CHALMERS

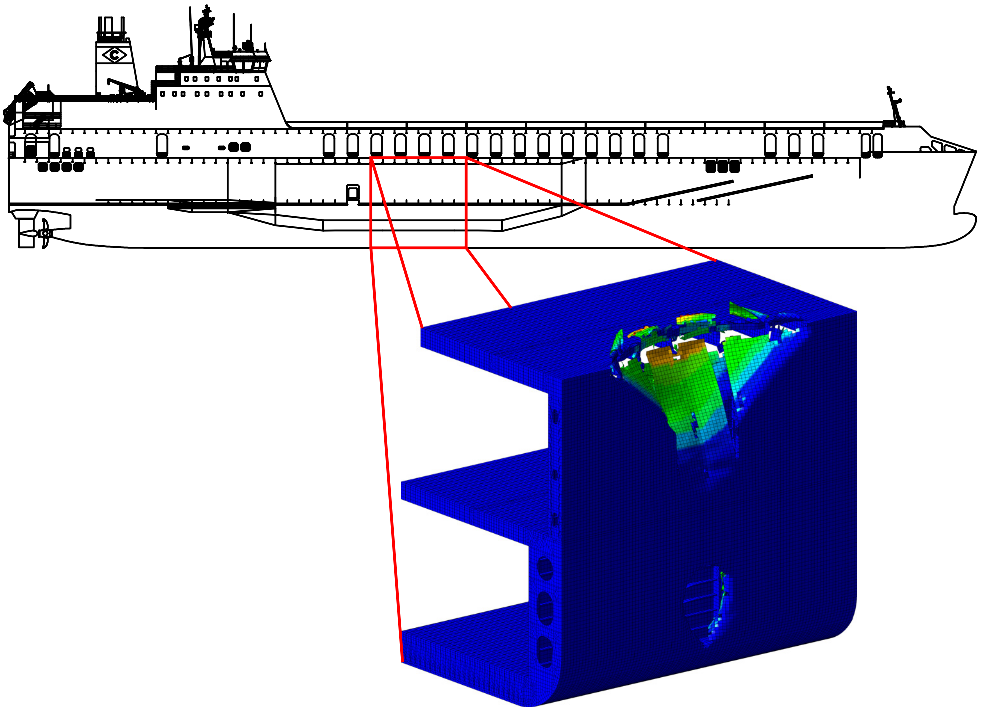

Simulation of Collisions between RORO Vessels with Improved Double-Hull Designs –

Influence of Modelling Parameters in Explicit Finite Element Analysis

Master of Science Thesis

MICHAEL ODEFEY

Department of Shipping and Marine Technology
Division of Ship Design
CHALMERS UNIVERSITY OF TECHNOLOGY
Gothenburg, Sweden, 2011
Report No. X-11/258

A THESIS FOR THE DEGREE OF MASTER OF SCIENCE

Simulation of Collisions between RORO Vessels with Improved Double-Hull Designs – Influence of Modelling Parameters in Explicit Finite Element Analysis

MICHAEL ODEFEY

Department of Shipping and Marine Technology
CHALMERS UNIVERSITY OF TECHNOLOGY
Gothenburg, Sweden 2011

Simulation of Collisions between RORO Vessels with Improved Double-Hull Designs – Influence of Modelling Parameters in Explicit Finite Element Analysis

MICHAEL ODEFEY

Report No. X-11/258

Department of Shipping and Marine Technology
Chalmers University of Technology
SE-412 96 Gothenburg
Sweden
Telephone +46 (0)31-772 1000

Printed by Chalmers Reproservice
Gothenburg, Sweden, 2011

Simulation of Collisions between RORO Vessels with Improved Double-Hull Designs – Influence of Modelling Parameters in Explicit Finite Element Analysis

MICHAEL ODEFEY

Department of Shipping and Marine Technology
Division of Ship Design
Chalmers University of Technology

Abstract

In this thesis the behaviour of the x-core double-hull design was investigated in various collision situations between two RORO vessels and compared to a conventional double-hull design using explicit finite element analysis. The purpose was, besides the examination of the x-core structure's increased crashworthiness, to investigate how different parameters influence the collision simulations. From this, recommendations were deduced on how to model future simulations most effectively. To achieve this, geometry models of both double-hulls and a striking bow section were created from CAD-data and drawings. The material model of a regular-strength shipbuilding steel was extended with the GL-approach describing a constant effective plastic failure strain, the PES-criterion describing a failure strain being dependent on sheet thicknesses of the shell model and mean edge lengths of the elements, and the RTCL-criterion accounting for triaxiality and introducing a damage variable. The RTCL-criterion was calibrated with simulated tensile tests. Collision simulations were carried out at two different draughts, hitting on a web frame and between two web frames, respectively. The collision angle was varied from the perpendicular angle to the struck hull to a 15 degrees inclination, and the influence of dynamic friction was examined. The conventional hull's level of detail was reduced and the x-core's mesh was coarsened and the resulting savings in time and errors in absorbed energy were examined.

It was found that the x-core structure shows the potential to provide a higher crashworthiness than the conventionally used hull. The PES-criterion responded well to changing sheet thicknesses, while the GL-approach and the RTCL-criterion were totally and virtually independent of them, respectively. Collisions from the inclined direction yielded higher energies than from the perpendicular one, which showed Minorsky's method to be inaccurate for this kind of collision. A comparison between results obtained from simulations regarding and disregarding friction showed only minor differences in the behaviour of folding structures and none in the absorbed energies. Simplification of the conventional double-hull and coarsening of the mesh of the x-core double-hull showed that the PES-criterion yielded the best compromise between reduction of calculation time and introduced error in this investigation.

Keywords: crashworthiness; explicit finite element analysis; failure criterion; friction; x-core.

Preface

This thesis was written at Flensburger Schiffbau-Gesellschaft (FSG), Flensburg, Germany, between January 2011 and June 2011. It is a part of the requirements for the Master's degree at Chalmers University of Technology, Gothenburg, and has been carried out at the Division of Ship Design, Department of Shipping and Marine Technology, Chalmers University of Technology.

First, I would like to acknowledge and thank my examiner and supervisor, Professor Jonas Ringsberg at the Department of Shipping and Marine Technology, for his guidance in finding and formulating an interesting topic, as well as his support during the thesis work. I would also like to thank my co-supervisor Professor Johan Ahlström at the Department of Materials and Manufacturing Technology for his valuable guidance and help, especially in the field of steels.

Furthermore, I would like to thank my co-supervisor at FSG, Karsten Werner, for his guidance and interesting discussions about explicit simulations and the application of the results of this thesis in future projects. I also would like to thank all persons at FSG and the Hamburg University of Technology who helped me with all smaller and larger problems during the thesis work, namely Jens Oliver Jensen, Ingo Tautz, and Martin Schötteindreyer.

Gothenburg, June 2011
Michael Odefey

Contents

1. Introduction

1.1. Background

The structural design of RORO (roll-on/roll-off) or ROPAX (roll-on/roll-off passenger) ferries constitutes thin-walled plate-structures that are in most cases weight-optimised to minimise fuel consumption. However, although the velocity of such vessels is usually not very high, its mass is still sufficiently large to develop an enormous amount of kinetic energy. In the case of a collision with another ship this energy will be transferred in a very short period of time resulting in serious damage to both ships, especially to the struck one, and thus the demand for a design of the ship that will provide maximum safety arises. For this reason, damage stability design, and, in this context especially partitioning of interior space, is currently governed by the mandatory regulations *International Convention for the Safety of Life at Sea* dating from 2009 (SOLAS 2009) to ensure a sufficient level of safety to minimise the risk for crew and passengers in such hazardous situations. However, in combination with conventional designs of double-hulls commonly used today those regulations do not lead to the most efficient design possible. The reason for this is that the available cargo space is not utilised to the most effective extent. For this reason the joint research project ELKOS (a German acronym meaning *Improvement of collision safety through the integration of structural measures into damage stability calculations of modern RORO passenger vessels*) was launched by the Flensburger Schiffbau-Gesellschaft (FSG) and Hamburg University of Technology (TUHH) and is funded by the German Federal Ministry of Economics and Technology. The aim of the project is to determine which structural measures that increase safety at collisions from alongside can be utilised in damage stability calculations complying with SOLAS 2009. The new regulations explicitly allow the freeboard deck to be submerged in case of damage, which provides many additional degrees of freedom regarding design. This can be valuable for ships with a large open lower cargo hold where an improvement of the resistance against penetration of the hull is highly beneficial and can lead to a higher level of safety. In this case the structure can be modified, i.e. the hull spacing can be reduced so that the level of safety returns to a value equivalent to that of the conventional hull. The important point with this method is that due to the reduced hull spacing a larger amount of space would be available at the same level of safety, and, for example, an additional car-lane on the cargo-deck could be introduced.

The overall objective with the ELKOS project is to create an interdisciplinary interface between the design of a ship, damage stability calculations, and structural mechanics. This will provide greater flexibility concerning partitioning while at the same time allowing for an easier prediction of the consequences on damage stability, which, in turn, can lead to products that are considerably more cost-effective.

1.2. Objective with this investigation

The main objective with this investigation is to examine the collision behaviour of a RORO vessel that is struck by another ship from alongside with respect to the design of the double-hull. In this context the behaviour of both a commonly used and a novel hull structure in simulations of various collision situations that can occur in reality should be examined by means of the explicit finite element (FE) method. It should also be studied in what manner the results for both hulls differ and what general conclusions can be valuable in future calculations and be drawn from them. Additionally, another objective is to show that an improved design can provide a higher crashworthiness than the conventional (in this context also reference) structure. This means that the improved design is intended to either provide a larger deformation depth until penetration of the inner hull, absorb a larger amount of kinetic energy, or both of these options. This would render it possible to decrease the total hull spacing, thereby increasing the available cargo area.

Furthermore, the models that are developed and used in the calculations should be parametric as far as possible and the entire process from building the model to running a collision calculation should be automated. This approach would provide greater flexibility and the framework created this way would allow FSG to easily customize and reuse the models and alter collision parameters with a less time-consuming adaption. Finally, parametric studies should be carried out to determine the optimum element size and minimum level of detail that would be necessary for not losing precision and falsifying results while at the same time allowing for a sufficiently large time-step size. This means that the largest allowable element size and smallest allowable modelling effort were to be identified. This would render it possible to implement the approach of collision calculations directly into the design cycle of a vessel.

1.3. Methodology

The finite element method was adopted to simulate collisions between RORO vessels. Emphasis was on the comparison of the behaviour of a conventional double-hull side-shell structure and a new innovative design, which improves the hull's capability of absorbing kinetic energy upon collision before fracture, i.e. its crashworthiness. In this context different failure criteria for the material were applied in different collision situations so that general recommendations could be made as to how a particular collision calculation in the future should be carried out. To achieve this, first the striking bow geometry was imported from FSG's CAD-system and adapted for the use in the commercial FE-software ANSYS (cf. section 4.1). Subsequently, a novel innovative double-hull design was chosen to be compared to the conventional one (cf. Section 4.3). The *x-core* design was selected for this particular task because it had already been tested in the *Crashcoaster* project in the European Union (cf. Vredeveldt [1]) and is known, while for a completely new design it could turn out that it is unsuitable and impairs crashworthiness. Furthermore, the x-core structure is among all other proposed structures the design that is most feasible to build for FSG from an economic and manufacturing point of view (cf. section 4.3). Both hull models and the bow model were established parametrically. This means that the process of creating the models and conducting collision calculations was automated as far as possible. This was done by building the x-core structure through keyword files and using a geometry for the conventional structure and the bow instead of manipulating their meshes directly. This approach would provide greater flexibility and the framework created this way would allow FSG to easily customize and reuse the models and alter collision parameters with a less time-consuming adaption.

The striking bow section, the double bottom, and the deck structures were created as geometries in ANSYS' CAD-interface and were used with both hull structures. The conventional hull was also created as a geometry in ANSYS, since the structure is highly irregular and thus the effort to automate its creation would have been disproportionally high (cf. Section 4.2). For the x-core design, on the other hand, the structure was intended to be both regular and adjustable. Therefore the hull segments were created by writing input scripts for ANSYS. As the next step a stress-strain curve describing a regular strength shipbuilding steel was obtained from the Technical University Hamburg-Harburg (TUHH) in Germany. To extend this material model and describe failure and removal of elements in the simulations three variably elaborate failure criteria were employed: the GL-approach prescribing a constant failure strain, the PES-criterion prescribing a mesh and sheet thickness-dependent failure strain, and the RTCL-criterion introducing a damage variable and taking triaxiality into account. This last criterion was then calibrated using simulated tensile tests incorporating different mesh sizes and sheet thicknesses (cf. Chapter 3).

In the main part of this thesis, several different collision situations were calculated with both hull models to determine if the novel design can absorb more energy until fracture of the inner hull occurs compared to the conventional one. For this purpose collisions at two different draughts with the point of impact both on a web frame and between two web frames were investigated. Additionally, the energies transferred into the structure by stem and bulb, respectively, were determined. These energies could then be compared to the results of practical bulb-only collision tests on one module that are planned to be done at TUHH. Besides an impact perpendicular to the struck ship's side ($\Phi = 90°$) a second impact angle of $\Phi = 75°$ was investigated. The collisions at $\Phi = 90°$ were carried out without friction and with a dynamic friction coefficient of $\mu_k = 0.3$ to examine possible differences in energy absorption and in failure modes. In a last step the amount of time which could be saved and the size of the error that was introduced when the structure was defeatured and the mesh was coarsened was investigated. This means that structure and mesh were changed and the deviations of the results compared to those obtained from the detailed structure and the fine mesh were determined.

1.4. Limitations

In the collision calculations, several assumptions were made that imply certain limitations on the models. Firstly, external dynamics of the struck ship such as sway or sideways motion are neglected because these would influence the energy absorption behaviour of the hull structures. Secondly, the striking bow was modelled as a rigid body. A deformable bow would consume a large fraction of its kinetic energy through deformation by itself, instead of transferring it to the respective hull structure. These limitations were made because the intention was to calculate a worst case scenario. The rigid bow, on the other hand, made it possible to decrease the necessary calculation time significantly, and to adjust its mass by increasing its density. The bow's mass due to its original density and sheet thickness was only about 0.38% of the entire vessel's mass, which would have provided a wrong kinetic energy. To solve this, either the density of the bow could be increased or an additional mass element could be introduced on each node. In this investigation the first option was chosen, since in this way the mass is increased smoothly and evenly over the entire bow. This does not mean a difference for the rigid bow but in future simulations, where a deformable bow is employed, this approach prevents the model from discontinuities. The bow was modelled with elements having a mean edge length of 500 mm, resulting in 2154 nodes (cf. Section 4.1). This means if a mass element was put on each node to preserve an even mass distribution each of these elements would possess a mass of about 5603 kg. This large mass discontinuity between the centre of an element and its nodes could cause incorrect inertia effects.

2. Theoretical background

2.1. Probabilistic damage stability

As Lewis [2] states, every seaborne vessel that is not constructed from buoyant materials only, but for instance from steel, is subject to capsizing and sinking in case its *watertight integrity* is lost. While this can occur through all kinds of accidents like collision, grounding, and also internal disasters like fire or explosions, the first two of these are according to Lehmann and Peschmann [3] despite all technical and nautical improvements still common nowadays. To counteract these hazards that could cause ship-loss, subdivisions such as watertight bulkheads and double bottoms have been made an inherent part of ship design, since a hull structure that preserves the ship's floatability even in damaged condition reduces the consequences of an accident considerably [3]. However, neither the instant of time and location of the event nor the actual extent of damage is known beforehand. Furthermore, the type and amount of cargo are different for every trip. Consequently, there are numerous unknown variables, and designing towards a ship that is able to withstand all thinkable disasters would lead to an economically useless concept. Accordingly, a compromise in placing subdivisions has to be found that satisfies both safety demands and economic demands. For this reason, the International Maritime Organization (IMO) has introduced a set of directives which are in their latest version known as the harmonized *SOLAS 2009* regulations. It is stated by IMO [4] that the foundation of these regulations is, contrary to the previous ones which exhibited a deterministic character, a probabilistic concept that assigns an *attained subdivision index A* to a ship. This index expresses the safety of a vessel through the likelihood of survival in the case of inflicted damage, for example the collision with another ship, and is intended to introduce a possibility to compare the levels of safety of different vessels. This means that if the indices of two ships have the same value they are equally safe. According to Hogström [5] A is a compound of several indices and can be calculated as:

$$A = 0.4\sum_{i=1}^{n_a}(P_i S_i)_a + 0.4\sum_{j=1}^{n_b}(P_j S_j)_b + 0.2\sum_{k=1}^{n_c}(P_k S_k)_c \tag{1}$$

At a particular draught of the ship for each compartment the product of the probability of damage and flooding P and the probability of survival S is computed, where a, b, and c represent summer-load line draught, partial subdivision draught, and light-service draught, respectively. These draughts are shown schematically in Fig. 1. As is mentioned by Deltamarin [6], a is the deepest subdivision draught, c is the lightest loading case that is assumed, and b lies between the two aforementioned loading cases being calculated as $b = c + 0.6(a - c)$. The sum over all compartments is multiplied with a weighting factor representing the frequency which the respective draught will be found in service with. Finally, the indices for all occurring draughts are summed up to yield A.

Despite the intention to create a fully probabilistic concept to replace the former deterministic one there are still residual deterministic parts in the regulations. While the probabilistic parts are recalculated for each individual design, the probability of survival S is determined from statistics built on the data obtained from a number of reference vessels. This methodology disagrees with the actual goal of the updated regulations. Therefore, an alternative approach that is based on probabilistic data obtained from collision calculations is the object of research of the ELKOS project.

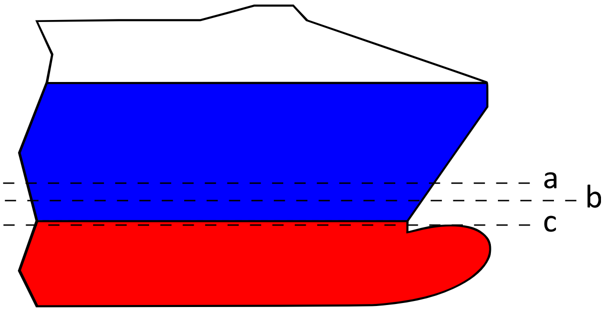

Fig. 1. Schematic distribution of the waterlines specified in SOLAS 2009.

2.2. Dependence of material properties on the strain rate

As Peschmann [7] states, a steel's response to a loading situation and especially its hardening characteristics strongly depend on the deformation rate. Thus a number of different material laws relating material properties and deformation behaviour to the strain rate have been developed out of which two of the most used ones are the *Voce model* and the *Cowper-Symonds model*.

The Voce model is a strain rate-dependent constitutive material model in a power law form that describes, according to Cao et al. [8], the stress-strain curve of a material in a linear steady state. It is defined as:

$$\sigma = \sigma_s - (\sigma_s - \sigma_0) e^{-\left(\frac{\varepsilon_p}{\varepsilon_0}\right)} \tag{2}$$

with the saturation stress σ_s. At this stress a state of fully plastic yielding is reached, which means strain hardening ceases and a neck develops. σ_0 is the extrapolated initial stress that is, according to Selin [9], approximately equal to 0.1% proof stress. ε_0 is the relaxation strain describing the dynamic recovery rate that expresses the annihilation of dislocations, as Cao et al. [8] state. To obtain values for these parameters, dynamic tension/compression or bending tests are conducted and the parameters are then fitted to the measured data. As Cao et al. [8] report, the fitted curve for each measurement correlates well with their respective measured curve for an interstitial free (IF) low alloyed steel. They found that both σ_0 and σ_s generally increase with an increasing strain rate, while ε_0 is characterised by three stages. It shows decreasing, slightly increasing, and again decreasing behaviour with an increasing strain rate, respectively. The first stage is governed by the diffusion of atoms and vacancies being favourable at lower strain rates and consequentially by recovery [8]. In the second stage, diffusion is constrained due to the increased strain rate and thus shorter diffusion time. Stage three lies at even higher strain rates and is as the first stage characterised by recovery resulting from a shorter diffusion distance and a higher temperature.

The Cowper-Symonds model is a constitutive material model that accounts for strain-rate effects by scaling the flow stress. The model is defined as:

$$\sigma_{dyn} = \sigma_{stat}\left[1+\left(\frac{\dot{\varepsilon}}{D}\right)\right]^{\frac{1}{p}} \tag{3}$$

with the quasi-static yield strength σ_{stat} obtained from a tensile test and the scaled yield strength σ_{dyn}. D and p are fitting constants. Peixinho and Pinho [10] mention as a major disadvantage of the Cowper-Symonds model in Eq. (3) that the fitting constants depend on the reference stress. This means that $\sigma_{Rp0.2}$ and σ_{UTS} will yield different constants so that a consistent modelling procedure is essential. Furthermore, as Peixinho and Pinho [10] state, this means that values obtained for $\sigma_{Rp0.2}$ can yield wrong results for higher stresses. In their results for a DP600 and a TRIP600 steel, deviations between stress-strain curves found for different reference stresses at the same strain rate of 200 MPa can be observed. Peschmann [7] states that the scale factor stays constant for a constant strain rate while it can be shown in experimental tests that the flow stress increases faster with an increasing strain rate. At collisions the strain rate gradient is very high, especially close to the point of impact and thus, although this model is easy to use, the disadvantage of varying results renders its predictions uncertain. According to Peixinho and Pinho [10] the Cowper-Symonds model has therefore been modified to be able to account for large plastic strains and a varying exponent:

$$\sigma_{dyn} = \sigma_{stat}\left[1+\left(\frac{(\varepsilon_u-\varepsilon_y)\dot{\varepsilon}}{(\varepsilon-\varepsilon_y)D_u+(\varepsilon_u-\varepsilon)D_y}\right)\right]^{\frac{(\varepsilon_u-\varepsilon_y)}{(\varepsilon-\varepsilon_y)p_u+(\varepsilon_u-\varepsilon)p_y}} \tag{4}$$

Here the indices y and u denote *yield* and *ultimate tensile* stress and strain, respectively, while for the strains $\varepsilon_y \leq \varepsilon \leq \varepsilon_u$ holds. As Peixinho and Pinho [10] mention, Eq. (4) yields the closest approximation to their experimental results and their conclusion is that it is superior to the more simple approach in Eq. (3).

2.3. Minorsky's method

Besides an FE analysis of a collision situation, several other methods to investigate the effects on a struck ship have been developed. Especially if the finite element method cannot be developed fast enough to contribute to the design cycle of the ship or if it is not available these methods that were partly developed before the FE method itself allow for a quick estimation of the energies involved in the collision. The simplest and also fastest and easiest model to implement was formulated by *Minorsky* in 1959 (cf. Minorsky [11]) and it became the most popular one according to Brown [12]. Minorsky's method is based on conservation of momentum and on the assumption that the collision is totally inelastic. Additionally, motion is confined to one dimension, which makes the formulation of an analytical model possible. This is contrary to other methods which are similar to the FE method and use numerical integration to determine the resulting energies. Minorsky proposed the total absorbed energy as:

$$\Delta KE = \frac{M_B \times 1.4 M_A}{2(M_B + 1.4 M_A)} v_B^{\,2} \tag{5}$$

with the masses of striking and struck ship M_B and M_A, respectively, and the striking ship's initial velocity v_B (cf. Brown [12]). A second equation was introduced to account for collision angles $\phi \neq 90°$:

$$\Delta KE = \frac{M_B M_A}{1.43 M_B + 2 M_A} [v_B \sin(\phi)]^2 \tag{6}$$

It should be noted that Eqs (5) and (6) take into account the sway of the struck ship into the direction that the striking one has at the instant of impact. This increases the mass of the struck ship since the hydrodynamic mass of the surrounding water is involved. Figure 2 shows an example of the distribution of absorbed energy over the collision angle for $M_A = M_B = 12.114 \times 10^6$ kg and $v_B = 5$ m s^{-1}.

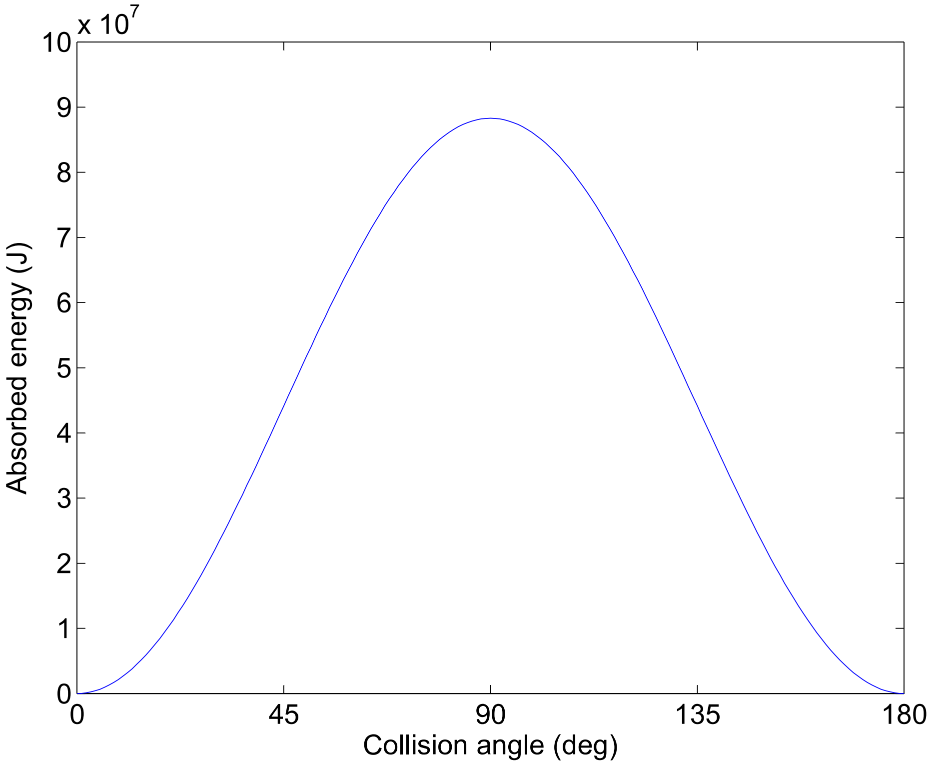

Fig. 2. Exemplary energy distribution of Minorsky's method.

3. Modelling of the material's behaviour

In the event of collision the structural behaviour of a ship is dominated by tearing of both the hull and structural members, see Peschmann [7]. This means that these tearing processes take the greatest part in the energy balance. Therefore it is very important for an FE simulation to employ, besides correct material data, a failure criterion that can reproduce this particular process correctly, since it will directly influence the ship's survival in the simulations. However, the criterion should also be as simple as possible because it has to be calibrated against material data which in turn is obtained from, for example, a tensile test or a forming limit test. This means that a criterion that uses many calibration parameters can be very accurate. On the contrary, the introduction of more variables renders the result statistically more uncertain due to scatter in the data from which the parameters are determined. Additionally, it can be impossible to calibrate many parameters in practice due to the necessary financial and temporal effort.

Tørnqvist [13] states that the definition of a maximum allowable equivalent plastic strain is the most common way of setting up a failure criterion in ship collision and grounding because it is simple and convenient. However, several limitations are imposed on the model if this strain is set constant. The reasons for this are that firstly, the fracture behaviour in FE-calculations is dependent on the used mesh size, as Peschmann [7] states. Here it should be added that according to Hogström et al. [19] also the damage process after necking leading to fracture is highly mesh-dependent. Secondly, according to results found by Bao [14], in the plastic region not only the equivalent strain but also the stress-state, i.e. the triaxiality, has a considerable effect on the behaviour of the material. Additionally, this last point has, according to Peschmann [7], also a noticeable effect on damage initiation. Stress and strain ratios, on the other hand, affect the fracture strain only to a minor extent, as Peschmann [7] and Bao [14] found. Furthermore, no data was available accounting for these effects and therefore they have been omitted in this thesis. To examine the effects of mesh size and triaxiality three different failure criteria were employed, which, sorted by increasing elaborateness, are: a constant failure strain according to the guidelines of Germanischer Lloyd (cf. GL [15]), a mesh-dependent failure strain after Peschmann [7], and the RTCL-criterion which takes triaxiality into account and makes use of a damage variable (cf. Tørnqvist [13]).

3.1. The true stress-strain curve

Stress-strain data for a material is commonly obtained through a tensile test which yields the engineering stress-strain curve. It is done by measuring the acting force with respect to the initial cross-section and the elongation with respect to the initial sample length. However, as Peschmann [7] states, the data needed for modelling the material behaviour is the true stress-strain curve, since both engineering stress and strain are by definition dependent on the initial sample geometry, while true stress and strain are not. This is because the latter ones are determined by measuring the acting force with respect to the current cross-section and the elongation with respect to the current sample length. The direct measurement of the current sample's cross-section is difficult to accomplish in a tensile test if strains are localised in a neck, though it is possible by means of optical monitoring systems. Therefore, most commonly the engineering stress-strain curve of a sample is measured. It is then converted to the true stress-strain curve by applying Eqs (7) and (8), where σ_e and ε_e are the engineering stress and strain, respectively, F is the acting force, and A_0 is the initial cross-section. It should, however, be noted that the applicability of the Eqs (7) and (8) is limited, as Dowling [16] states. Starting from the necking point, the engineering strain is only an average value of the actual strain in a non-uniformly elongated region of the specimen [16]. This means that it is not the maximum occurring value and thus cannot be used to determine the true strain. In this case, the actual minimum cross-section has to be measured continuously during the test to be able to calculate true stress and strain. Dowling [16] also mentions that Eq. (7) is inaccurate if σ_e is smaller than the yield stress or lies close to it. It is suggested that up to twice the strain that is measured at the offset yield point the differences between engineering and true stress are negligible [16].

$$\sigma_t = \frac{F}{A_0}(1+\varepsilon_e) = \sigma_e(1+\varepsilon_e) \tag{7}$$

$$\varepsilon_t = \ln(1+\varepsilon_e) \tag{8}$$

Another possibility to obtain a true stress-strain relationship is to calibrate the data by means of simulated tensile tests using the finite element method. The stress-strain data obtained from TUHH is shown in Fig. 3. This curve was created by recomputing real tensile tests, which had been conducted at TUHH, with the finite element method (cf. Tautz [17]), meaning that it was adjusted several times until the results from the calculations showed good accordance with the results from the practical tests. This means that the data points are not the original measured values but values which best reproduce the behaviour of the real tensile specimen in a simulated tensile test. The data points are interconnected by linear functions so that the most suitable material model in LS-DYNA is *modified piecewise linear plasticity*. The characteristics of the curve are very similar to true stress-strain curves shown by Dowling [16], except that beginning with $\varepsilon = 0.3$ the curves assumes a constant slope. A measured stress-strain curve would instead show an increasing slope at higher strains due to the rapidly decreasing cross-section locally, called the neck. Tautz assumed that the reason for this deviating behaviour is that a plastic strain of 30% was the upper boundary of the strain range that he could use in his iterative process of adjusting the stress-strain data so that the simulations would reproduce the measurements. To be able to carry out simulations incorporating configurations that allow a larger strain until they fail he extended the curve linearly up to $\varepsilon = 1$.

The tensile tests at TUHH had been conducted with flat specimens made of regular strength shipbuilding steel with a yield strength of $\sigma_y = 314\,\text{MPa}$. According to Tautz, different geometries (perforated, welding seam under different angles) were tested, each of which represented by one specimen, to determine the dependency of the local plastic strain on the configuration of the specimen. The dimensions of a specimen are shown in Fig. 4. The general steel properties that were used in all calculations in the current investigation were a Young's modulus of E = 210 GPa, a Poisson's ratio of $\nu = 0.3$, and a density of $\rho = 7.85 \times 10^3$ kg m^{-3}. The tests were carried out quasi-statically. The necking and fracture strains of the geometry shown in Fig. 4 (without any additional features) are also plotted in Fig. 3.

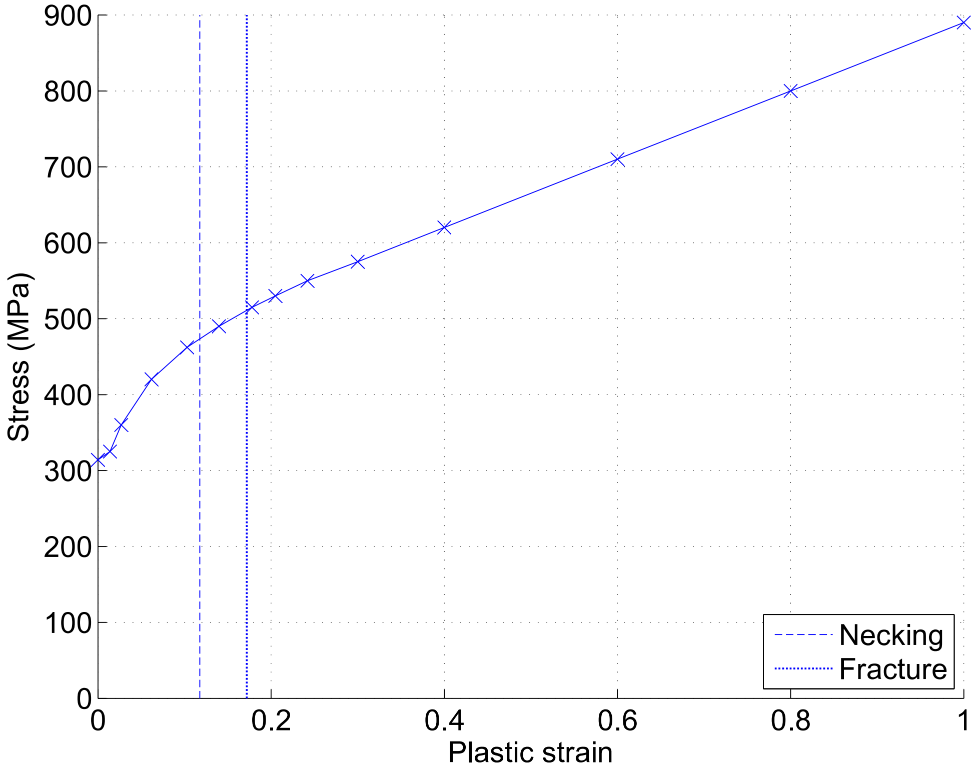

Fig. 3. True stress-strain curve obtained from TUHH. The data point at $\varepsilon = 0.3$ marks the border between the portions of the curve having a varying and a constant slope, respectively. The necking and fracture strains are those of the specimen shown in Fig. 4.

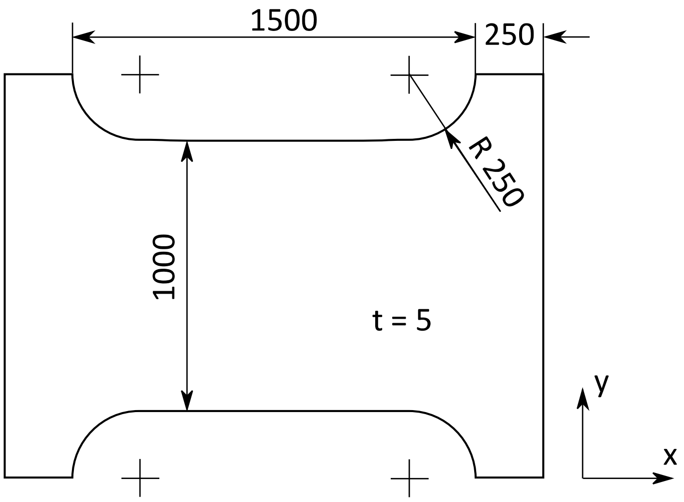

Fig. 4. Specimen used in the tensile tests at TUHH, all dimensions in mm.

3.2. The GL constant effective failure strain approach

In the latest rules and guidelines for seagoing ships by GL [15] the failure strain to be used in collision calculations is stated as:

$$\varepsilon_f = 5\% \tag{9}$$

This constant failure strain takes none of the dependencies mentioned above into account and the low value corresponds to very limited plasticity before fracture. This means that only little energy can be absorbed, which renders the approach conservative. The value from Eq. (9) was set as the effective plastic strain at failure in calculations utilising the GL-approach.

3.3. The PES failure criterion

Peschmann [7] refers to the tensile test to reason a dependency of a part's failure strain on its element size and the intention behind the PES-criterion. Here, the global strain is measured over the entire test section of the specimen and used in the stress-strain curve. The strain close to the necking point, however, can be considerably higher than the global value, especially for ductile materials (cf. Peschmann [7], Tautz [17]). Hence, if the average element length is large only the global strain is measured and the failure strain is low. If on, the other hand, the average element length is small also large local strains can be resolved and the value of the failure strain should be correspondingly higher. As stated by Kuhn and Medlin [18] this behaviour is described by *Barba's law,* which relates the extension of a specimen to its dimensions (cf. also Hogström [5] and Hogström et al. [19]), meaning that if two specimens are geometrically similar this will also hold for their necks. For a flat specimen this relation expressed as engineering strain is:

$$e_f = \beta \frac{\sqrt{A_0}}{L_0} + e_u \tag{10}$$

with the uniform elongation strain ε_u, initial cross-section and length A_0 and L_0, and a proportionality constant β (cf. Kuhn and Medlin [18]). Peschmann [7] suggests a relation between failure strain, the thickness of an element, and its edge length to account for the behaviour mentioned above in finite element calculations:

$$\varepsilon_f = 0.08 + 0.65 \frac{t}{l} \tag{11}$$

If exemplary values of t = 12 mm and l = 200 mm are inserted into Eq. (11) the result is a failure strain of $\varepsilon_f = 11.9\%$. This value lies significantly below usual measurements. This is because, as Ehlers [20] states, the criterion underestimates the failure strain at too large element sizes. As Alsos et al. [21] state, the reason for this is that the failure strain output by this kind of failure criterion is merely an averaged critical strain. A shell element which is strained until fracture can be thought to consists of two parts, as shown in Fig. 5. These are the necking region in the middle of the specimen and the residual parts around it. While the residual parts are uniformly strained the necking region shows a peak strain at failure. Furthermore, *plastic incompressibility* is assumed, so that both V_1 and V_2 stay constant during the process [21]. The concept of plastic incompressibility is explained by Dowling

[16]: elastic strain contributes to a volume change, while plastic and creep strains do not. In a tensile test up until fracture elastic strains can be assumed to be small and hence the volume to be approximately constant [16]. Since the element now contains both the peak and uniform strains, these are averaged over the entire element to the element's critical strain. This averaged strain is as a matter of course smaller than the peak strain, and, depending on the chosen element size, it can also be smaller than the measured critical strain.

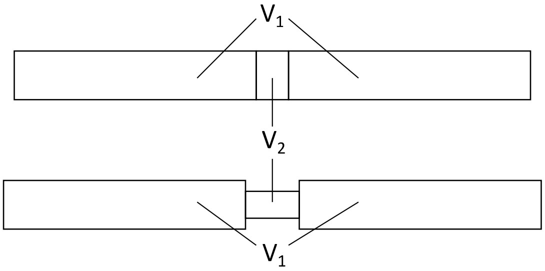

Fig. 5. Schematic illustration of the straining process of a shell element, seen from its side; unstrained (top) and strained (bottom). The volumes V_1 and V_2 stay constant in this process. The third dimension is not shown.

If the above exemplary value for the element length is changed to $l = 30$ mm the failure strain is $\varepsilon_f = 34\%$, which is a value that is not unusual for a practical tensile test (cf. for example Dowling [16]).

The dependency after Peschmann [7] can be seen in Fig. 6 for $0 \le \frac{l}{t} \le 50$ and in Fig. 7 for $0 \le t \le 30$ mm and $0 \le l \le 600$ mm. Equation (11) was used to calculate the effective plastic strain at failure for every shell in the models.

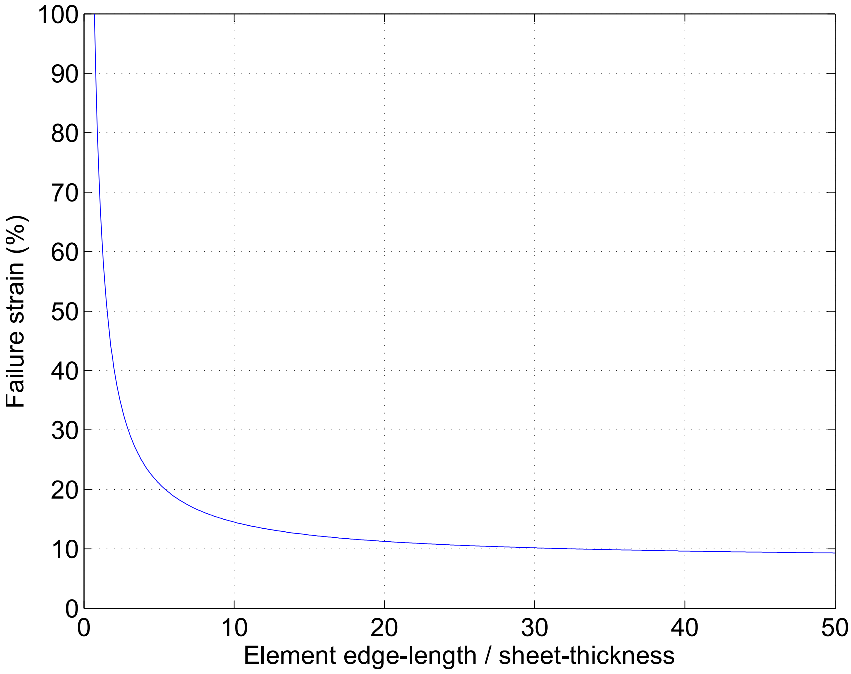

Fig. 6. Failure strain after Peschmann [7] for $0 \le \frac{l}{t} \le 50$.

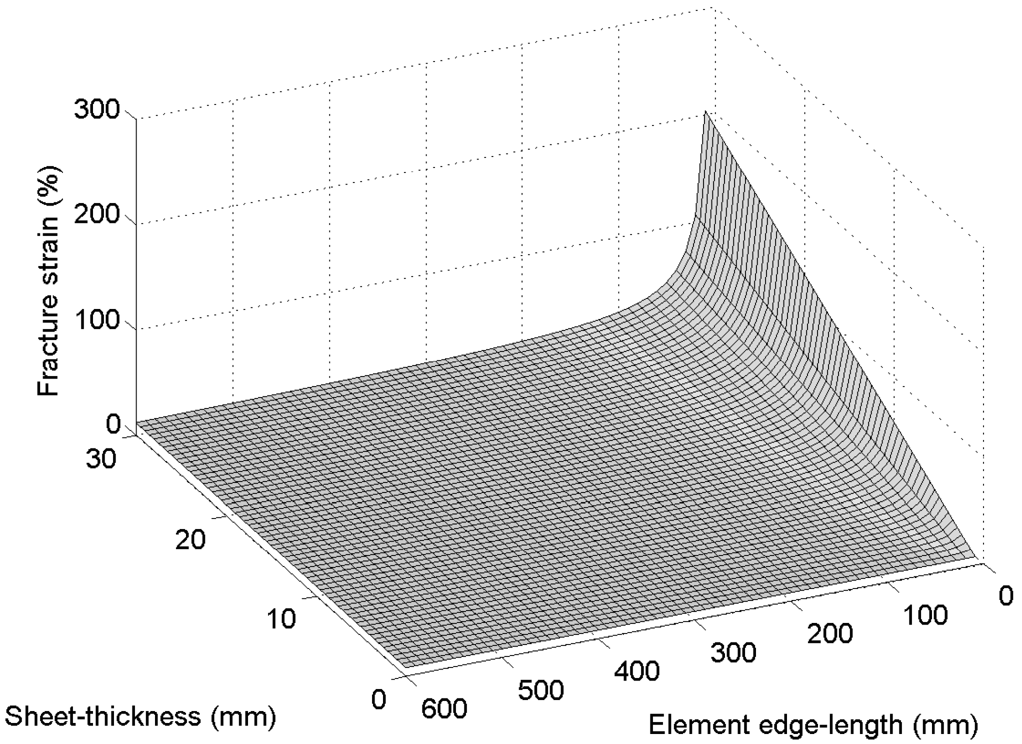

Fig. 7. Failure strain surface dependent on mean element edge length and sheet thickness for the PES-criterion.

3.4. The RTCL failure criterion

The RTCL-criterion introduces a damage variable which is formulated in terms of effective plastic strain increment and causes failure when it reaches unity. The criterion was first proposed by Tørnqvist [13] and is composed of a void growth model developed by Rice and Tracey, and a shear failure model developed by Cockroft and Latham, which account for tensile and compressive load, respectively. The RTCL-criterion takes the multiaxial stress-state at plastic deformation, i.e. the triaxiality *T*, into account which is defined as:

$$T = \frac{\sigma_h}{\sigma_{eq}} \tag{12}$$

with the von Mises equivalent stress and the hydrostatic stress:

$$\sigma_{eq} = \sqrt{\frac{(\sigma_1 - \sigma_2)^2 + (\sigma_2 - \sigma_3)^2 + (\sigma_3 - \sigma_1)^2}{2}} \tag{13}$$

$$\sigma_h = \frac{1}{3}(\sigma_1 + \sigma_2 + \sigma_3) \tag{14}$$

In its general form the RTCL-criterion determines the damage according to Tørnqvist [13] by integrating a triaxiality function over the strain:

$$D = \int f(T)_{RTCL} d\varepsilon \tag{15}$$

with:

$$f(T)_{RTCL} = \begin{cases} 0 & for \quad T \leq -\frac{1}{3} \\ 2\frac{1+T\sqrt{12-27T^2}}{3T+\sqrt{12-27T^2}} & for \quad -\frac{1}{3} \leq T \leq \frac{1}{3} \\ \frac{1}{1.65}\exp\left(\frac{3}{2}T\right) & for \quad T \geq \frac{1}{3} \end{cases} \tag{16}$$

However, a much more commonly used form integrates over the effective plastic strain and is normalised with respect to a damage strain parameter, since it is easy to handle in terms of calibration, as is stated by Alsos et al. [21] (cf. Section 3.5):

$$D_i = \frac{1}{\varepsilon_0}\int f(T)_{RTCL}\, d\varepsilon_{eff}{}^p \tag{17}$$

Here $d\varepsilon_{eff}{}^p$ is the effective plastic strain increment and the material fails at $D_i = 1$. The damage strain parameter ε_0 can then be calculated numerically according to the discretisised form Eq. (18):

$$\varepsilon_0 = \int f(T)_{RTCL}\, d\varepsilon_{eff}{}^p \approx \sum_{i=1}^{n} f(T)_{RTCL,i}\, \Delta\varepsilon_{eff}{}^p \tag{18}$$

3.5. Calibration of the RTCL failure criterion

A failure criterion is usually applicable to a variety of different materials and therefore to be able to use it with a particular material with specific properties it has to be calibrated against test data. For this purpose, the more complex failure criteria possess parameters which have to be fitted to measured values to adjust them to the material. Concerning this matter the RTCL-criterion is highly suitable for the current study because it can be calibrated by means of only one parameter that can be obtained by a tensile test, which matches the available material data. This is because at pure tension $\left(T = \frac{1}{3}\right)$ the values of the damage strain parameter and the effective plastic strain at failure become equal, as Alsos and Amdahl [22] mention.

For the calibration of the RTCL-criterion the FE model of a flat tensile specimen was used. For consistency reasons, the dimensions and set-up were chosen in the same manner as the configuration Tautz [17] used in his calculations (cf. Fig. 4), since the calibration of the material data obtained from TUHH was done with this model. The left edge of the model was constrained in all directions, the right edge in the y- and z-directions, while the load was applied in the x-direction as a constant velocity. Additionally, all rotations on these two edges were constrained. The tests were done for different meshes and sheet thicknesses to examine the dependence of ε_0 on these parameters. The meshes are shown in Fig. 8 in the unstrained condition and at the instant of failure, meaning that they have reached the global failure strain from the experiments. All specimens will subsequently be denoted with their element edge-length-to-sheet-thickness ratio (e.g. 100/10 for $l = 100$ mm and $t = 10$ mm).

A tensile test is a quasi-static problem, since the applied strain rate is low and therefore for the simulation of such a test a quasi-static approach is needed, because using an explicit algorithm to simulate a tensile test results in unfeasibly small time steps and the loss of precision. Therefore, LS-DYNA offers the possibility to switch to an implicit algorithm so that geometries and data, such as for example material models, do not have to be transferred to another finite element system. This approach was used to simulate the tensile tests and determine mesh- and thickness-dependent values for ε_0. It should be noted that due to the large dimensions of the specimen, the loading rate was set to $v_l = 1\,\text{m s}^{-1}$ in order to gain acceptable calculation times. This did not influence the material itself since the material model was strain rate independent, as mentioned above. However, the high loading rate rendered it difficult for the implicit algorithm to converge, especially for small elements and thin sheets. For this reason LS-DYNA offers a function to switch between implicit and explicit during a calculation if no convergence can be achieved. With this method in use, satisfactory calculation times could be achieved. On the other hand, it should be noted that excessive switching from implicit to explicit and back can cause the response of the system, i.e. stresses, to build up and oscillate in certain situations, resulting in a massive loss of precision.

Each test was run until the global true uniaxial failure strain found in the real tensile tests conducted at TUHH was reached, i.e. until the onset of cracking, which was at $\varepsilon_f = 17.2\%$. Local necking did not occur in any of the tests. Instead, a diffuse neck appeared spanning the slender part of the specimens completely (cf. Fig. 8), which complies with the results found by Urban [23]. However, due to the missing local neck the model does not show a realistic behaviour. In a real tensile test the specimen either does virtually not neck (brittle behaviour), develops a local neck (ductile behaviour), or shows a behaviour between these two. The reason for this is that the stress-strain curve (Fig. 3) assumes a constant slope at higher strains, instead of developing an increasing slope due to the specimen's rapidly reducing cross-section. As a consequence, the material model does not accurately account for the damage degradation process. Instead, the material maintains a high level of hardening, which counteracts necking. However, a lot of effort had been put into adjusting the data in Fig. 3 and it has been used successfully at TUHH so far. Therefore, it was the only material model that was available.

After having finished a test the effective plastic strain ${\varepsilon_{eff}}^p$, von Mises equivalent stress σ_{eq}, and the three principal stresses σ_1, σ_2, and σ_3 were extracted for every time step, and hydrostatic stress, triaxiality, and triaxiality function *f(T)* were calculated (cf. Eqs (12), (14), and (16)). Subsequently, the product of *f(T)* and the strain increment $\Delta{\varepsilon_{eff}}^p$ were calculated for every time step and summed up to obtain the uniaxial damage strain parameter ε_0 for the RTCL-criterion according to Eq. (18).

The parameters found from the tests are shown versus the mean element edge length in Fig. 9 and versus sheet thickness in Fig. 10. The values for the different mesh sizes at one particular thickness are very similar except for those found from the specimens 75/5 and especially 50/5. Judging from the figures, it can be suspected that in Fig. 9 both data points should lie close to those from the tests with t = 10 mm and t = 15 mm, respectively, as it is the case for l = 100 mm. From Fig. 10 it can be suspected that the parameters also should assume the same value as the respective results from t = 10 mm and t = 15 mm, resulting in being independent of t. This is due the system's build-up, which is mentioned above, causing an oscillating behaviour that could be observed for t = 5 mm (cf. Fig. 11). It can be seen that the global characteristics of the curve show an increasing progress. The numerous local peaks, on the other hand, falsify quantities (i.e. σ_{eq} and consequently ε_0) which are computed from the data points. Therefore, the tensile tests of specimens 75/5 and 50/5 were repeated with modified parameters, as described below.

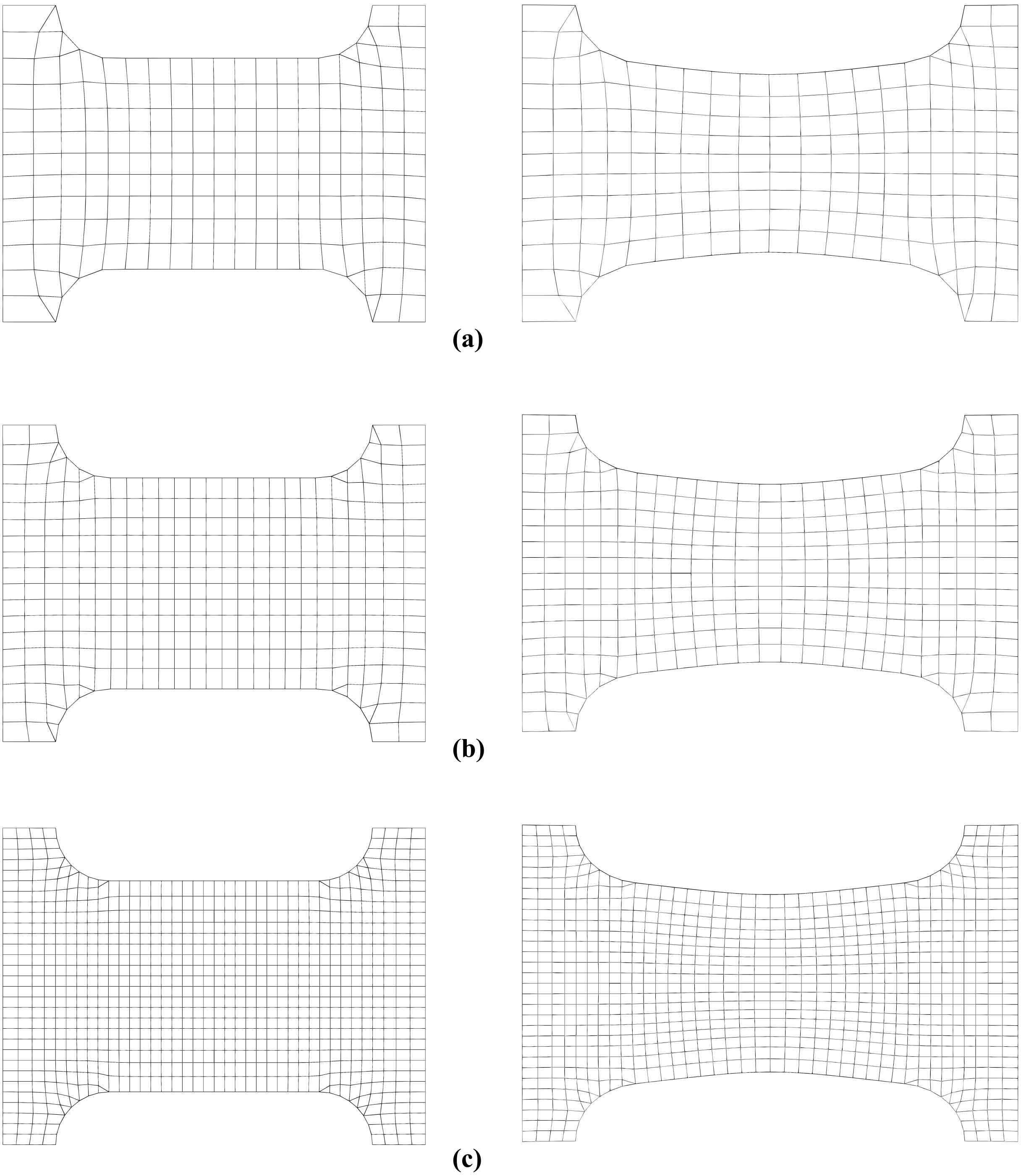

Fig. 8. Meshed tensile model, unstrained (left) and at the instant of failure (right): l = 100 *mm* (a), l = 75 *mm* (b), and l = 50 *mm* (c).

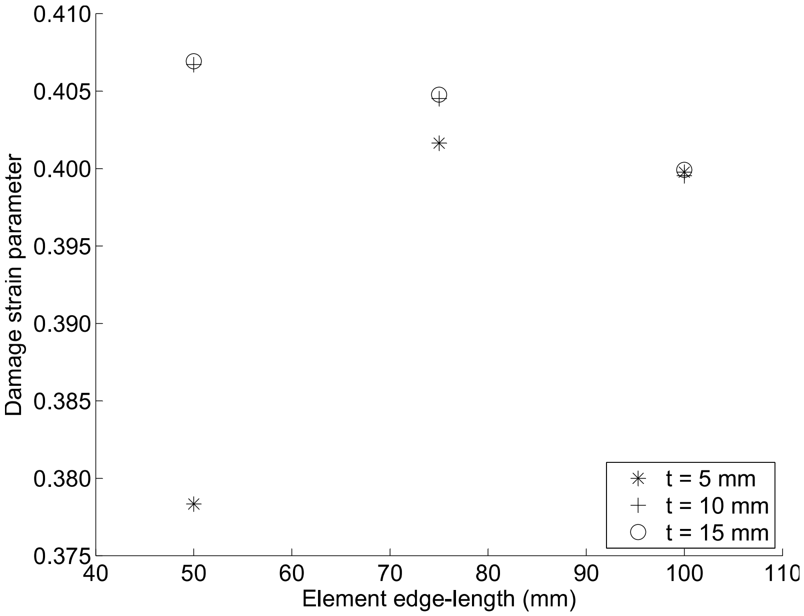

Fig. 9. Dependence of the damage strain parameters found from the simulated tensile tests on element edge lengths.

Figure 12 shows the dependencies of the damage strain parameter ε_0 on the element edge-length-to-sheet-thickness ratio l/t for the simulated tensile tests. It can be seen that the parameter slightly decreases with increasing ratio and according to Alsos and Amdahl [22], Ehlers et al. [24], and Simonsen and Törnqvist [25] this dependency is inversely proportional. This is because, as is stated by Ehlers et al. [24], *virtual local necks* that develop within large elements can be taken into account by:

$$\varepsilon_f = n + (\varepsilon_n - n)\frac{t}{l_e} \tag{19}$$

In this material-specific function, n is the exponent of the respective power law model and ε_n the failure strain at uniaxial stress when $t = l_e$. Accordingly, Eq. (19) was taken as the regression polynomial for the values obtained from the simulations resulting in:

$$\varepsilon_0\left(\frac{l}{t}\right) = 0.3928 + 0.0514\frac{1}{\frac{l}{t}} \tag{20}$$

which is shown in Fig. 12 as the dashed curve. To improve the results for the specimens 75/5 and 50/5 these two tensile tests were repeated with a scaled model where all dimensions were scaled up by the factor of 2. The results are shown in Fig. 12 and are denoted as new. Accordingly, the regression polynomial was recomputed as:

$$\varepsilon_0\left(\frac{l}{t}\right) = 0.4007 + 0.0210\frac{1}{\frac{l}{t}} \tag{21}$$

It can be seen that the range of damage strain parameters covered by the results is very narrow for the old curve and even narrower for the new one. This suggests that in the present case ε_0 depends on mesh size and sheet thickness only to a very small extent.

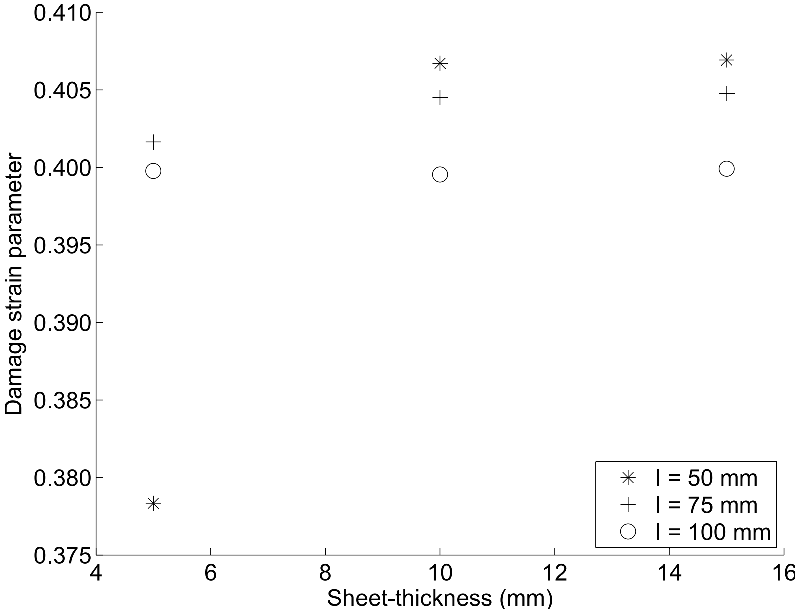

Fig. 10. Dependence of the damage strain parameters found from the simulated tensile tests on sheet thicknesses.

In Fig. 13 the evolution of effective plastic strain until fracture at the point of fracture over global strain is shown for all three sheet thicknesses. It can be seen that the curves lie very close to each other but still have small differences, which conforms to the narrow range of results for ε_0. Nevertheless, because of the differences that are still present, Eq. (21) was applied in the calculations instead of a simple average value. It should be noted here that the similarity in the evolutions of plastic strain mentioned above can be explained by the fact that no local but only global necking occurred. Hogström et al. [19] found in their tensile tests that for different lengths of virtual extensometers, corresponding to different mesh-densities, a divergence of stress-strain curves was observed from the point of local necking, while formerly all curves took similar courses. This means that a tensile test accounts for size scale effects of changing mesh-densities and hence is useful for calibration, if these effects should be included.

In Fig. 14 the triaxialities for all element sizes and a sheet thickness of $t = 15$ mm are plotted over the global strain until fracture. Even though the set-up is a uniaxial tensile test it can be seen that contrary to the statements by Alsos and Amdahl [22] the value of the triaxiality is not a constant $\frac{1}{3}$, meaning that the stress state is not pure tension. This can be explained by the fact that the idea of a uniaxial stress state is an idealised concept, since transverse contraction also induces stresses in the other two directions. The through-thickness stress can be very small to zero in case of plain stress conditions, but the second in-plane stress usually cannot be neglected, especially in the plastic region. Thus, the biaxial stress state renders the uniaxial failure strain as being inaccurate in theory, as Tørnqvist [13] mentions. However, in most cases the easy and inexpensive use is considered the crucial point compared to the error introduced by this approach. Furthermore, Tørnqvist [13] states that the highest possible triaxiality that a usual shell element can arrive at is $\frac{2}{3}$. This is because shell elements are based on a plane state of stress concept and thus cannot model a through-thickness stress correctly. Despite this deficit, simulations have according to Tørnqvist [13] shown that the RTCL-criterion can model propagating cracks well.

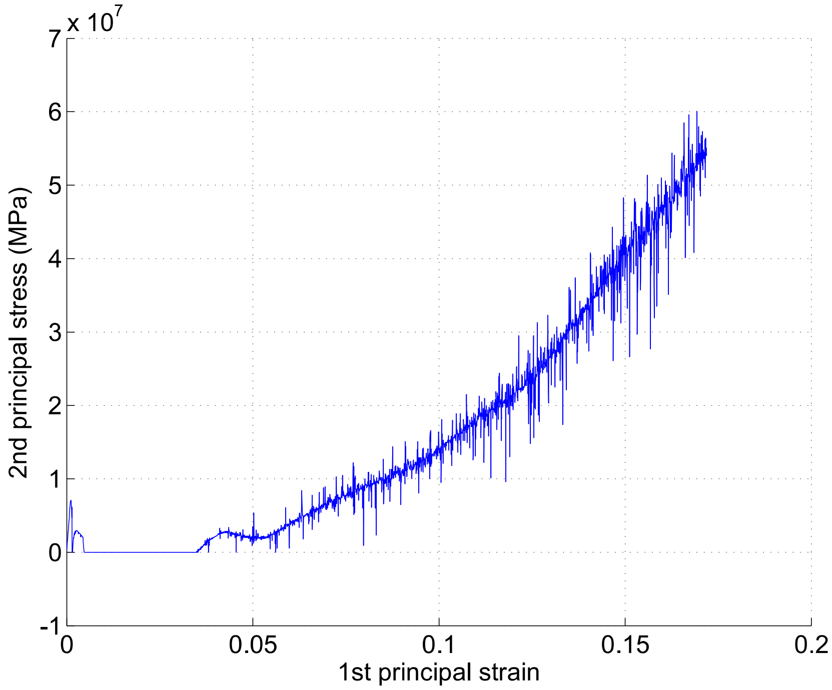

Fig. 11. Observed oscillating behaviour of the 2nd principal stress σ_2 for l = 50 mm and t = 5 mm.

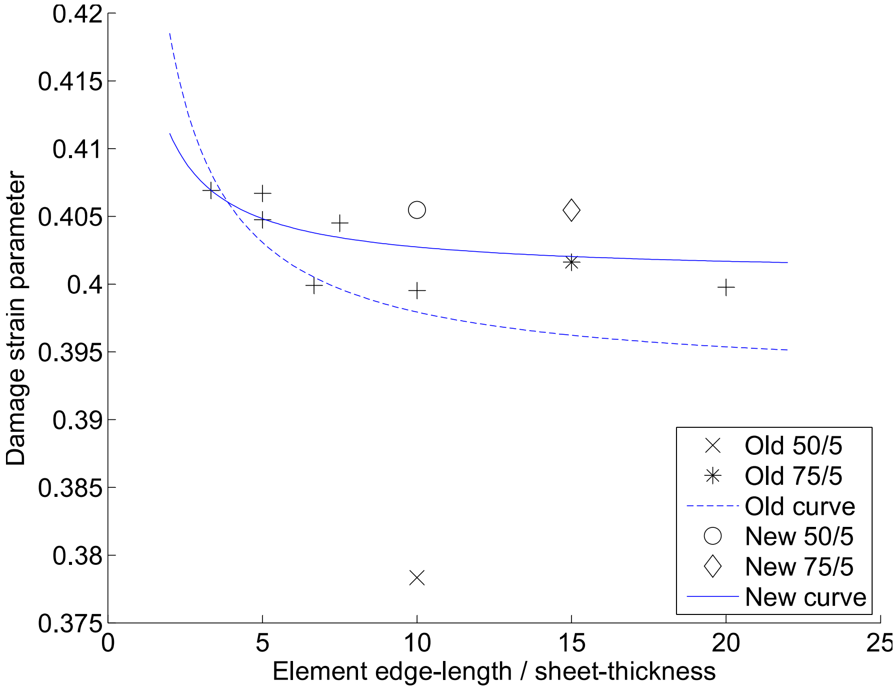

Fig. 12. Dependence of ε_0 on the ratio $^l/_t$. Old results were determined from the first series of simulations, new ones from the scaled tests.

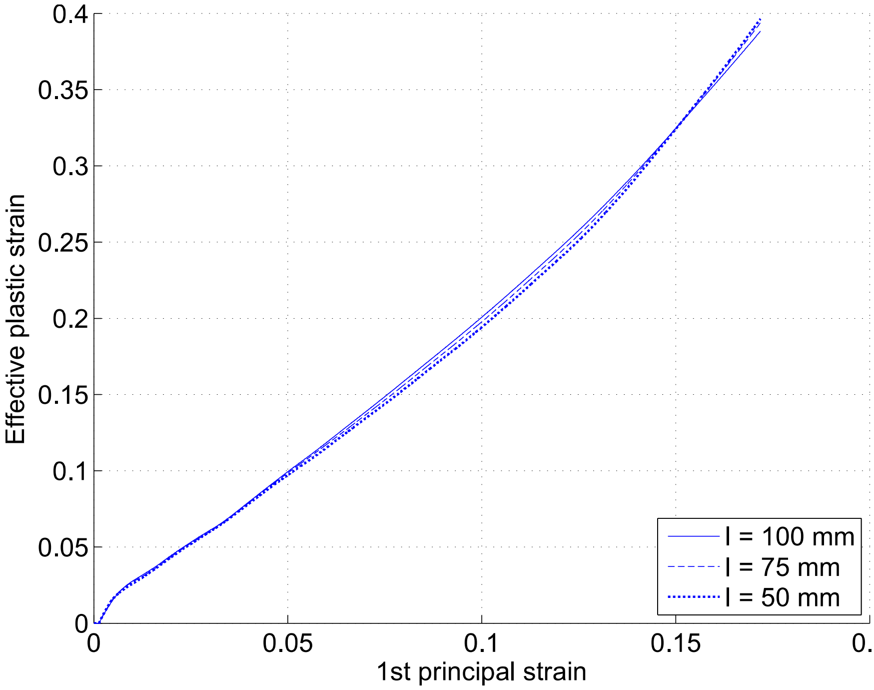

Fig. 13. Evolution of effective plastic strain until failure at the point of fracture over global strain for all three sheet thicknesses.

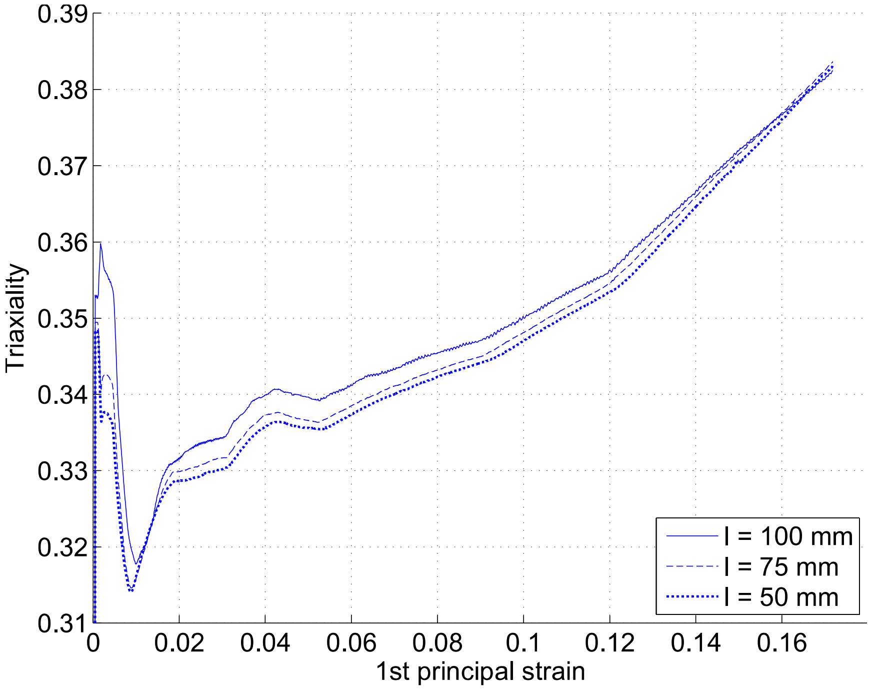

Fig. 14. Triaxialities over global strain for *t* = 15 mm.

4. Development of models for simulation of ship collisions

The explicit calculations of collision situations in LS-DYNA were carried out incorporating three different models: a bulbous bow of the striking ship, a conventional double-hull design that is currently in use (e.g. in yard number 743, cf. Fig. 15), and a novel double-hull design in order to verify the increased crashworthiness that this structure is intended to provide. The actual double-hull was different for both hull models, while the deck structures and the double bottom were the same. All models were entirely modelled with four-noded Belytschko-Lin-Tsay shell elements with one in-plane integration point and five integration points through the thickness. This element type offers a very high degree of computational efficiency while still being accurate (cf. LSTC [26]), so that it has become the default element type used in collision simulations, as Ehlers et al. [24] mention. Both hull models were limited to eight sections, i.e. nine web frames (the distance between two web frames was x = 2400 mm), cf. Figs 19, 23 and 24. This would allow for sufficiently short calculation times. This was important since the investigated methods should be implemented into the project process and thus calculation times should be as short as possible.

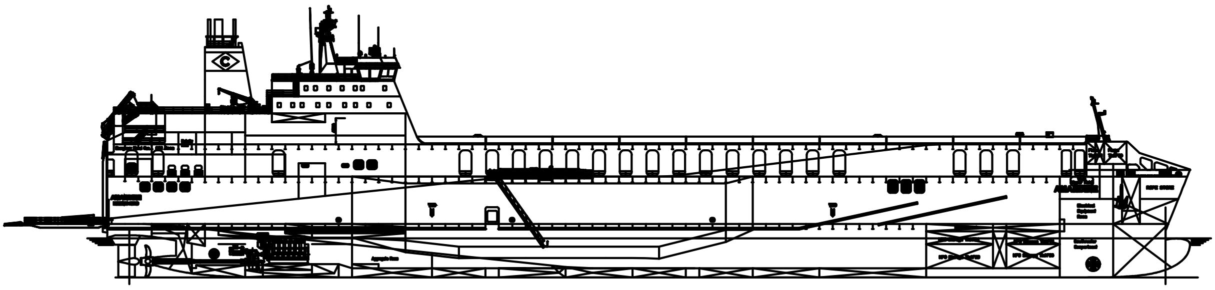

Fig. 15. General plan view of FSG yard number 743 from starboard.

4.1. Bulbous bow

Figure 16 shows the unmeshed model of the bulbous bow; lines in the model are plate joints.

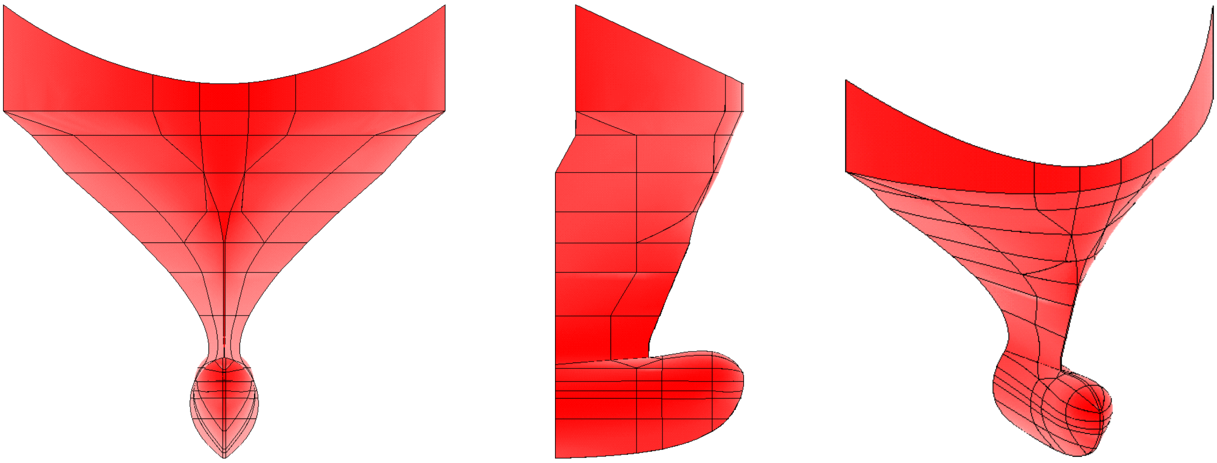

(a) **(b)** **(c)**

Fig. 16. Front (a), side (b), and angular (c) view of the bulbous bow model.

The bow was taken from FSG yard number 746 "Seatruck Progress" (cf. Fig. 17), frames 184 to 196+669 mm. This vessel has a length over all of 142.0 m, a breadth of 25.0 m, and a design draught of 5.2 m. The cargo can be divided onto four decks with a total number of 2166 lm (lane metres). It was imported as an IGES model and adapted for use in ANSYS. This means that the areas that the imported bow consisted of had to be connected to each other since every area was defined by a separate subset of keypoints and lines.

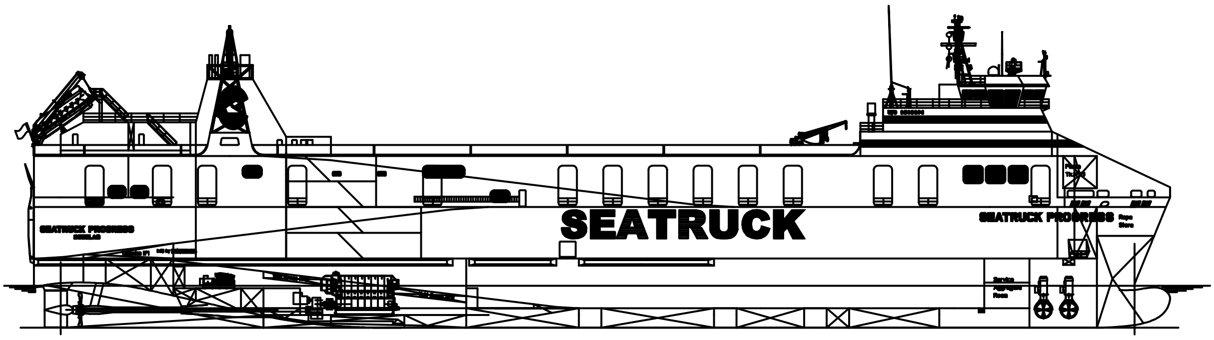

Fig. 17. General plan view of FSG yard number 746 from starboard.

Afterwards, the bow was assigned the rigid body property. This way it would not dissipate any plastic energy upon collision by deformation. Therefore, by prohibiting any plastic deformation of the bow a worst case scenario, and thus a conservative result with respect to large damage caused to the struck vessel, could be expected. Furthermore, the density of the shell model was scaled up according to Eq. (22). The bow had, due to its sheet thickness and the general material properties of steel mentioned in Section 3.1, a mass of $m_{shell} = 46 \times 10^3$ kg, and by scaling up the density it possessed the mass of the entire ship so that its kinetic energy assumed a realistic value.

$$\rho_{bow} = \rho \frac{m_{ship}}{m_{shell}} = \rho \frac{12.114 \times 10^6 kg}{46 \times 10^3 kg} \approx 263.35 \rho \tag{22}$$

The bow was meshed with a mean element edge length of 500 mm; see Fig. 18 for the mesh.

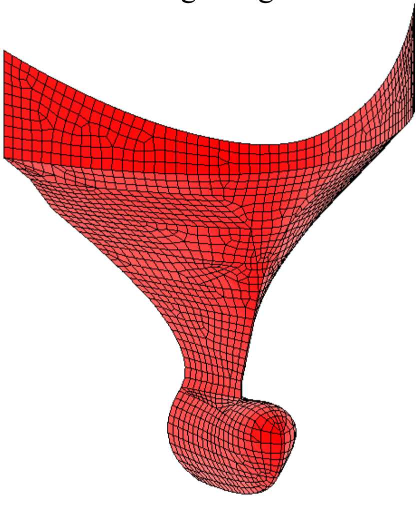

Fig. 18. Meshed geometry of the bow section.

4.2. Conventional double-hull design

Figure 19 shows the unmeshed and meshed geometry of the conventional double-hull design. The model was built after drawings of FSG yard number 743 "Amandine" (cf. Fig. 15). This vessel has a length over all of 195.4 m, a breadth of 26.2 m, and a design draught of 7.05 m. The cargo can be divided onto three decks with a total number of 2907 lm (lane metres).

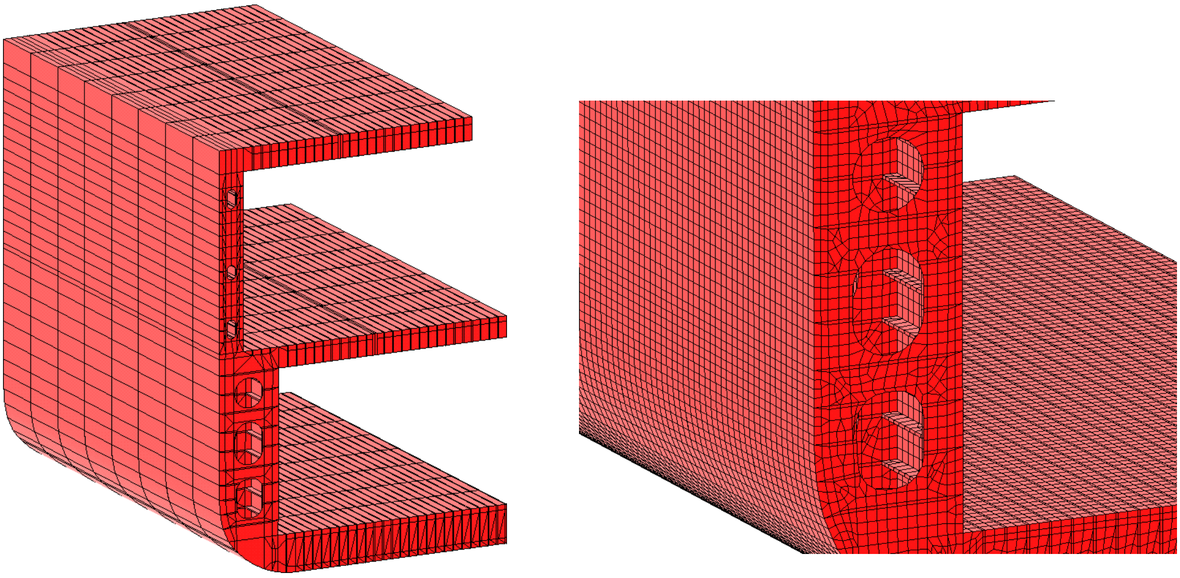

(a) (b)

Fig. 19. Unmeshed (a) and detail of the meshed (b) geometry of the conventional hull.

Full modelling of HP-sections (cf. Fig. 20a) would have led to very small elements, which, in turn, would have resulted in an unfeasibly small time step (cf. appendix, section *Explicit time integration*). Therefore, all HP- sections were replaced by L-sections (cf. Fig. 20b) while for all replacements the overall length and the web thickness of the respective HP-section was preserved, i.e. $h_{web} + t_{flange} = b$ and $t_{web} = s$ (cf. Fig. 20). This is the usual approach at FSG and the last part of the current thesis also deals with how well this procedure can be further simplified. It should be noted that modelling the sections with beam elements would have led to inaccuracies since if a beam impinges a shell perpendicularly its degrees of freedom are transferred incorrectly.

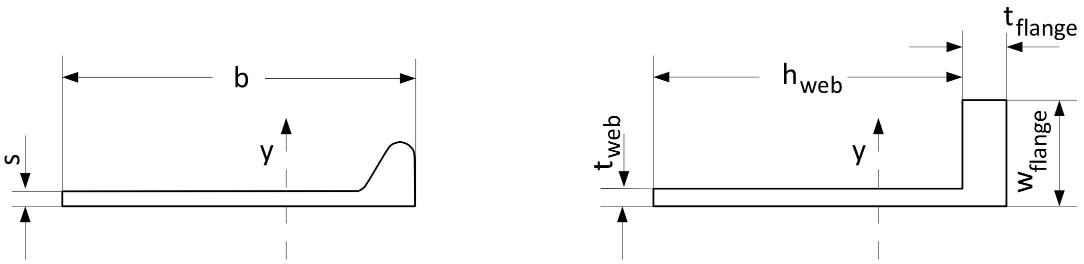

(a) (b)

Fig. 20. HP-section (a) and L-section (b). *y* denotes the important inertia axis.

The resulting dimensions of the L-sections as well as the errors of inertia and cross-sections can be seen in the appendix, Table 5. All errors were below 0.5%, which was considered sufficiently small.

4.3. Novel double-hull design

There are several novel designs of double-hulls that are intended to improve crashworthiness (cf. for example Klanac et al. [27] and Karlsson [28]). After consultation with FSG's steel design department the x-core structure was chosen among those as the novel double-hull design to implement. The reasons for this are that firstly, the design has according to Ehlers et al. [29] already been tested in the *Crashcoaster* project carried out in the European Union (cf. Vredeveldt [1]). A completely new design which has not been tested could possibly be unsuitable. Secondly, for FSG it is the most feasible design from both the manufacturing and the economic point of view, since it was shown by Ehlers et al. [29] that the structure can be manufactured by laser welding. Therefore, a sufficiently high processing speed can be assumed.

A detailed view of the modelled structure can be seen in Fig. 21. All dimensions were taken from Ehlers et al. [29] and built in as parameters. This means that, since the goal was to decrease the total thickness of the double-hull to gain additional cargo-space, all dimensions of the inner x-core-structure were formulated as relative quantities being dependent on the hull spacing to be easily adjustable. The initial hull spacings used were the same as for the conventional hull (lower hold and the deck above, respectively) to be able to compare results directly. Modelling of the welds was omitted.

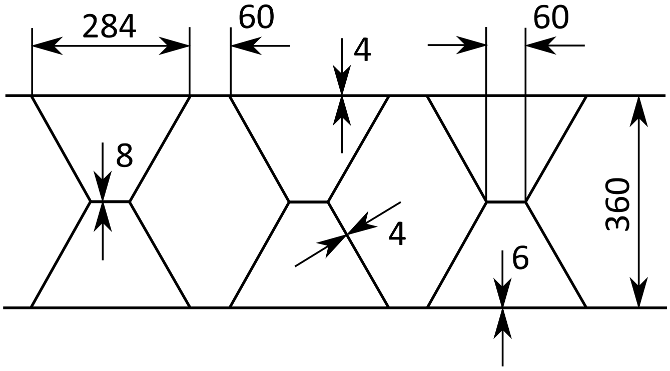

Fig. 21. X-core structure as proposed by Ehlers et al. [29], all dimensions in mm. The outer shell is at the bottom, the inner one at the top.

The process of building the hull from parameters input by the user is schematically shown in Fig. 22. First, the input values are formulated relative to the hull spacing, all ratios being based on the structure proposed by Ehlers et al. [29]. Subsequently, the hull segments belonging to lower section and deck, double-bottom, and upper section and deck are created consecutively by first determining the optimum number of x-cores through Eq. (23) so that the necessary degree of scaling is minimised. h_{user} is the height of a section input by the user, and h_{core} and $h_{spacing}$ are the heights of a core and the spacing between two cores, respectively. *nint* is a function offered by ANSYS that returns the integer that is closest to its argument.

$$n_{core}=nint\left(\frac{h_{user}}{h_{core}+h_{spacing}}\right) \tag{23}$$

In the next step each respective hull segment is built by creating one core and copying it the optimum number of times that was previously determined. Lastly, the height of the hull segment is scaled to match the original input value. At this point, one frame of the hull has been created, which is then copied in the global x-direction the input number of times. As the very last step the geometries of both decks and the double-bottom are imported and connected to the hull.

Figures 23 and 24 show both the unmeshed geometry and a detail of the meshed geometry of the widely and narrow spaced novel double-hull design, respectively. It should be noticed that the curvature at the bilge is not modelled. The reason for this is that maintaining the easy scalability of the model was considered more important.

In a conventional structure ballast tanks are arranged in the lower part of the double-hull. These are not modelled in the x-core structure since there is no measured data available describing the behaviour of the structure with water-filled tanks. Therefore, only the structure's characteristics are investigated and ballast water damping effects are not incorporated. More practical suggestions for the structure are given in Chapter 8.

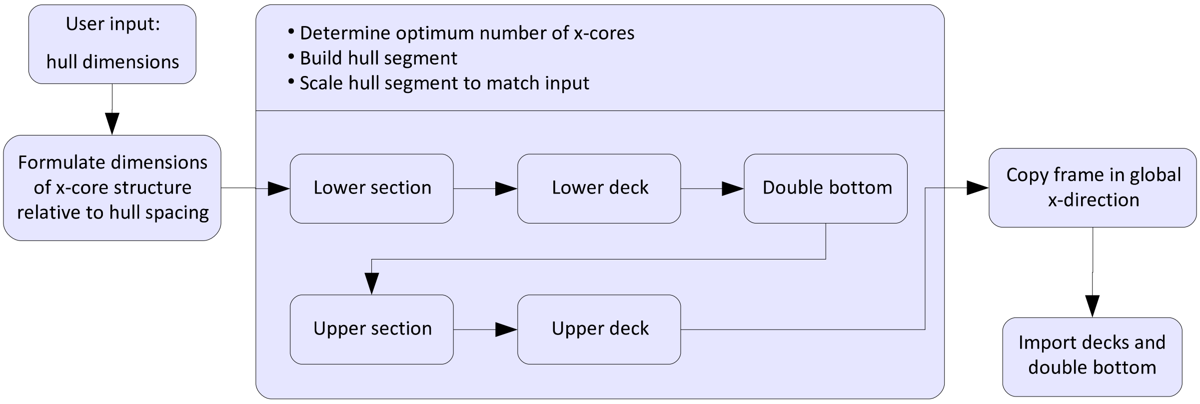

Fig. 22. Building procedure of the x-core double-hull.

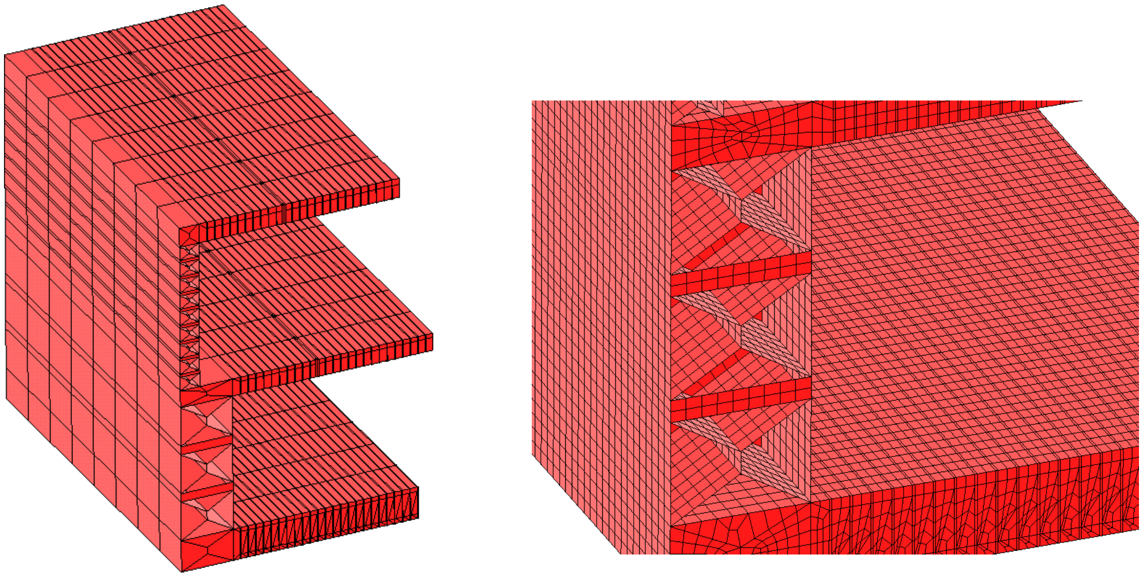

(a) **(b)**

Fig. 23. Unmeshed (a) and detail of the meshed (b) geometry of the widely spaced x-core hull. For clarification of the meshed x-cores parts of the foremost frame's wall are hidden.

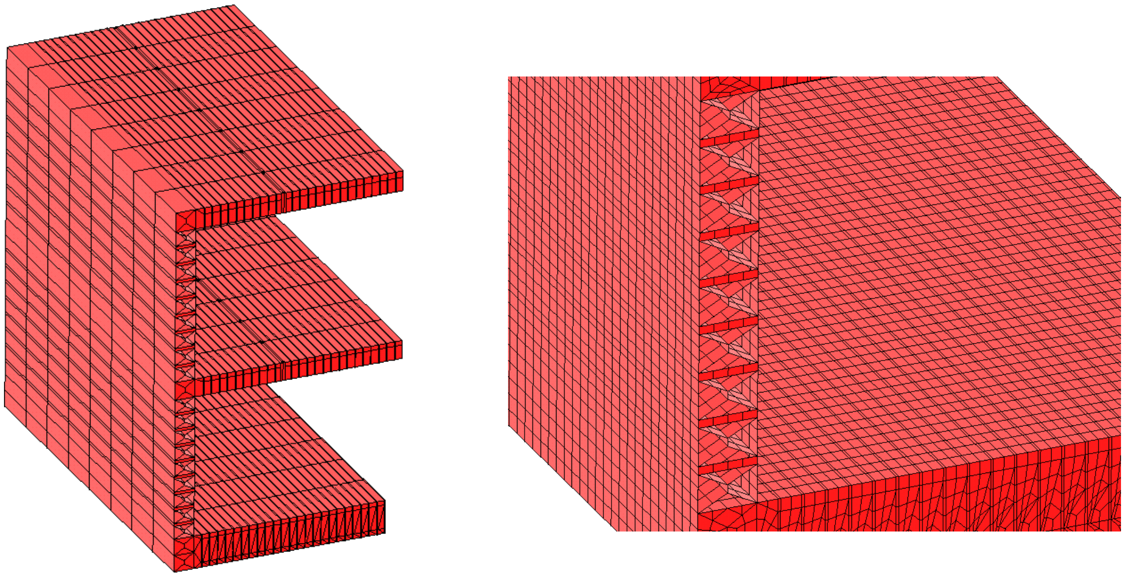

(a) **(b)**

Fig. 24. Unmeshed (a) and detail of the meshed (b) geometry of the narrow spaced x-core hull. For clarification of the meshed x-cores parts of the foremost frame's wall are hidden.

5. Calculation of collision situations

The calculations were done with LS-DYNA, version ls971d R5.0 (cf. LSTC [26]), under Microsoft Windows Server 2008 R2 Standard 64bit on an Intel Xeon E5450 quadcore CPU with a clock rate of 3GHz and 16GB of RAM. All calculations made use of the explicit time integration algorithm (cf. appendix, section *Explicit time integration*) implemented in LS-DYNA, cf. LSTC [26, 30].

Two different contacts were used in the simulations: automatic node-to-surface and automatic single surface. The first algorithm checks if nodes of one part (slave side) penetrate the other one (master segment). The second one checks if nodes of the slave side penetrate segments of the same side, meaning that the algorithm checks if a part penetrates itself. This is important for simulating the behaviour of folding structures correctly. The option automatic causes LS-DYNA to check both sides of shell elements for penetrations and to take the sheet thicknesses in the contact determination process into account (cf. LSTC [26]). Elements that failed and nodes which were no longer connected to at least one element were removed from the model by the algorithm. This procedure is, according to Tørnqvist [13], state of the art.

Karlsson [28] mentions that a kinetic friction coefficient of $\mu_k = 0.3$ has been shown appropriate for collision simulations. To determine the differences between the results of calculations regarding and disregarding friction, the first series of simulations was done with $\mu_k = 0$, the third one with $\mu_k = 0.3$ (cf. Table 1). The approach disregarding friction was expected to yield a differing increase in internal energy in the hull structures, since friction between the bulbous bow and the hull and inside the inner structure of the hull would consume additional energy. In addition, both series were expected to yield different failure modes, such as differing buckling, shearing, and tearing behaviour. Moreover, the differences between an impact perpendicular to the hull ($90°$) and under a collision angle of 75° were investigated. External dynamics such as inertia effects of the surrounding water and movement of the struck ship were generally neglected. The striking speed was set to 5 m s^{-1}. At FSG the mean element edge length typically lies in the range 100 mm $\leq l \leq$ 200 mm and was set to 200 mm for the calculations.

Two draughts were used, which can be seen in Fig. 25. The bow illustrated by the solid outline has its keel 1650 mm above the struck ship's keel, sliding on the double bottom. This draught describes the struck ship's design load case. The bow illustrated by the dashed outline lies 2 m above this, representing the heavy load of the struck vessel. The collision situations, for which calculations were carried out systematically, are shown in Table 1. Each checkmark denotes a set of three calculations which incorporate the GL-approach, as well as both failure criteria.

Both hull models were constrained with symmetry boundary conditions: the foremost and sternmost frames in x, the free edges of the decks (the edges close to the centreline) in y, and the bottom in the z-direction (cf. Fig. 29). This means that, for example for the first case, displacement of the nodes in the x-direction, as well as rotations around the y and z-axes were constrained. For each failure criterion two collision situations were calculated simulating an impact directly on a web frame, and between two web frames with equal distances to both of them. Each calculation was run either until the bulb penetrated the inner shell of the hull segment belonging to the lower hold, or, in case all of the bow's kinetic energy was consumed, until the bow stopped moving. The latter occurred for the widely spaced x-core structure (2700 mm) due to the relatively thick sheets, due to which this spacing was not pursued any further. Instead, its results could be used to examine the failure criteria's sensitivity (cf. Section 6.1).

After each calculation it was checked if the boundary conditions mentioned above influenced the results. This was done by inspecting different contour plots showing the distribution of effective displacement and internal energy increase, respectively. For both GL and PES these plots showed a value of zero up to at least half a section (1200 mm) away from the boundaries (cf. Fig. 30). However, this was not the case for RTCL at the lower draught for the conventional structure. Instead, excessive plastic deformation was observed, which also displaced the free edges so that the results were influenced. The reason for this was most likely the narrow range of parameters that Eq. (21) delivered. To resolve this issue, the calculations were repeated with a model that was extended in both the positive and negative x-directions. To do so, the respective frames on both sides of the mid web frame were copied, so that the model eventually consisted of sixteen sections, i.e. seventeen web frames (cf. Fig. 26). Subsequently, the model was tested if comparability to the short hull structure was maintained, since otherwise the resulting absorbed energies would not be useful. To do so, a calculation utilising PES and simulating an impact between two web frames was carried out on the extended hull. This situation would, due to PES, influence a large part of the structure and due to the impact between two web frames be closest to the boundary of the shorter structure. A comparison of the total energies absorbed by the shorter and the longer structure showed very good agreement, so that comparability regarding energy absorption was maintained. This way the shorter structure could be regarded as a detail of the longer hull. The calculations revealed differences for RTCL in the total absorbed energies between normal and large hulls in the range of 6% to 7%. However, this procedure also led to considerably increased calculation times for the respective collision situations. This means that the calculation times for RTCL at the upper draught were, contrary to the absorbed energies, not comparable any more.

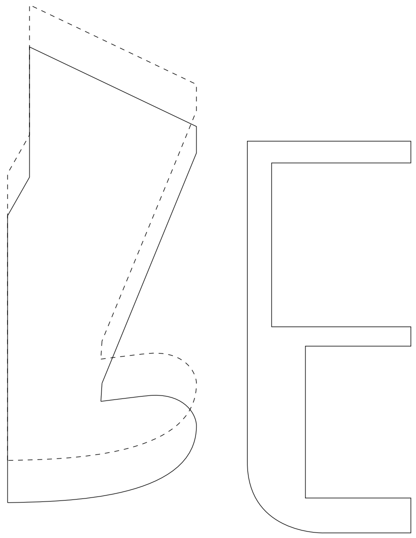

Fig. 25. Schematic view of the draughts used in the collision simulations.

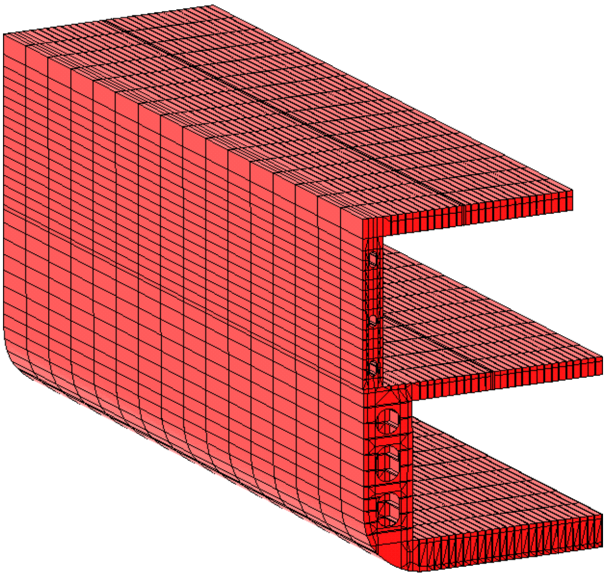

Fig. 26. Unmeshed geometry of the extended conventional hull.

5.1. Collisions perpendicular to the ship's side

At first collisions were simulated with the striking bow moving perpendicularly to the ship's side, meaning that the collision angle was $\Phi = 90°$. The bow was constrained (in the x- and z-directions of the struck ship's coordinate system, (cf. Fig. 29) to not twist around or move along undesirable axes upon collision, but only move along the y-axis. The calculations were done with the conventional and the x-core double hull, the latter using two different hull spacings. These spacing were chosen as 2700 mm, which is the spacing of the conventional hull at the lower hold, and 1000 mm, which is the spacing of the conventional hull at the deck above (cf. Fig. 19).

5.2. Collisions from an angular direction

To determine how the structures react to impacts that do not occur perpendicularly, calculations were done at an impact angle of $\Phi = 75°$, meaning that the angle was deviating $15°$ from the hull's normal angle. The bow was constrained (in the z-direction of the struck ship's coordinate system, cf. Fig. 29) so as not to move up or down upon collision. The calculations at an angle of $\Phi = 90°$ showed that the widely spaced x-core structure causes a behaviour not observed in real collisions due to its very thick sheets. These thicknesses are not used practically and hence the structure was taken into account in none of the following calculations. Instead, the difference between the behaviours of a wide (conventional) and a narrow (x-core with a hull spacing of 1000 mm) hull were pursued. If the masses of both the widely and narrow spaced x-core structure are considered, the differences between these structures are even more obvious. The mass per square metre of the narrow spaced structure is $m_{1000} \approx 462$ kg m^{-2}, while the mass per square metre of the widely spaced one is $m_{2700} \approx 1255$ kg m^{-2}.

5.3. Collisions incorporating friction

All calculations described in the two previous sections were done without friction. To be able to investigate differences in the results when regarding and disregarding friction in the simulations, a dynamic friction coefficient of $\mu_k = 0.3$ was introduced. Thereafter the collision situations under an impact angle of $\Phi = 90^\circ$ were repeated for the conventional and the narrow spaced x-core structure.

5.4. Defeaturing of the conventional structure

To decrease calculation time and thereby increase performance the models had to be simplified. The x-core structure was already designed in a very simple fashion in the current study to be easily buildable. Thus defeaturing was not sensible here. Instead, the mesh could be coarsened to reduce computational effort and decrease computational time (cf. section 5.5). The conventional hull, on the other hand, showed much potential for defeaturing due to the detailed structure. Hence, all HP- (cf. Fig. 20a), L- (cf. Fig. 20b), and FL-sections (flat steel) were removed from the model (cf. Fig. 27b). This was done since the modelling of all sections and the adjustment of all other areas to them demanded by far the highest modelling effort and longest modelling time. The latter had to be done to ensure a coherent mesh. If areas form a free edge (cf. Fig. 28a) the resulting mesh will be incoherent, while the configuration of areas in Fig. 28b will yield a coherent one. The re-modelling (cf. Fig. 27c) reduced the calculation times for GL from 225 min to 39 min, for PES from 251 min to 68 min, and for RTCL from 397 min to 86 min (average values).

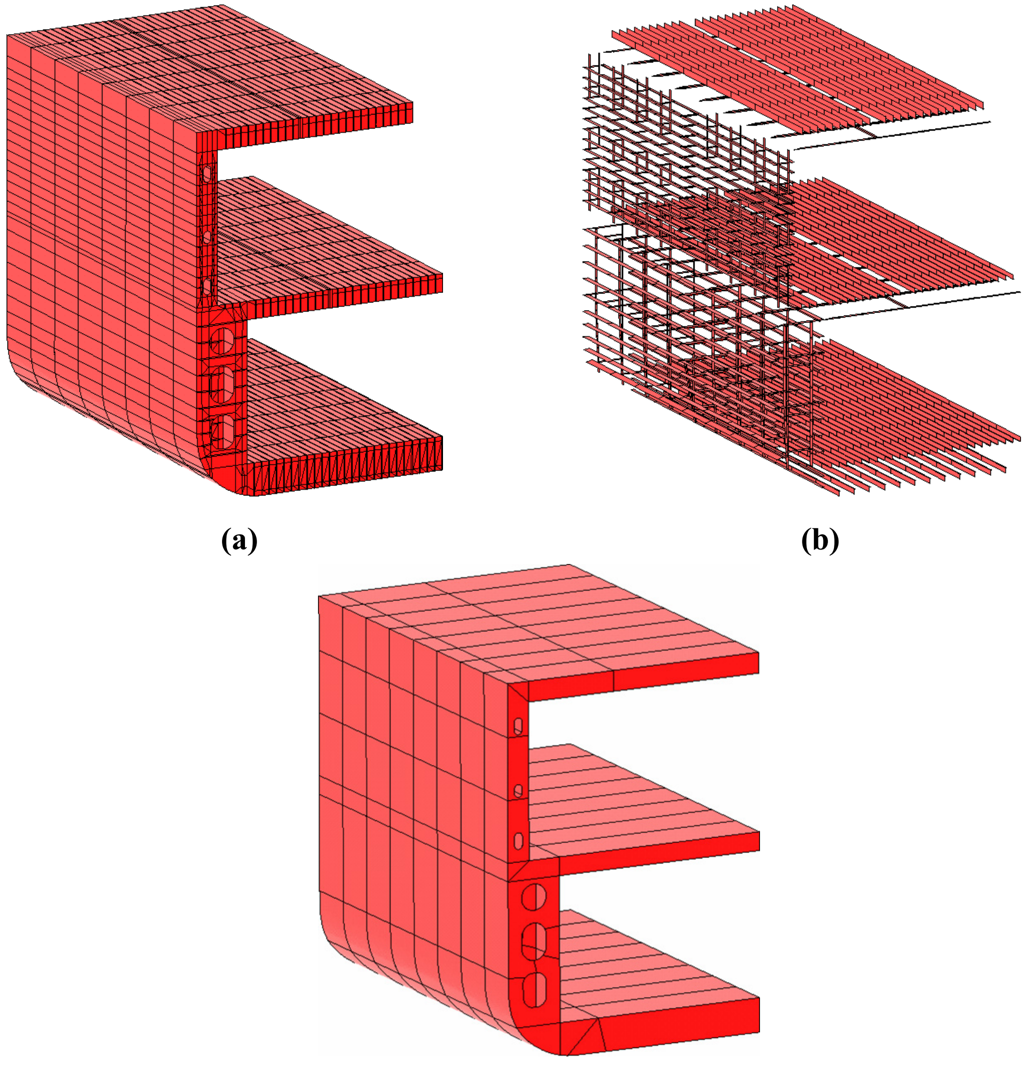

(a) **(b)**

(c)

Fig. 27. Hull having all HP-, L-, and FL-sections removed (a), removed sections (b), and revised hull (c).

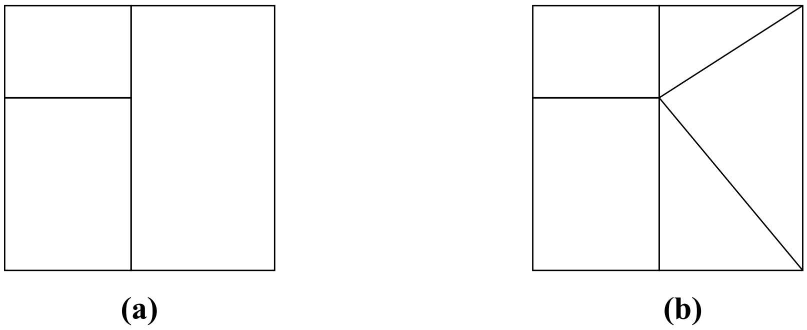

Fig. 28. Example of a group of areas with (a) and without (b) a free edge.

Therefore, if either a small error or a constant error that could be taken into account in future calculations was the result, this method would be valuable. All calculations were done under an impact angle of $\Phi = 90°$.

5.5. Coarsening of the mesh

The finer the mesh in a finite element model is, the better results, such as for example stress and strain values can be expected to be resolved. However, this also increases the required calculation time drastically, so that a compromise has to be found between accuracy and effort. Therefore, the collision situations for the narrow spaced x-core structure under an impact angle of $\Phi = 90°$ were repeated with two additional mesh densities. The original mean element edge length was l = 200 mm and discretisations of l = 300 mm and l = 400 mm were examined to find the savings in time, as well as the errors introduced by reducing the mesh density.

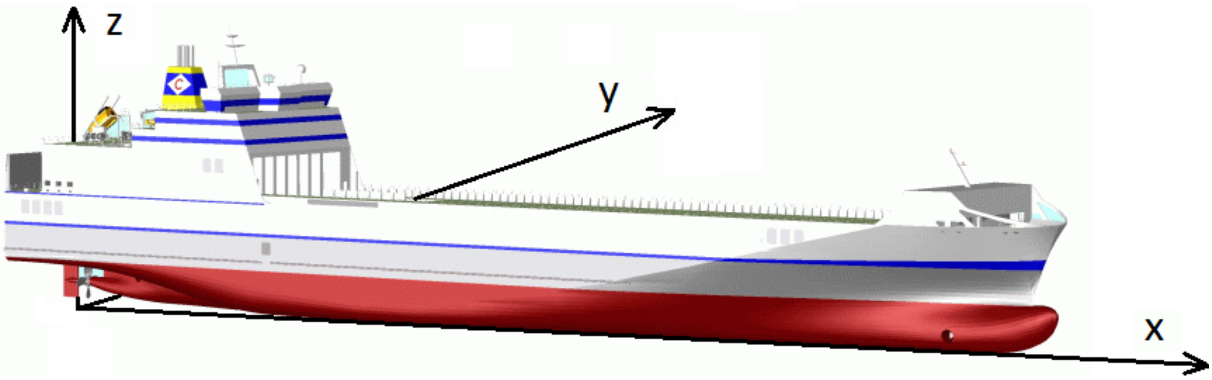

Fig. 29. Schematic view of a ship's global coordinate system. The origin is on a level with the keel in the rudder stock. The x-axis runs towards the bow, the y-axis towards port, and the z-axis straight upwards.

Table 1. Overview of systematically performed calculations. For each series all three failure criteria were studied. OW = impact on a web frame, BW = impact between two web frames.

Striking bow	Rigid											
Hull design	Conventional				X-core							
Hull spacing	2700 mm				2700 mm				1000 mm			
Draught	Lower		Upper		Lower		Upper		Lower		Upper	
	OW	BW	OW	BW	OW	BW	OW	BW	OW	BW	OW	BW
a)	✓	✓	✓	✓	✓	✓	✓	✓	✓	✓	✓	✓
b)			✓	✓							✓	✓
c)	✓	✓	✓	✓					✓	✓	✓	✓
d)	✓	✓	✓	✓								
e)	✓	✓	✓	✓								
f)									✓	✓	✓	✓
g)									✓	✓	✓	✓

Legend

a)	Full model, collision angle $\Phi = 90°$, friction disregarded ($\mu_k = 0$)
b)	Full model, collision angle $\Phi = 75°$, friction disregarded ($\mu_k = 0$)
c)	Full model, dynamic friction coefficient $\mu_k = 0.3$ introduced
d)	Defeatured model (all HP/FL/L sections removed)
e)	Defeatured and revised model (small areas merged)
f)	Full model, mean element edge-length changed to $l = 300\,\mathrm{mm}$
g)	Full model, mean element edge-length changed to $l = 400\,\mathrm{mm}$

All calculations were done with $\Phi = 90°$, $\mu_k = 0$, and $l = 200\,\mathrm{mm}$ if not stated otherwise

6. Results and discussion

6.1. Collisions perpendicular to the ship's side

Figures 31 and 32 show the total energies absorbed by the conventional and both the widely and narrow spaced x-core designs at the lower and upper draught, respectively. All energies were measured at the point of rupture of the inner hull. It can be seen that both for an impact on a web frame (Figs 31a and 32a) and an impact between two web frames (Figs 31b and 32b) the absorbed energy increases along the series GL $\rightarrow$ PES $\rightarrow$ RTCL. GL consumes the smallest amount of energy before failure, while RTCL consumes the largest amount. The energy consumed by PES lies in between these two, but especially the energy differences between the conventional structure and the widely spaced x-core structure (2700) are very large and even larger than for RTCL. This could be expected since PES prescribes a larger value for the failure strain than GL does. RTCL, in turn, always fails close to the experimentally determined failure strain due to the narrow range of the ε_0-parameter (cf. Section 3.5). This means that these criteria are totally (GL) and virtually (RTCL) independent of the sheet thickness, respectively, as Figs 10 and 12 already suggested, while PES strongly depends on it.

It can be seen that the energies absorbed by the widely spaced x-core structure are much higher than those absorbed by the conventional structure. This is because the structure proposed by Ehlers et al. [29] was taken and scaled up to match the spacing of the conventional hull (cf. Section 4.3). Accordingly, also the sheet thicknesses were scaled up in this process which makes the structure hardly usable in reality due to excessive weight. Instead, this structure is useful in demonstrating how sensitive the criteria are to input values. This is especially visible by the fact that the larger jump in absorbed energy compared to GL and RTCL causes the "curve" that is created by connecting the data points of PES with straight lines to change from convex to concave. This means that the curvature changes from positive to negative. This shows the dependency of PES on sheet thickness can be seen here, since the energy capacity of the structure and thus the failure strain increases considerably. RTCL should show a similar behaviour, since it is also dependent on sheet thickness. However, due to the absence of localised necking in the simulated tensile tests (cf. Section 3.5) the criterion assumed a very narrow parameter range, so that a dependency on sheet thickness or element edge length was virtually not accounted for. The total energies absorbed by the narrow spaced x-core structure (1000), on the other hand, are somewhat smaller than those absorbed by the conventional hull and the data points maintain a convex "curve". The difference is small for GL and increases via PES to the highest value for RTCL.

Generally, the total energy increases faster for both x-core double hulls than for the conventional hull (cf. Figs 39 – 40 and Figs 44 – 45), which shows their potential for a greater capability to absorb plastic deformation energy. Another general observation is that at the upper draught less total energy is absorbed than at the lower one and the effective displacement in the region that is hit by the stem is considerably smaller. This is because the part of the stem crashing into the hull is smaller than that at the lower draught and additionally it crashes later than the bulb does. Aside from this, the energy introduced by the bulb stays relatively constant regardless of the draught (cf. Figs 31 and 32). This is due to the fact that the bulb more or less cuts through the hull, as described below (cf. also Fig. 30). Thus, at the upper draught the energy introduced by the bulb has a larger fraction of the total energy than at the lower draught and therefore this situation is more critical for the lower cargo hold. If the energies introduced into the lower cargo hold's double hull by the bulb are considered, it can be seen that for almost all cases the narrow spaced x-core structure absorbs more energy than the conventional one. Thus, while its global crashworthiness is lower it offers a comparable energy to higher local crashworthiness.

In the course of the ELKOS project, practical tests utilising the bulb and one module only are planned to be carried out at TUHH. However, the simulations showed that the greatest part of the bow's kinetic energy is transferred by the stem, as the ratios between the energies introduced by stem and bow, respectively, suggest (cf. Appendix, Figs 41 – 43 and Figs 46 – 48). Thus, to be able to compare the results from these tests to those received in this investigation the mass of the bow has to be adjusted so that a comparable kinetic energy is maintained throughout the test, if not a constant testing velocity is used. The energies introduced by the stem are always larger than those introduced by the bulb (cf. Appendix, Figs 41 – 43 and Figs 46 – 48). The reason for this is that the stem possesses a much larger area than the bulb and presses a large segment into the structure while the bulb cuts through the hull like a knife. This effect can be seen in Fig. 30 where the effective displacement of the region around the point of impact of the bulb is small compared to that caused by the stem. Furthermore, the ratios between the energies introduced by the stem and by the bulb are generally inconstant. If friction is disregarded in the calculations, the change in kinetic energy of the bow equals the internal energy increase in the hull and an effective mass ratio between stem and bulb can be derived from the energy ratio. For a rigid body the velocity has to be the same at all points in the bodyso that energy and mass ratios are equal:

$$\frac{\Delta E_{Bulb}}{\Delta E_{Stem}} = \frac{\frac{1}{2} m_{Bulb} \times \Delta v^2}{\frac{1}{2} m_{Stem} \times \Delta v^2} = \frac{m_{Bulb}}{m_{Stem}} \tag{24}$$

This means that the effective mass of the bulb needed to reproduce the results obtained in this thesis is highly inconstant so that an exact accordance will most likely not be possible. Nevertheless, another possibility would then be to take the mean value of the energy ratio curve as a first approximation.

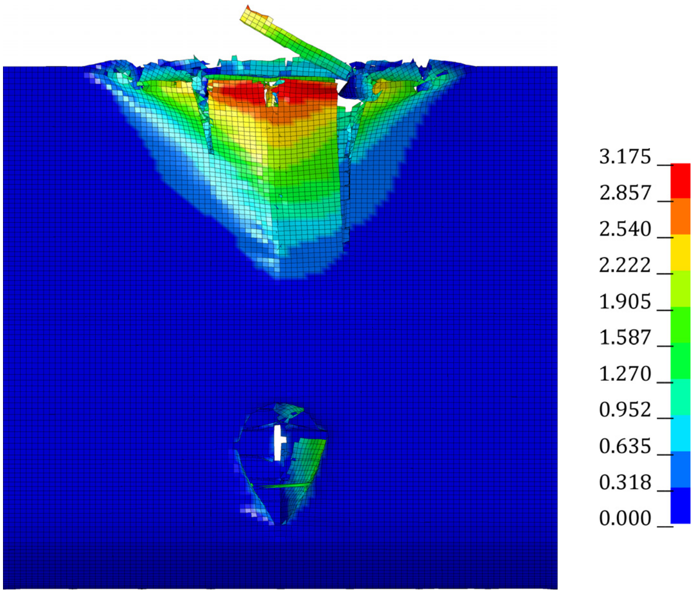

Fig. 30. Example of how the stem crushes a large part of the hull while the bulb cuts through it. Effective displacement is shown; the unit is m. Lower draught, hit on a web frame of the conventional hull, PES-criterion.

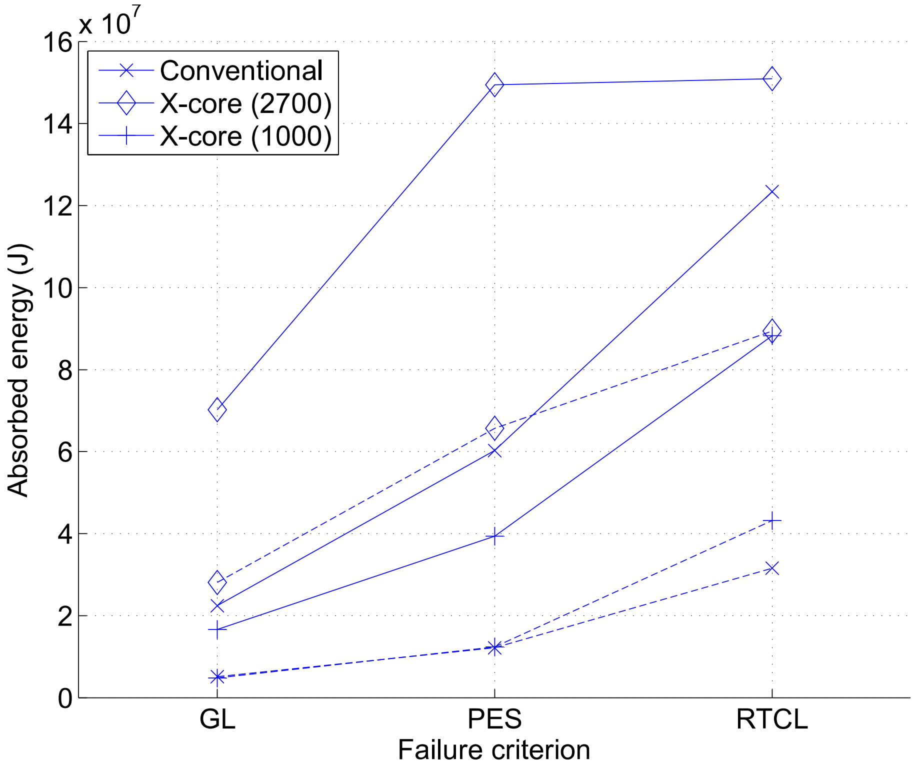

(a)

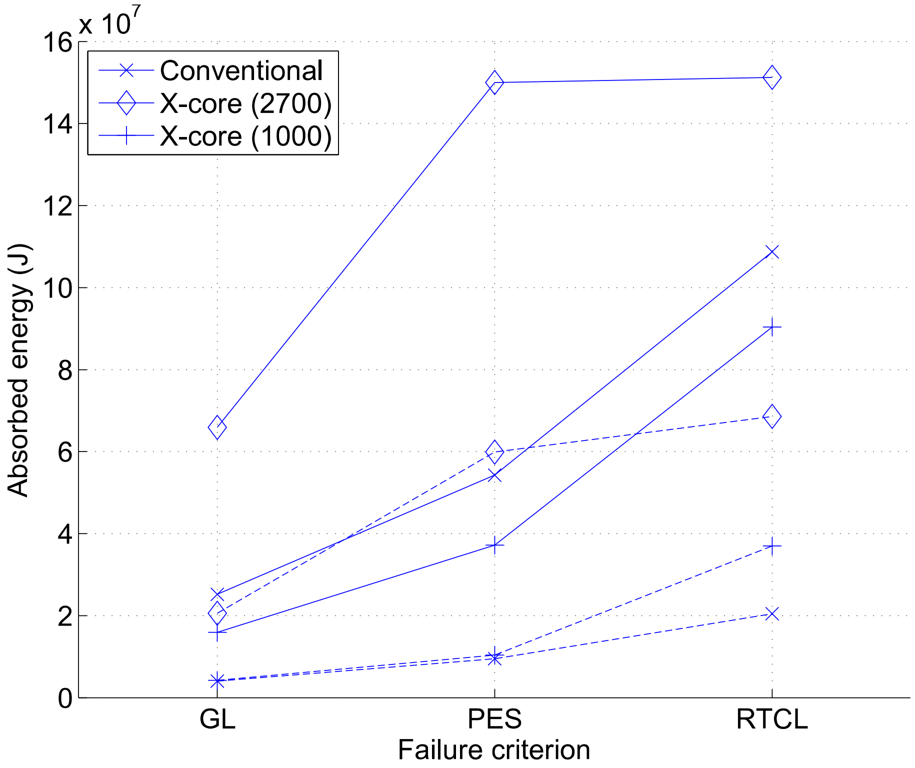

(b)

Fig. 31. Energies introduced into the structures by the entire bow (solid lines) and by the bulb (dashed lines) for the three failure criteria at the lower draught: impact on a web frame (a) and impact between two web frames (b).

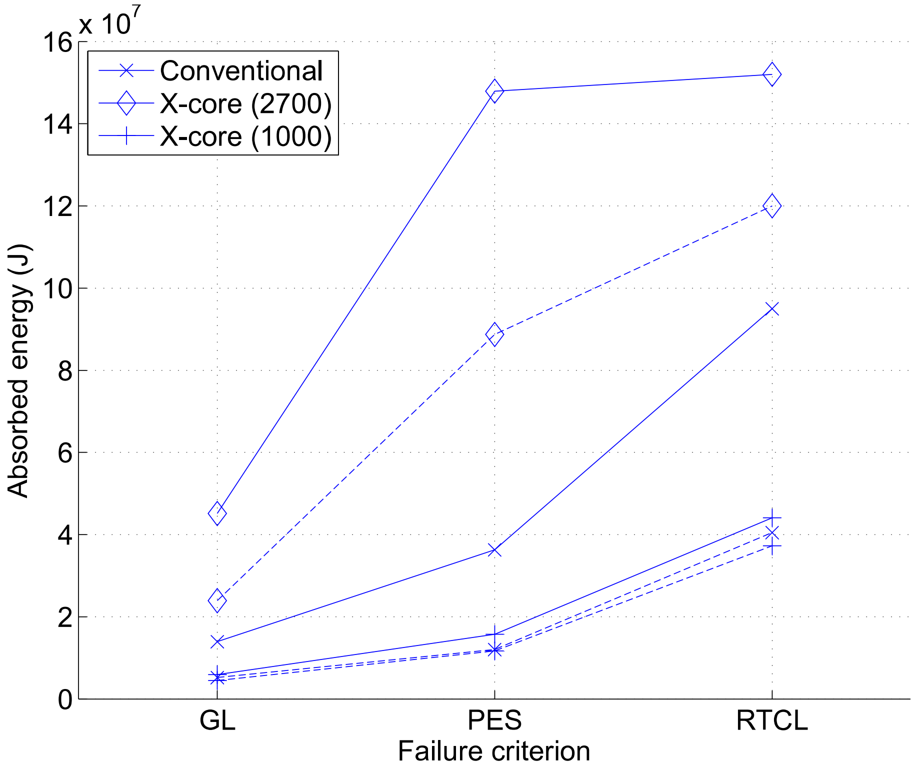

(a)

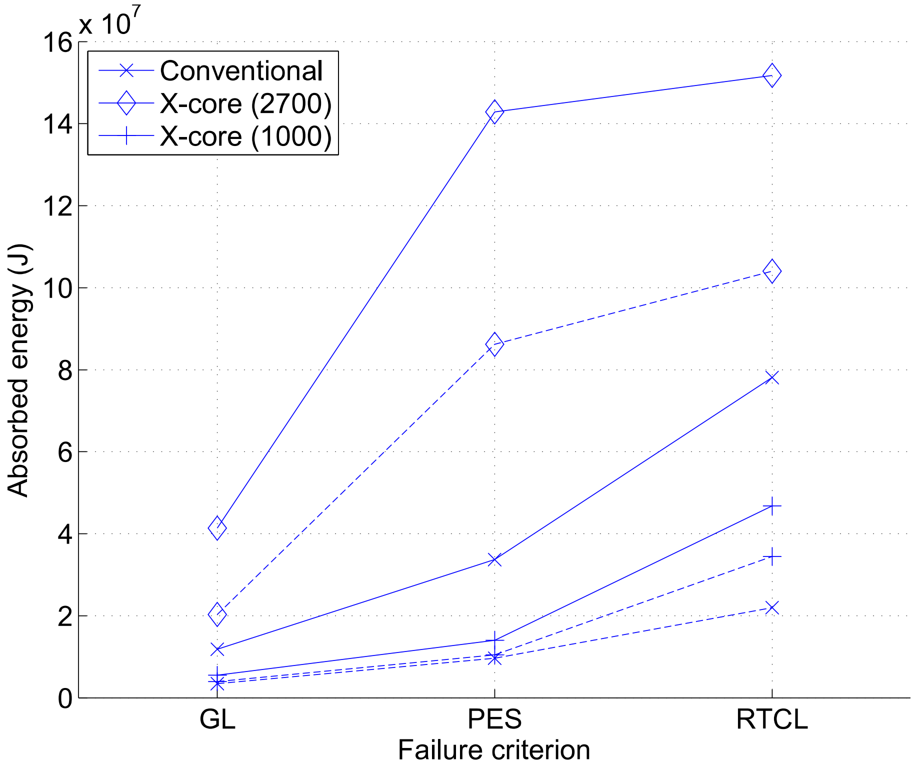

(b)

Fig. 32. Energies introduced into the structures by the entire bow (solid lines) and by the bulb (dashed lines) for the three failure criteria at the upper draught: impact on a web frame (a) and impact between two web frames (b).

As stated above, the upper draught is a more critical collision situation for the lower cargo hold than the lower draught. This is because at the upper draught the bulb transmits a larger fraction of the total energy. Therefore, at this draught, a comparison was made between the conventional hull and different x-core hulls with varying hull spacings but constant sheet thicknesses. These sheet thicknesses are originally from the hull spacing 1000 mm and are comparable to those of the conventional hull. Figure 33 shows that x-core structures with hull spacings of 1500 mm and 2000 mm constitute a window which the conventional hull lies in, meaning that as a first approximation the x-core double hull is generally capable of absorbing a higher energy than the conventional one. However, neither manholes for inspection nor ballast tanks are included in this single x-core structure. Suggestions as to how to resolve this issue are given in Chapter 8.

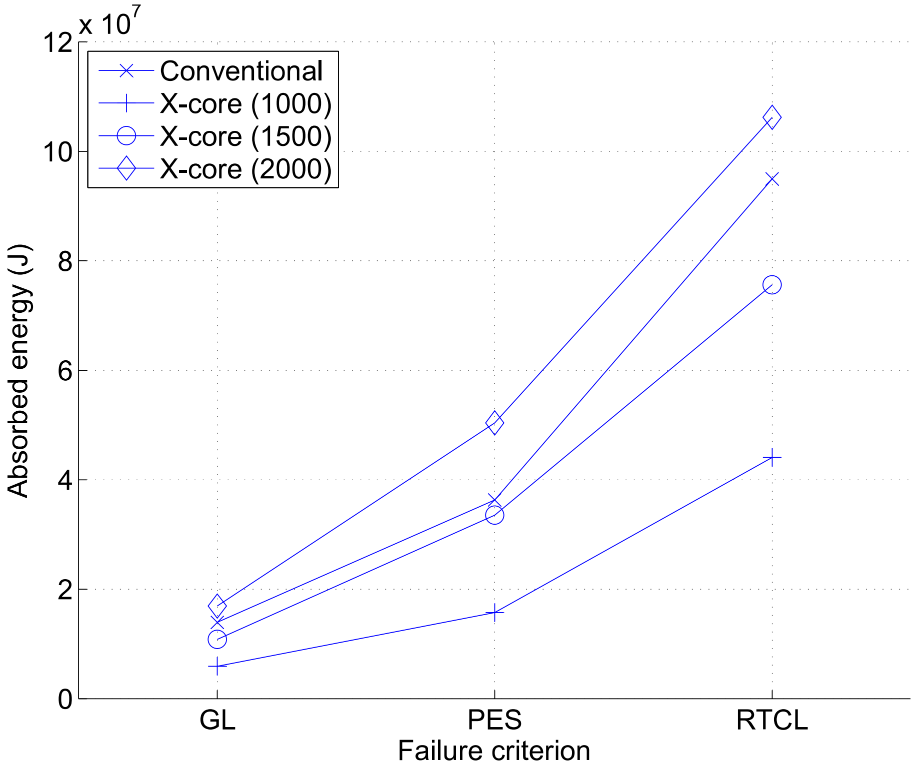

Fig. 33. Upper draught, impact on a web frame: comparison of energies absorbed by the conventional design and x-core designs of various hull spacings. The sheet thicknesses of the latter are similar to those of the former one.

6.2. Collisions from an angular direction

Figure 34 shows the energies introduced into a conventional and narrow-spaced x-core structure by the entire bow and bulb at the upper draught under an impact angle of $\Phi = 75°$. Generally, it can be seen that the energies were somewhat higher than at an impact angle of $\Phi = 90°$, which can be explained by the longer distance the bow had to cover before the inner hull fractured. Furthermore, the area of the stem that crashed into the hull was somewhat larger than that at $\Phi = 90°$. If the individual criteria are considered it can be observed that compared to a perpendicular impact the changes in energy were hardly noticeable for GL, only little for PES, and considerably for RTCL. This can be explained by the total amount of energy being absorbed by the structure, which increased from GL over PES to RTCL (cf. Section 6.1).

On the other hand, it can be expected that the absorbed energy will eventually drop if the collision angle is further decreased, since the striking ship will slide against and bounce off the struck ship instead of penetrating the complete hull. This would possibly cause only minor damage to the struck vessel.

6.3. Comparison of the results with Minorsky's method

The ratio between the energies absorbed at a collision perpendicular to the ship's side and collisions at an angle predicted by Minorsky's method is (cf. Eq. (6) and Fig. 2):

$$\frac{\Delta KE_{75°}}{\Delta KE_{90°}} = \left[\frac{\sin(75°)}{\sin(90°)}\right]^2 \approx 0.933 \qquad (25)$$

Figure 35 shows the ratios between the energies absorbed at collision angles of $\Phi = 75°$ and $\Phi = 90°$, respectively. It can be seen that except for one runaway value (x-core structure, impact on a web frame, GL-criterion) all ratios are larger than one which disagrees with the prediction deduced from Eq. (25). The reason for this is that the method does not take into account the longer distance that has to be covered at a collision from an angular direction. Instead, the squared sine function steadily decreases if the collision angle deviates from $90°$ This also complies with the statement by Pedersen and Zhang [31] that Minorsky's method disregards the structural arrangement. Furthermore, both the material properties and the damage mode are not considered [31]. However, as mentioned in Section 6.2 the energy ratio can be expected to decrease again with a further decreasing angle and thus follow the tendency given by the curve shown in Fig. 2.

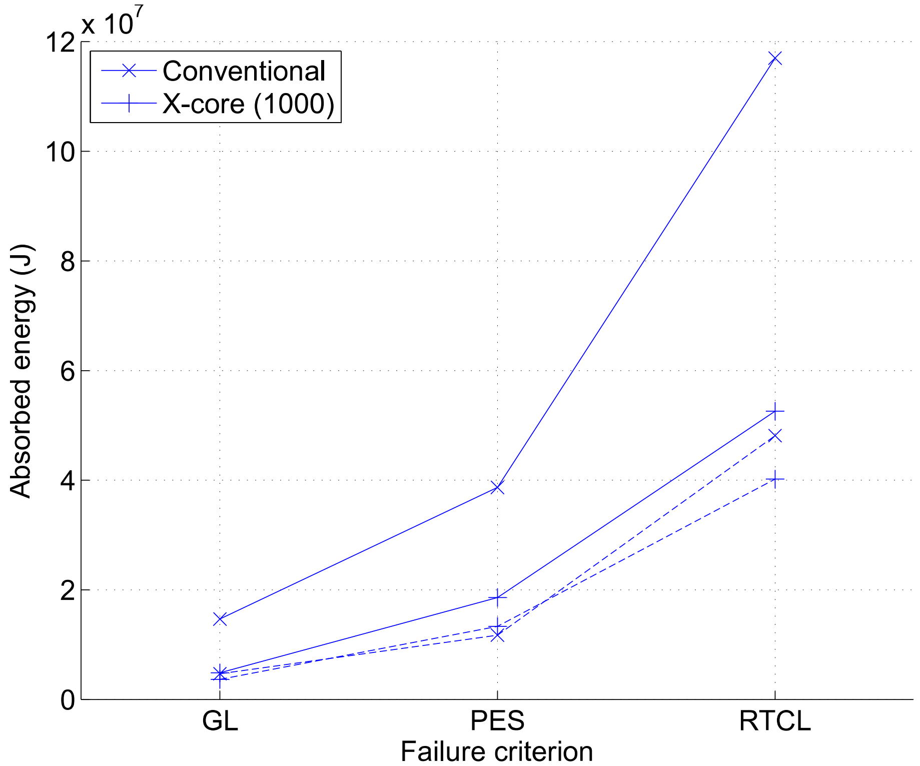

(a)

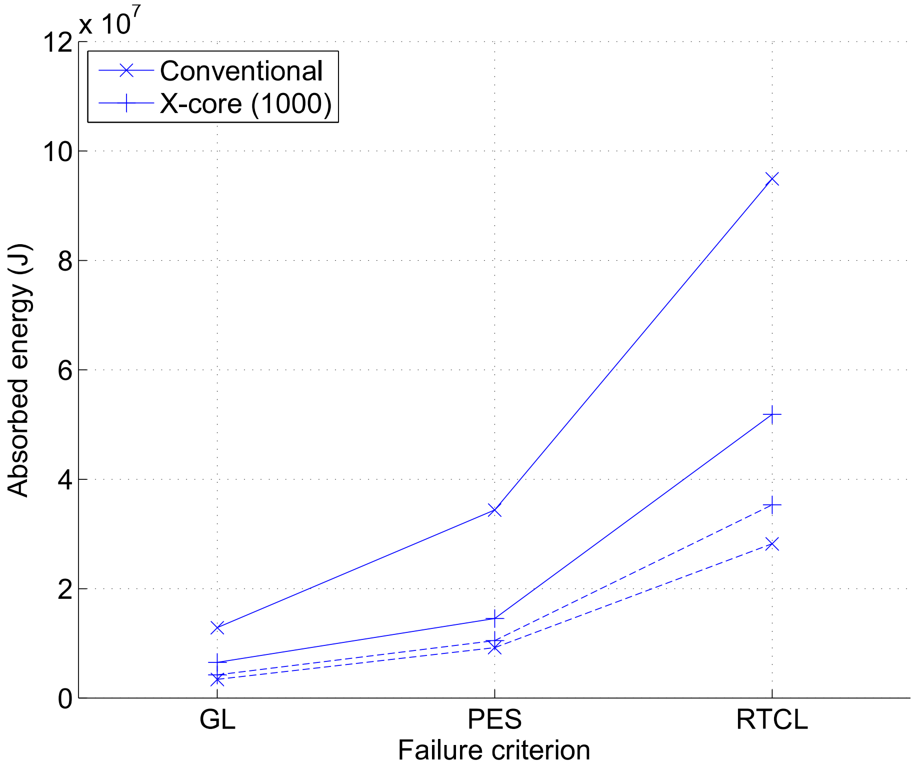

(b)

Fig. 34. Energies introduced into the structures by the entire bow (solid lines) and by the bulb (dashed lines) for the three failure criteria at the upper draught, impact angle $\Phi = 75°$ impact on a web frame (a) and impact between two web frames (b).

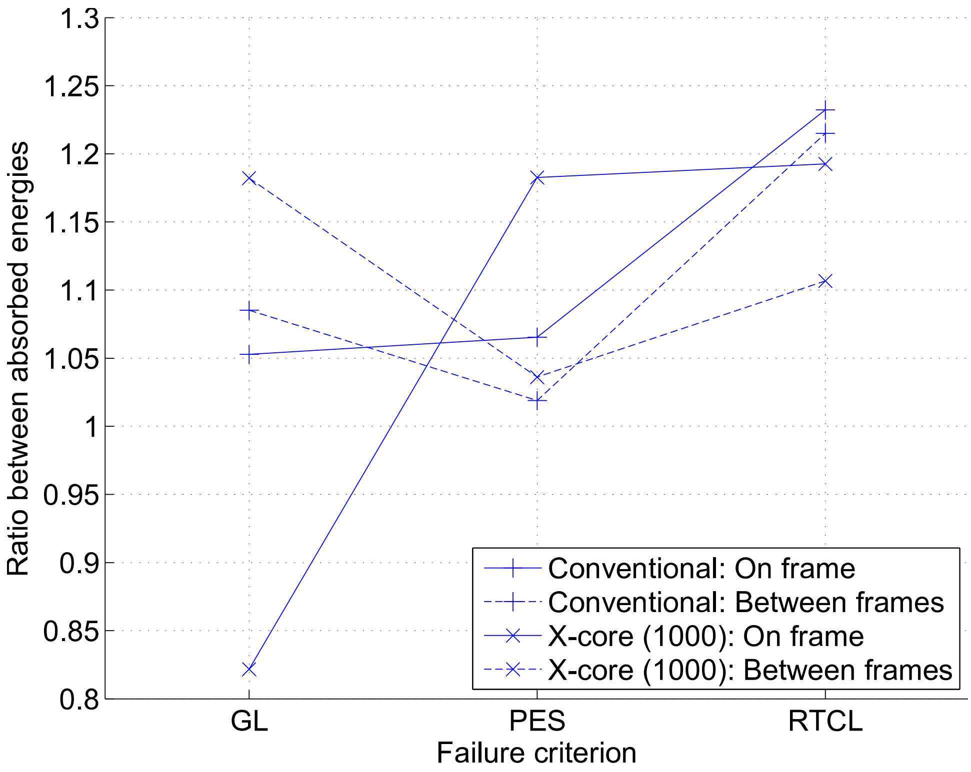

(b)

Fig. 35. Ratios between absorbed energies from collisions at $\Phi = 75°$ and $\Phi = 90°$ at the upper draught.

6.4. Collisions incorporating friction

The ratios between the total absorbed energies from the calculations regarding and disregarding friction (cf. Table 1 and section 5.3) are plotted in the Appendix, Figs 49 – 52, for the three failure criteria. It can be seen for all plots that the ranges covered by the energy ratios are very narrow; the largest interval occurs for the conventional hull at the upper draught sustaining an impact on a web frame with $\Delta \approx 0.039$. Furthermore, it could be expected that friction changed the set-up in such a way that more energy would be absorbed by the structure and thus the energy ratios would lie above one. Instead, it can be seen from the plots that all ratios oscillated around this value. Here it should be noted that the ratios for both GL and PES oscillated heavily and the ratio at failure of the hull lies above one in some of the situations and below in the others. RTCL on the other hand stayed, except for the conventional hull at the lower draught sustaining an impact on a web frame, almost constantly at a value of one. Therefore, no unambiguous conclusion can be drawn about the absolute effects of friction on the absorption of energy. Nevertheless, it can generally be said that in collision simulations comparable to those carried out in this investigation friction plays, from the energy point of view, only a minor role. However, the introduction of friction can change the failure mode. To investigate if this occurred, the point of impact of the bulb was examined from the inside and the outside of the double-hull. Additionally, the area of impact of the stem was examined from the inside and the outside. For both locations and for all three criteria no apparent differences that related to a different failure mode could be seen. Only small differences in the folding behaviour of the upper deck could be detected (cf. Fig. 36). This behaviour could have been caused by a too coarse mesh of the double-hull structures, since some small groups of elements were twisted in a different way or were missing in the models regarding friction. On the other hand, Peschmann [7] mentions that on a double-hull specimen tested during the joint research project *Life Cycle Design* (cf. Kulzep and Peschmann [32]), only small traces of friction were observedso that he used a dynamic friction coefficient of $\mu_k = 0.1$ in his calculations. This could mean that friction in total has only a minor influence in collision simulations.

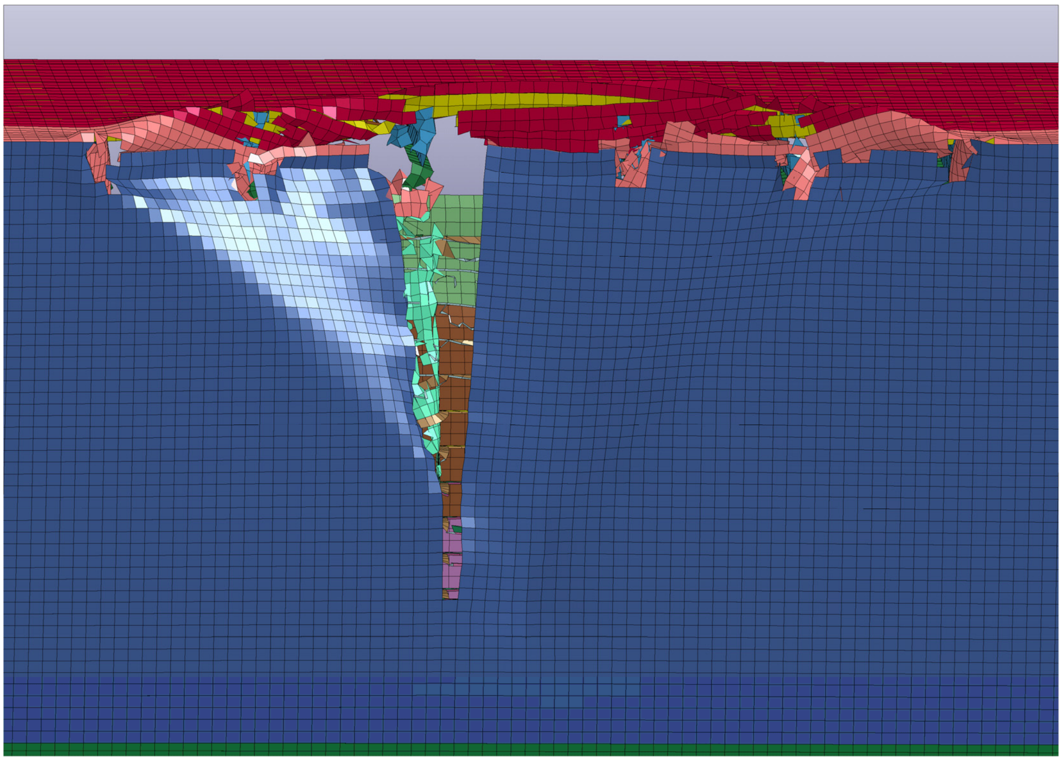

(a)

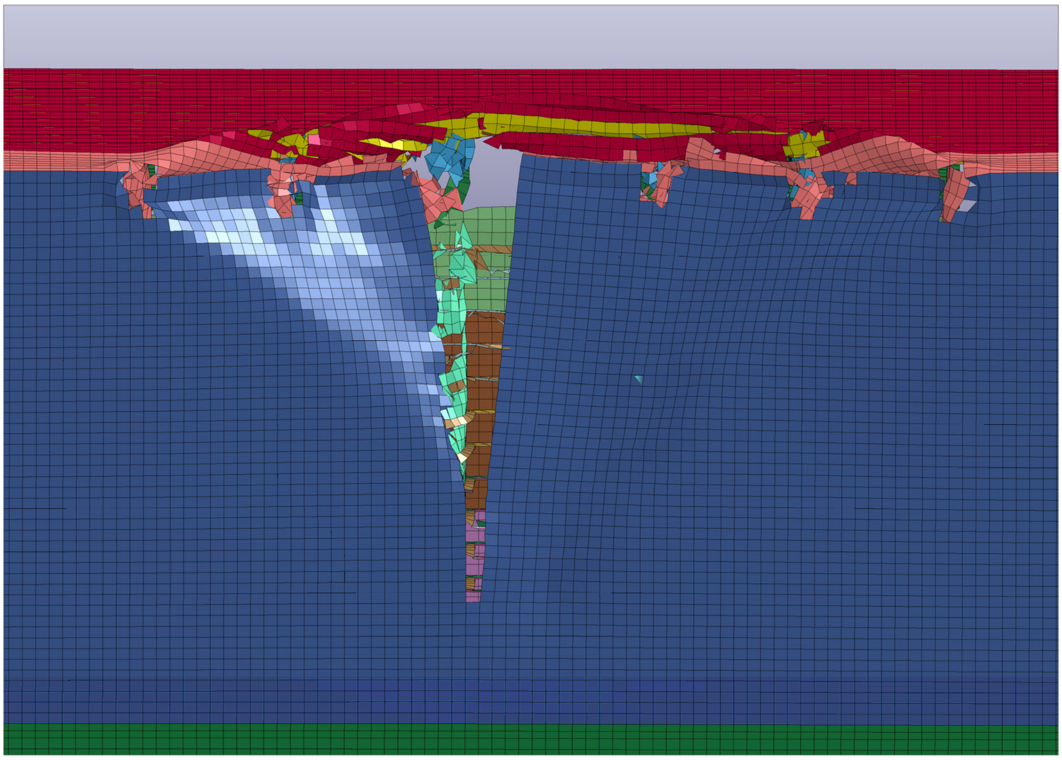

(b)

Fig. 36. Schematic comparison between calculations disregarding (a) and regarding (b) friction. The folding behaviour of the upper deck is somewhat different.

6.5. Collisions with defeatured structure

Table 2 shows a comparison between the results obtained from both the detailed and the defeatured conventional double-hull structure. The mean relative time requirement is the average ratio between the calculation times needed for a defeatured and detailed hull, and the mean relative error is the average relative error between absorbed energies, respectively. Typical calculation times for the detailed model were 460 min for GL, 485 min for PES, and 702 min for RTCL (average values, runaway values and the extended hull for RTCL are not taken into account). Individual values for every collision situation can be found in the Appendix, Tabs. 6 to 8. It can be seen that removing all sections in the model reduced the calculation times to 53% for PES and even below 50% for GL and RTCL. The largest average relative error occurred for GL. This can be explained with the relatively small amount of energy that was absorbed when using this approach, since even a small change in energy would result in a large deviation in percentage. Furthermore, it can be seen that the mean errors for PES and RTCL were approx. 12%, while the standard deviations decreased to only 0.6% for RTCL. It should be emphasised here that the mentioned savings in time resulted from deleting all sections, and, in the second case, additionally adjusting the geometry. However, the most considerable savings in time resulted from leaving out all small structural elements and corresponding adjustments of larger areas. The latter are necessary for ensuring a coherent mesh, as explained above (cf. Section 5.4). As can be seen from Table 3, the mean calculation times for the defeatured and revised hull decreased to approx. 7% and 6.5% for GL and RTCL, respectively, and 8.5% for PES, while the respective standard deviations were also very small. The mean relative errors in absorbed energy, on the other hand, increased to more than 30% for GL and RTCL and approx. 26% for PES. This means that the errors increased, although the structure itself was maintained and only small areas were merged to larger ones. The reason for this is that the mesh inherited from the large areas has a higher susceptibility to bending than the one inherited from the small areas. This implies that the failure modes are different. To overcome this issue, a more elaborate material model that accounts for this behaviour could be introduced. Additionally, the sections that were removed could be re-included by smearing them over the areas which originally contained them, i.e. by increasing thicknesses in these areas.

Table 2. Mean relative time requirement for and mean relative error of the defeatured hull compared to the detailed one, together with respective standard deviations (all in %).

	GL	PES	RTCL
$\bar{t}_{rel}$	40.5	52.9	34.7
$\sigma(\bar{t}_{rel})$	9.0	5.7	6.7
$\bar{e}$	23.4	11.7	11.9
$\sigma(\bar{e})$	5.1	4.1	0.6

Table 3. Mean relative time requirement for and mean relative error of the defeatured and revised hull compared to the detailed one, together with respective standard deviations (all in %).

	GL	PES	RTCL
$\bar{t}_{rel}$	7.1	8.5	6.5
$\sigma(\bar{t}_{rel})$	1.8	0.9	1.0
$\bar{e}$	30.17	25.91	32.69
$\sigma(\bar{e})$	5.9	5.2	8.0

6.6. Collisions with coarsened mesh

In Fig. 37, the mean required calculation time and the mean errors of the absorbed energies for the models with coarsened meshes compared to the fine mesh (l = 200 mm) are plotted. Both plots are normalised to the calculation time and absorbed energy of the fine mesh, respectively. Table 4 shows the corresponding standard deviations. It can be seen that as expected the necessary time decreased, while the imposed error increased with increasing mean element edge length. In Fig. 37a it is shown that the ratios for GL and PES lay very close to each other, while in comparison to these RTCL showed a ratio of approx. +10% at l = 300 mm and approx. +5% at l = 400 mm. Here it should be noticed that these deviations were caused by the large spread of calculations times for RTCL, which can be seen in Fig. 37a. Figure 37b shows the mean relative error between the absorbed energies of coarsened and fine hulls. It can be seen that PES caused the smallest errors while those generated by GL lay approx. +7% higher at l = 300 mm and approx. +10% higher at l = 400 mm. However, RTCL showed a runaway value at l = 300 mm (upper draught, impact between two web frames), which increased the mean relative error to approx. 42%. If this value was disregarded, the error would be approx. 27% as it is at l = 400 mm, which still is approx. +10% and approx. +17% compared to GL and PES, respectively. This deviating behaviour of RTCL can also be found in the standard deviations in Table 4: while GL and PES lay relatively close to each other RTCL differed considerably from these values.

Generally it can be said that PES yielded the least influence on the results due to a coarser mesh compared to the other two criteria. RTCL, on the other hand, yielded widespread results so that a distinct prediction of neither time nor error is possible.

Table 4. Standard deviations of the mean relative time requirement for and the mean relative error of the two coarser meshes of the narrow spaced x-core hull compared to the fine mesh (all in %).

		GL	**PES**	**RTCL**
l = 300 mm	$\sigma(\bar{t}_{rel})$	1.12	2.10	12.52
	$\sigma(\bar{e})$	21.55	12.30	61.47
l = 400 mm	$\sigma(\bar{t}_{rel})$	1.62	1.96	18.84
	$\sigma(\bar{e})$	6.85	3.54	17.88

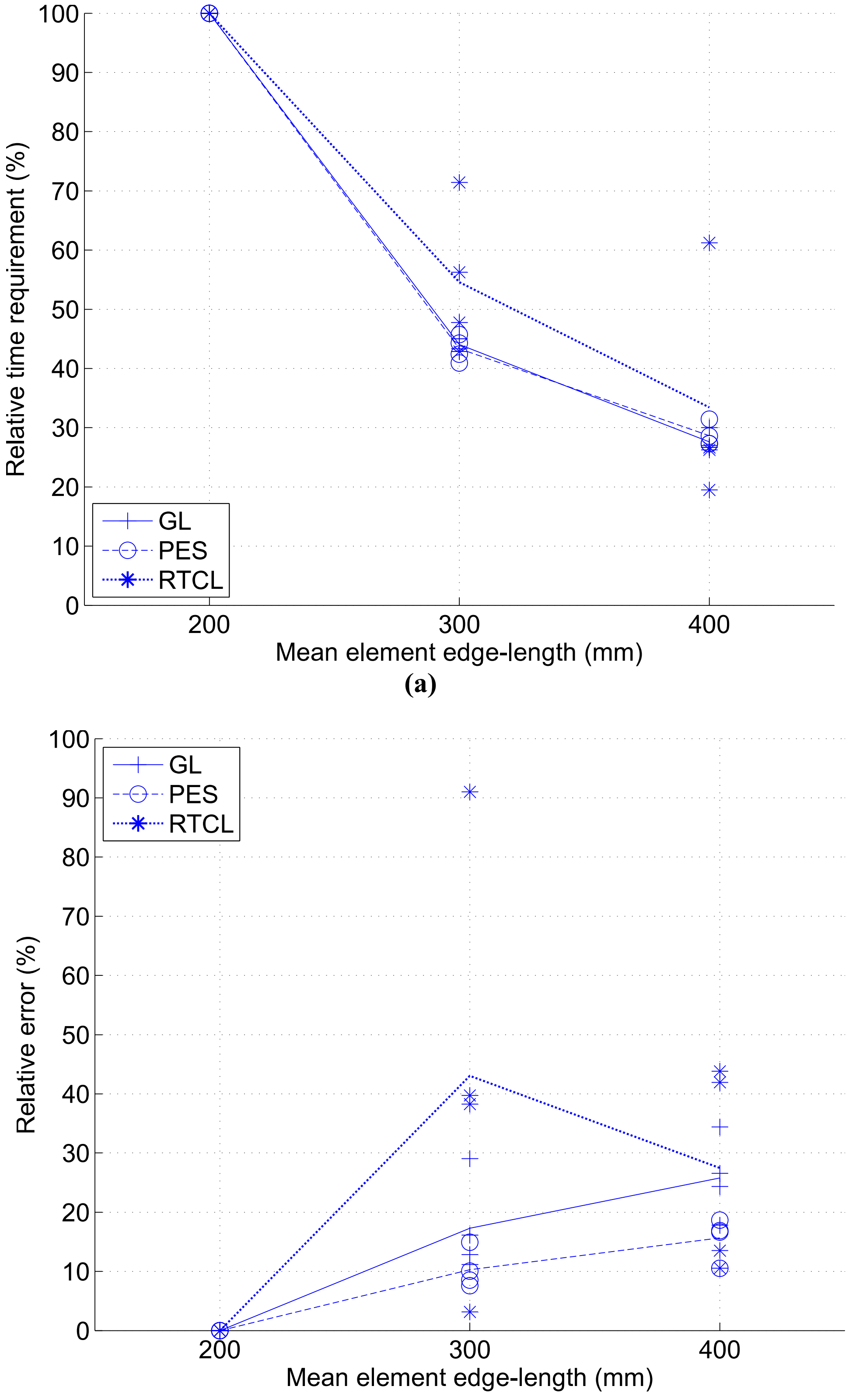

(a)

(b)

Fig. 37. Mean relative time requirement (a) for and mean relative error (b) of the two coarser meshes of the narrow spaced x-core hull compared to the fine mesh. The lines connect the mean values for the criteria at each mesh discretisation.

7. Conclusions

In this thesis, the collision behaviour of a RORO vessel's double-hull was investigated with regard to two different hull designs: a commonly used double-hull and the novel x-core structure. Additionally, the behaviour of both double-hulls regarding three different failure criteria was examined and compared: the GL-approach, the PES-criterion, and the RTCL-criterion. These investigations were carried out for different collision situations incorporating two different draughts and two different collision angles. Furthermore, the effects of a coarsened mesh and a defeatured model compared to the original models were investigated.

It was shown that for collisions perpendicular to the struck ship's side the double-hulls absorbed the lowest amount of energy for the GL-approach, followed by the PES-criterion, and the highest amount for the RTCL-criterion. The x-core structure showed a steeper slope in the absorbed energy-penetration depth curve than the conventional hull, even with a narrow hull spacing. This shows the potential for a higher crashworthiness of the x-core double-hull design. The PES-criterion responded well to changing sheet thicknesses, while the GL-approach and the RTCL-criterion showed no response and virtually no response, respectively. For the RTCL-criterion this was the case because the provided material model turned out to be inadequate concerning the criterion's calibration.

For collisions under an angle of 15° deviating from the hulls' normal higher amounts of absorbed energy than for the collision perpendicular to the hulls were obtained. This was due to the longer distance that had to be covered by the striking bow before fracture occurred and the larger area of the bow that crashed. These results were contrary to predictions deduced from Minorsky's method, which stated that the absorbed energy under an angle should have been smaller. However, this can be expected to be the case at larger deviating angles, since the striking bow will be likely to slide against and bounce off the struck hull.

The differences between the results of collisions regarding and disregarding friction were investigated. It was found that except for small differences in the folding behaviour of the upper deck structure no distinct variation in absorbed energy or failure mode could be detected.

Since the modelling of the conventional double-hull took a large amount of time, both the savings in time and the introduced errors were investigated to see if the model was defeatured. For this, in a first step all sections were removed from the model, and in a second step the model was revised to obtain larger areas and further decrease the necessary calculation time. It was found that for the defeatured model the PES and RTCL-criteria provided a mean relative error of approx. 12% in on average half the original calculation time, while the error for the GL-approach was twice as large. For the revised model the necessary calculation times were reduced to approx. 7-8% of the original times, while the mean relative errors increased to approx. 26% for the PES-criterion and approx. 30% for the RTCL-criterion and the GL-approach. This was because the large areas of the revised hull reacted to the impact with a different failure mode than the original and defeatured ones.

To decrease the necessary calculation time for the x-core double-hull the differences between the original mesh-density and two additional discretisations of the mesh were examined: mean element edge length $l = 200$ mm (original), $l = 300$ mm, and $l = 400$ mm. It was found that the calculation time decreased notably for both criteria and the GL-approach. However, the RTCL-criterion showed widespread results at both coarser meshes. With respect to the introduced errors the PES-criterion showed the smallest deviations, while the GL-approach caused somewhat larger errors. The RTCL-criterion, on the other hand, showed a runaway value that caused a very high degree of error while otherwise the results were similar to the GL-approach.

Based on these findings several recommendations on how to carry out collision simulations at FSG in the future can be deduced:

- The GL-approach is specified as mandatory in the GL-regulations. It should therefore be used when the classification society's requirements have to be fulfilled, for example in a statistical distribution of collision situations (cf. Chapter 8). However, from the current point of view the PES-criterion should be used as a failure criterion if a more realistic estimation is desired. It responds well to changing input parameters such as sheet thickness and causes the lowest errors if the model is simplified. Additionally, the errors that are caused for the models with a coarsened mesh stay fairly constant over the range investigated. This means that they could be taken into account globally in future simulations, if further benchmarks were to confirm this behaviour.

- The calibration of the RTCL-criterion should be repeated with a more suitable material model (cf. Chapter 8). This could increase the usefulness of this promising criterion considerably and reduce the mentioned widespread results. Here it should be noted that LS-DYNA has the limitation of not being able to model damage initiation correctly, which in the case of GL is currently overcome by employing a very low failure strain. Hence, this approach would not improve results until a version of LS-DYNA supporting damage initiation is released.

- In the present investigation Minorsky's method wrongly predicted the energy ratio between perpendicular and angular impacts and thus yields results too inaccurate to be used.

- The introduction of friction caused only minor differences in the results. However, since the usage of friction does not influence the necessary modelling or calculation time it should be included. In this way effects that were not discovered in this investigation could be revealed.

- The defeatured and revised hull saves a large amount of modelling and calculation time. Therefore, this approach should be pursued by smearing the removed sections and incorporating a more elaborate material law that can account for the behaviour of large areas (cf. Chapter 8).

- The minimum hull spacing that the x-core double-hull design can assume always depends on the collision situation.

- In the current investigation the bulb cut through the hull. The stem, on the other hand, crushed it and thereby introduced the largest fraction of the total kinetic energy. Thus, the hulls could profit from a reinforced upper module. However, since in reality the stem acts as a crush-zone and deforms easily while the bulb is very stiff, the lower part of the hull may not be left unconsidered.

8. Future work

In this investigation several limitations were imposed on the models to allow for sufficiently short calculation times so that a greater number of collision situations could be simulated (cf. Section 1.4). Therefore, it would be interesting to examine the collision behaviour of both hull designs considering the following points:

- The examined failure criteria not only impose a varying ability to deform plastically on the material, but their underlying theories are also able predict different failure modes (for example due to consideration of element length and triaxiality). Therefore, it would be very important to exactly define what kinds of results are expected from future simulations.

- External dynamics could be included. These would be hydrodynamic masses of both vessels which would yield additional inertia effects, sway and yaw of the struck vessel, and a velocity of the struck vessel $v \neq 0$. Additionally, a deformable striking bow could be used since it could cause larger damage than the rigid one at certain draughts and collision angles.

- Ballast tanks and manholes for inspections could be included in future simulations. Other possibilities could be to introduce openings in places where two x-cores meet at a frame wall and use these as ballast tanks, or use two x-core hulls as a double structure with an open space in between.

- The x-core structure could be checked for a satisfactory transfer of forces and momentums and modified if required. Together with the third point, also a meaningful comparison between the weights of the conventional and x-core structures could then be made.

- Welding seams of the laser-welded x-core structure could be taken into account.

- The calculations could be redone with a material model which is more suitable for calibration of the RTCL-criterion, i.e. accounts for damage initiation and degradation, when this is possible in LS-DYNA. It could be obtained from practical tests which are planned to soon be carried out at TUHH. Additionally, this model should then also be able to account for the altered behaviour of the revised double-hull.

- The sections that were removed in the defeatured and revised model could be smeared over the respective areas which contained them. This way the areas' thicknesses would be increased and the absorbed energy would approach the original value again. Here it could be investigated if the necessary percentage to equal out the missing volume is constant.

- More angles and velocities of the striking ship could be simulated to obtain a statistical distribution which could be used for calculations complying with SOLAS 2009.

9. References

[1] A.W. Vredeveldt. ‘Crashworthiness as a means to improve damage stability survivability’. In: *Second International Conference on Collision and Grounding of Ships* (ICCGS). Copenhagen, Denmark, 1st–3rd July, 2001.

[2] E. V. Lewis. *Principles of Naval Architecture. Volume I - Stability and Strength*. Second Revision. Society of Naval Architects and Marine Engineers, 1988.

[3] E. Lehmann and J. Peschmann. ‘Energy absorption by the steel structure of ships in the event of collisions’. In: *Marine Structures* 15(4-5), 2002, pp. 429–441.

[4] Maritime Safety Committee. *Interim explanatory notes to the SOLAS chapter II-1 subdivision and damage stability regulations. Resolution MSC.1/Circ.1226*. International Maritime Organization. 2007.

[5] P. Hogström. ‘Holistic Assessment of Survival Time after Ship Collision’. Department of Shipping and Marine Technology, Chalmers University of Technology, 2010.

[6] Deltamarin Ltd. *Research Project 552. Impact Assessment On The Design of New Cruise Liners, Ro-Ro Passenger Ships And Cargo Vessels Of The Forthcoming Revision To SOLAS Ch II-1, Part A, B & B-1 Relating To Subdivision And Probabilistic Damage Stability*. CONTAINER FEEDER. 2011.

[7] J. Peschmann. ‘Berechnung der Energieabsorption der Stahlstruktur von Schiffen bei Kollision und Grundberührung’. German. PhD thesis. Institute for Ship Structural Design and Analysis, Hamburg University of Technology, 2001.

[8] Y. Cao, J. Ahlström and B. Karlsson. ‘Mechanical Behaviour of a Rephosphorized Steel for Car Body Applications: Effects of Temperature, Strain Rate, and Pretreatment’. In: *Journal of Engineering Materials and Technology* 133(2), 2011, pp. 021019-1–021019-11

[9] M. Selin. ‘Comparing Three Equations Used for Modelling the Tensile Flow Behavior of Compacted Graphite Cast Irons at Elevated Temperatures’. In: *Metallurgical and materials transactions. A, Physical metallurgy and materials science* 41(11), 2010, pp. 2805–2815.

[10] N. Peixinho and A. Pinho. ‘Study of Viscoplasticity Models for the Impact Behavior of High-Strength Steels’. In: *Journal of Computational and Nonlinear Dynamics* 2(2), 2007, pp. 114–123.

[11] V. U. Minorsky. ‘An analysis of ship collisions with reference to protection of nuclear power plants’. In: *Journal of Ship Research* (1959).

[12] A. J. Brown. SSC – 1400 *Draft Report. Modelling Structural Damage in Ship Collisions*. Ship Structure Committee, 2002.

[13] R. Tørnqvist. ‘Design of Crashworthy Ship Structures’. PhD thesis. Technical University of Denmark, Department of Mechanical Engineering, Maritime Engineering, 2003.

[14] Y. Bao. ‘Dependence of ductile crack formation in tensile tests on stress triaxiality, stress and strain ratios’. In: *Engineering Fracture Mechanics* 72, 2005, pp. 505–522.

[15] Germanischer Lloyd. *Strengthening against Collisions*. Part 1 - Seagoing Ships, Chapter 1 - Hull Structures, Section 33. 2010.

[16] N. E. Dowling. *Mechanical Behaviour of Materials. Engineering Methods for Deformation, Fracture, and Fatigue*. Third edition. Prentice Hall, 2007.

[17] I. Tautz. ‘Untersuchung konstruktiver Maßnahmen zur Verbesserung der Sicherheit von Doppelhüllentankern’. German. Institute for Ship Structural Design and Analysis, Hamburg University of Technology, 2006.

[18] H. Kuhn and D. Medlin, eds. *ASM Handbook. Volume 08 – Mechanical Testing and Evaluation*. ASM International, 2000.

[19] P. Hogström, J. W. Ringsberg and E. Johnson. ‘An experimental and numerical study of the effects of length scale and strain state on the necking and fracture behaviours in sheet metals’. In: *International Journal of Impact Engineering* 36(10-11), 2009, pp. 1194–1203.

[20] S. Ehlers. ‘The influence of the material relation on the accuracy of collision simulations’. In: *Marine Structures* 23, 2010, pp. 462–474.

[21] H. S. Alsos, J. Amdahl and O. S. Hopperstad. ‘On the resistance to penetration of stiffened plates’. Part II: Numerical analysis. In: *International Journal of Impact Engineering* 36, 2009, pp. 875–887.

[22] H. S. Alsos and J. Amdahl. ‘On the resistance of tanker bottom structures during stranding’. In: *Marine Structures* 20, 2007, pp. 218–237.

[23] J. Urban. ‘Crushing and Fracture of Lightweight Structures’. PhD thesis. Technical University of Denmark, Department of Mechanical Engineering, Maritime Engineering, 2003.

[24] S. Ehlers, J. Broekhuijsen, H. S. Alsos, F. Biehl and K. Tabri. ‘Simulating the collision response of ship side structures: A failure criteria benchmark study’. In: *International Shipbuilding Progress* 55, 2008, pp. 127–144.

[25] B. C. Simonsen and R. Tørnqvist. ‘Experimental and numerical modelling of ductile crack propagation in large-scale shell structures’. In: *Marine Structures* 17, 2004, pp. 1–27.

[26] Livermore Software Technology Corporation. *LS-DYNA Theory Manual*. 2006.

[27] A. Klanac, S. Ehlers and K. Tabri. ‘Qualitative design assessment of crashworthy structures’. In: *Proceedings of the 12th International Congress of the International Maritime Association of the Mediterranean. Maritime Transportation and Exploitation of Ocean and Coastal Resources*. 2005, pp. 461–469.

[28] U. B. Karlsson. ‘Improved Collision Safety of Ships by an Intrusion-Tolerant Inner Side Shell’. In: *Marine Technology* 46(3), 2009, pp. 165–173.

[29] S. Ehlers, K. Tabri, J. Romanoff and P. Varsta. ‘Numerical and Experimental Investigation on the Collision Resistance of the X-core Structure’. In: *Proceedings of 5th International Conference on Collision and Grounding of Ships*. 2010, pp. 18–24.

[30] Livermore Software Technology Corporation. *Time integration – LS-DYNA Support*. 2011. URL: http://www.dynasupport.com/tutorial/ls-dyna-users-guide/time-integration (visited on 21/03/2011).

[31] P. T. Pedersen and S. Zhang. ‘Absorbed Energy in Ship Collisions and Grounding – Revising Minorsky’s Empirical Method’. In: *Journal of Ship Research* 44(2), 2000, pp. 140–154.

[32] A. Kulzep and J. Peschmann. *Seitenkollision von Doppelhüllenschiffen. Abschlußbericht zum BMBF Verbundforschungsvorhaben Life Cycle Design*. Teil D2A. German. Hamburg University of Technology, 1999.

[33] Wikimedia Foundation Inc. *Divergence*. 2011. URL: http://en.wikipedia.org/wiki/Divergence (visited on 28/03/2011).

APPENDIX

Explicit time integration

The fundamental equation which an explicit solver tries to find a solution for is the equation of motion. In the case of a finite element mesh it constitutes a system of either linear (Eq. (26)) or nonlinear (Eq. (27)) ordinary differential equations (cf. LSTC [26]):

$$[M]\ddot{U} + [C]\dot{U} + [K]U = P(t) \tag{26}$$

$$[M]\ddot{U} + [C]\dot{U} + f(U) = P(t) \tag{27}$$

where [*M*], [*C*], and [*K*] are the matrices for mass, dampings and stiffness, respectively, and the vector *P*(*t*) includes external forces. Contrary to an implicit method where the velocity-dependent and acceleration-dependent terms are zero and a static equilibrium is searched, these terms have to be taken into account in a dynamic problem. Furthermore, while the linear type of the equation of motion can be solved analytically by determining the dynamic response due to a harmonic load, the non-linear type can only be solved numerically. In LS-DYNA this is done with the *central difference method* which uses *central difference time integration* to find the displacement increment from Eq. (29) (cf. LSTC [26]).

The central difference method replaces the continuous differential equations with discrete difference equations which are approximately equal to the former (cf. Fig. 2). The system of equations of motion at equilibrium at time *n* is:

$$[M]\ddot{u}_n + [C]\dot{u}_n + [K]u_n = P_n \tag{28}$$

where P_n is the load vector at time *n* (cf. LSTC [30]). The velocity-vector at time *n* can be expressed as:

$$\dot{u}_n = \frac{u_{n+1} - u_{n-1}}{2\Delta t} \tag{29}$$

while the corresponding acceleration at time *n* can be expressed as:

$$\begin{aligned} \dot{u}_n &= \frac{\dot{u}_{n+1/2} - \dot{u}_{n-1/2}}{2\Delta t} \\ &= \frac{1}{\Delta t}\left(\frac{u_{n+1} - u_n}{2\Delta t} - \frac{u_n - u_{n-1}}{2\Delta t}\right) \\ &= \frac{u_{n+1} - 2u_n + u_{n-1}}{2\Delta t^2} \end{aligned} \tag{30}$$

Equations (29) and (30) are then inserted into Eq. (28) and after reforming this yields:

$$\left([M]+[c]\frac{\Delta t}{2}\right)u_{n+1} = P_n\Delta t^2 - \left([K]\Delta t^2 - 2[M]\right)u_n - \left([M]-[C]\frac{\Delta t}{2}\right)u_{n-1} \tag{31}$$

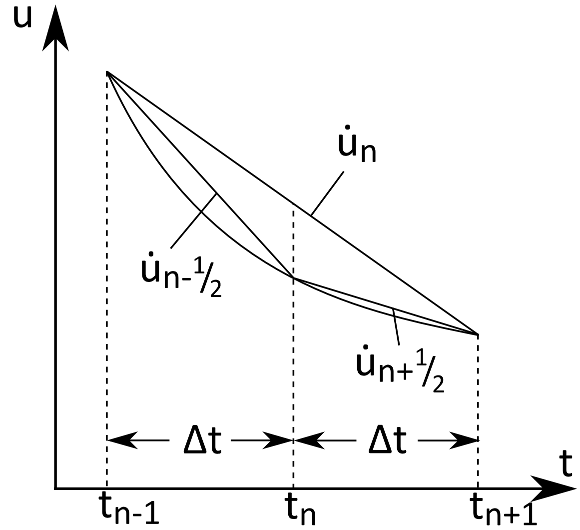

Fig. 38. Discretisation in the central difference method (after LSTC [26]).

Finally, the new displacement-vector u_{n+1} can be obtained from Eq. (31) and the total displacement can be updated:

$$u = u_n + u_{n+1} \tag{32}$$

As is mentioned by LSTC [30], LS-DYNA applies this method in a slightly modified way. Instead of displacements u the actual geometry x is used. In the case of non-linear equations this yields:

$$[M]\ddot{x}_n + [C]\dot{x}_n + F_n^{\text{int}} = P_n \tag{33}$$

where F_n^{int} is the stress divergence vector. Stresses are available as a vector field and the divergence operator assigns scalar values representing a measure of the magnitude to this field (cf. Wikimedia [33]). From the central difference method velocity and acceleration are obtained as:

$$\dot{x}_{n+1/2} = \frac{x_{n+1} - x_n}{\Delta t_{n+1/2}} \tag{34}$$

$$\ddot{x}_n = \frac{\dot{x}_{n+1/2} - \dot{x}_{n-1/2}}{\Delta t_n} \tag{35}$$

where it should be noted that $\ddot{x}_n$ is a central difference while $\dot{x}_{n+1/2}$ is not. Eqs (34) and (35) can be combined to:

$$x_{n+1} = x_n + (\dot{x}_{n-\frac{1}{2}} + \ddot{x}_n \Delta t_n)\Delta t_n \tag{36}$$

Then the missing acceleration can be obtained from Eq. (33). Here it is assumed that for the update of the accelerations $\dot{x}_n = \dot{x}_{n-\frac{1}{2}}$ so that:

$$\ddot{x}_n = [M]^{-1}\left(P_n - F_n^{\text{int}} - [C]\dot{x}_{n-\frac{1}{2}} \right) \tag{37}$$

In total, the updated geometry at time *n+1* finally can be computed as:

$$x_{n+1} = x_n + \left(\dot{x}_{n-\frac{1}{2}} + [M]^{-1}\left(P_n - F_n^{\text{int}} - [C]\dot{x}_{n-\frac{1}{2}} \right)\Delta t_n \right)\Delta t_n \tag{38}$$

To ensure numerical stability, the smallest time step must be shorter than the period a sound wave needs to propagate through an element. For a shell element this critical time-step size is determined through Eq. (39) where l_s is the characteristic element length of the smallest element. It is defined as Eq. (40) with β being equal to zero for triangular and one for quadrilateral elements (cf. LSTC [26]).

$$\Delta t_{crit} = \frac{l_s}{c} \tag{39}$$

$$l_s = \frac{(1+\beta)A_s}{\max(l_1, l_2, l_3, (1-\beta)l_4)} \tag{40}$$

Thus, the characteristic length is calculated by dividing the surface area of the smallest element in the model by the length of its longest edge. c is the plane stress propagation velocity of sound through the material and is defined as Eq. (41):

$$c = \sqrt{\frac{E}{\rho(1-\nu)}} \tag{41}$$

with Young's modulus *E*, density ρ, and Poisson's ratio ν. As a general conclusion this means the larger and lighter the elements in a model are the larger the time step can be chosen without the risk of instabilities and convergence errors.

Dimensions of replacement sections

Table 5. Dimensions of L-sections to replace corresponding HP-sections (in mm, cf. Fig. 20) and relative errors of inertia and cross-sections (in %).

HP	h_{web}	t_{web}	w_{flange}	t_{flange}	e_{Jyy}	e_A
300 × 11	270.0	11.0	56.0	30.0	0.01	0.19
280 × 11	255.0	10.0	57.0	25.0	0.02	0.26
260 × 10	241.5	10.0	62.0	18.5	0.11	0.35
240 × 10	219.0	10.0	49.0	21.0	0.08	0.16
220 × 9	200.5	9.0	44.0	19.5	0.10	0.15
200 × 9	180.0	9.0	43.0	20.0	< 0.01	< 0.01
180 × 8	165.0	8.0	37.0	15.0	0.11	0.10
160 × 7	139.5	7.0	25.0	20.5	0.02	< 0.01
140 × 8	124.5	8.0	25.0	15.5	< 0.01	< 0.01

Results from collisions perpendicular to the ship's side

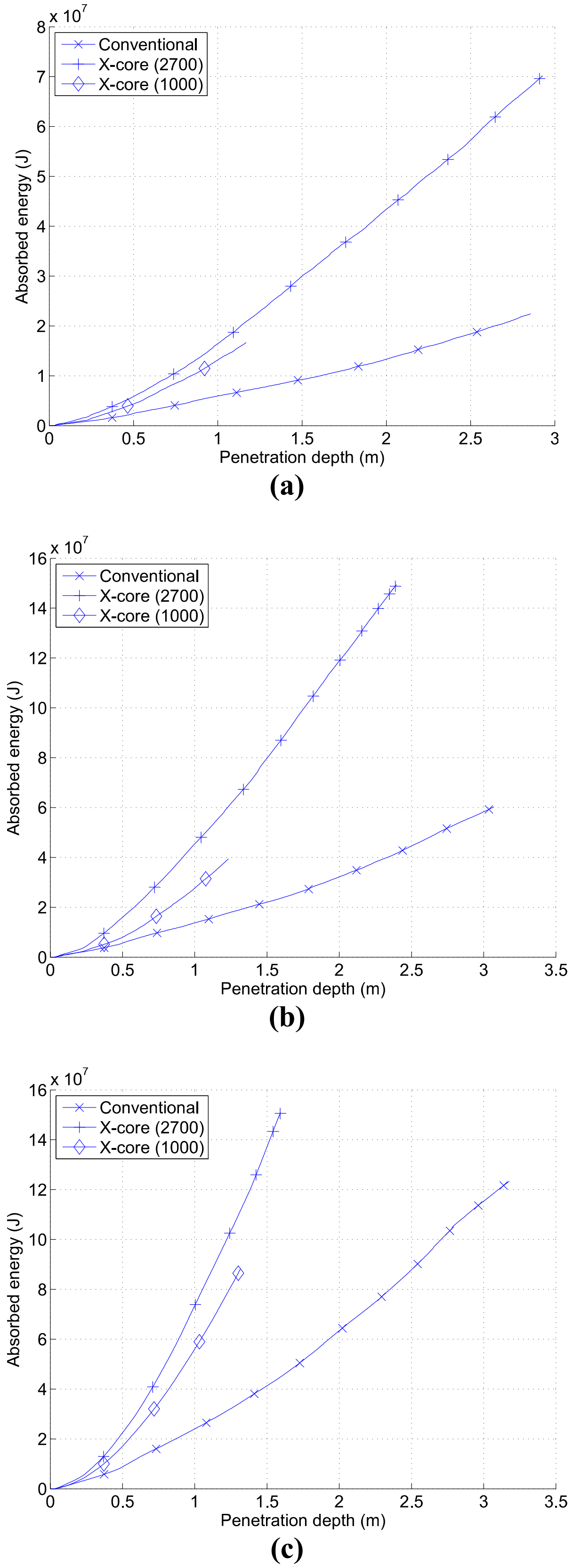

Fig. 39. Lower draught, impact on a web frame: total energies absorbed by conventional and x-core designs for the GL- (a), PES- (b), and RTCL-criteria (c).

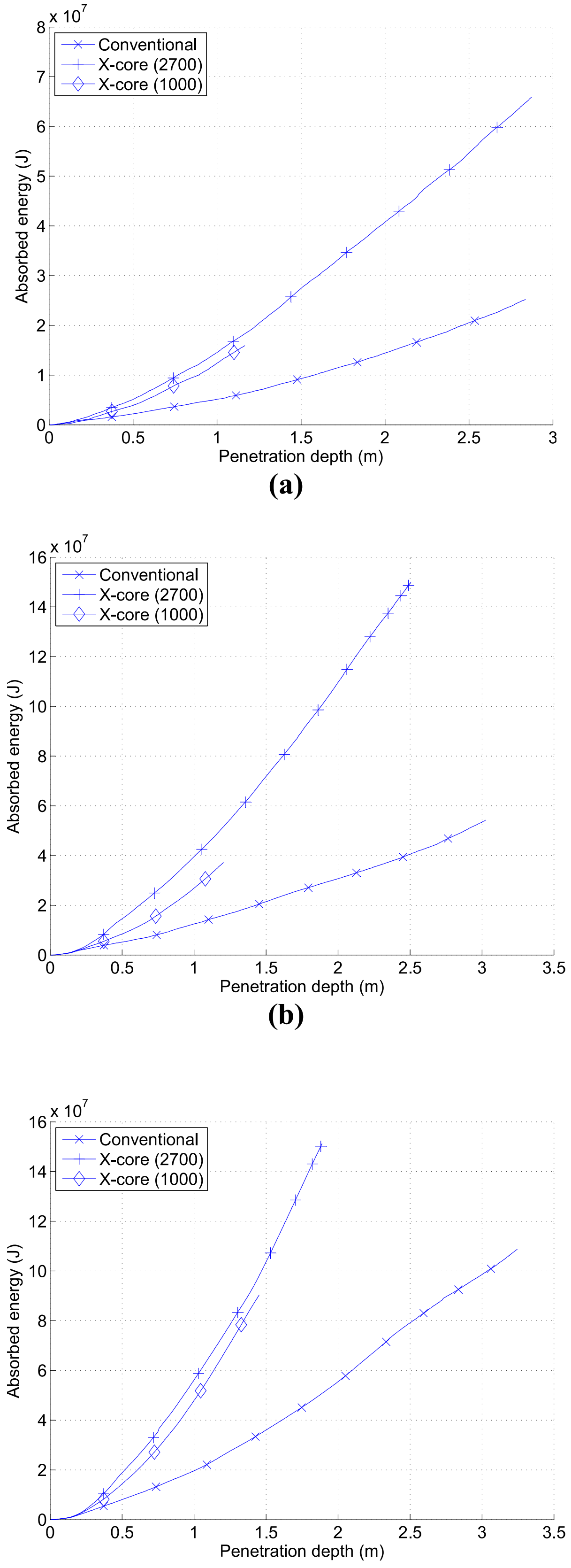

Fig. 40. Lower draught, impact between two web frames: total energies absorbed by conventional and x-core designs for the GL- (a), PES- (b), and RTCL-criteria (c).

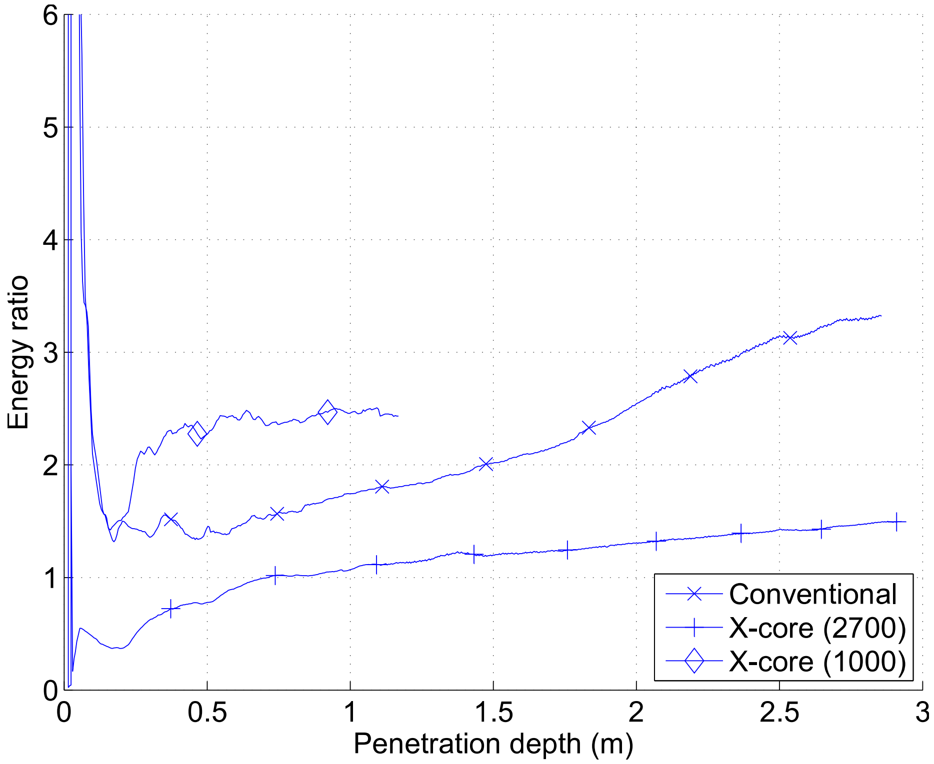

(a)

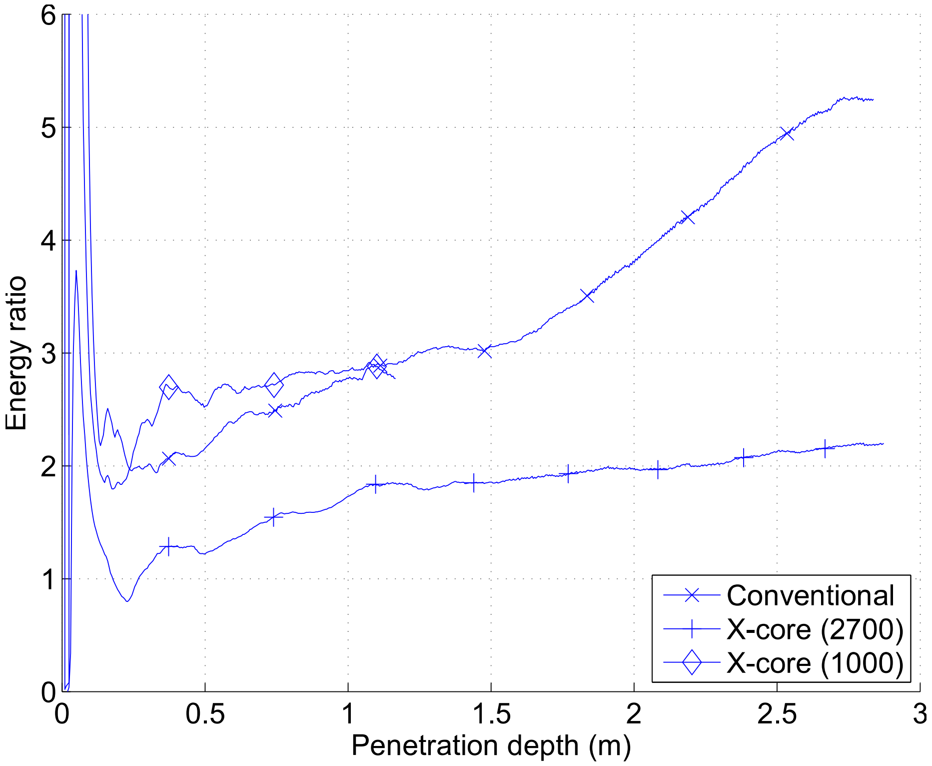

(b)

Fig. 41. Lower draught, GL-criterion: ratios between energies absorbed by stem and bulb for an impact on a web frame (a) and between two web frames (b).

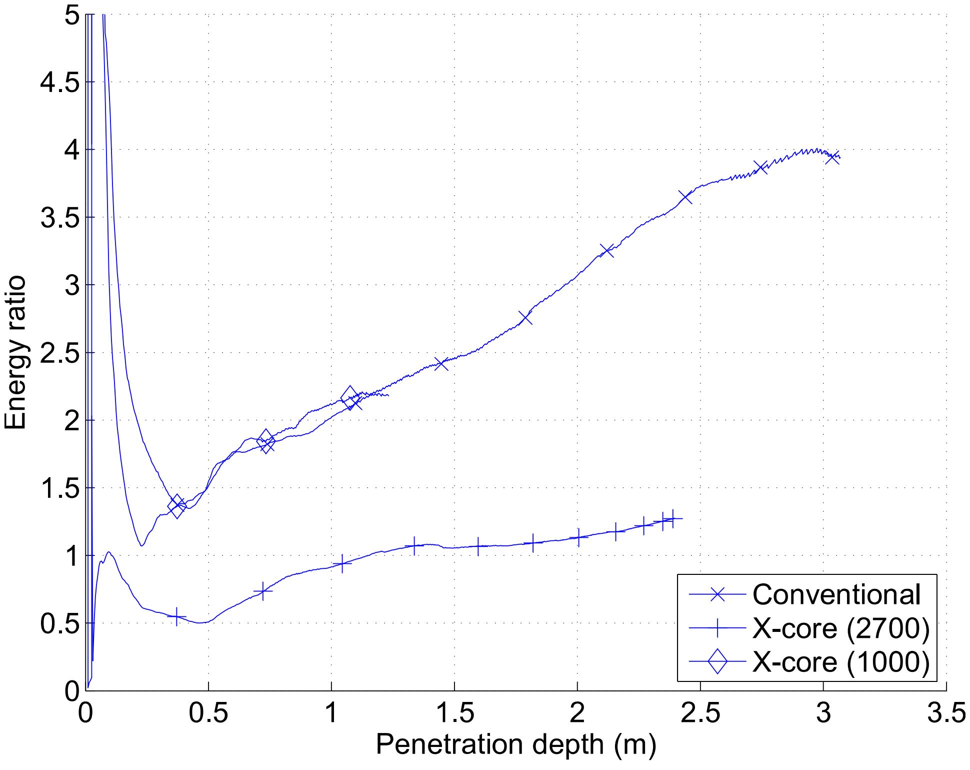

(a)

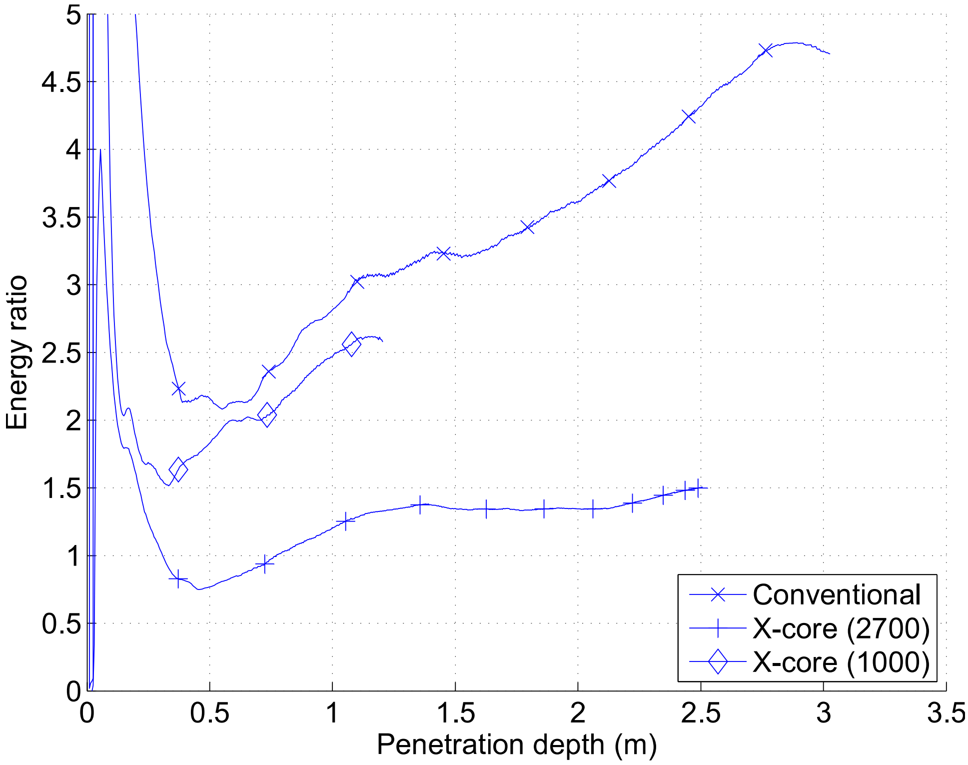

(b)

Fig. 42. Lower draught, PES-criterion: ratios between energies absorbed by stem and bulb for an impact on a web frame (a) and between two web frames (b).

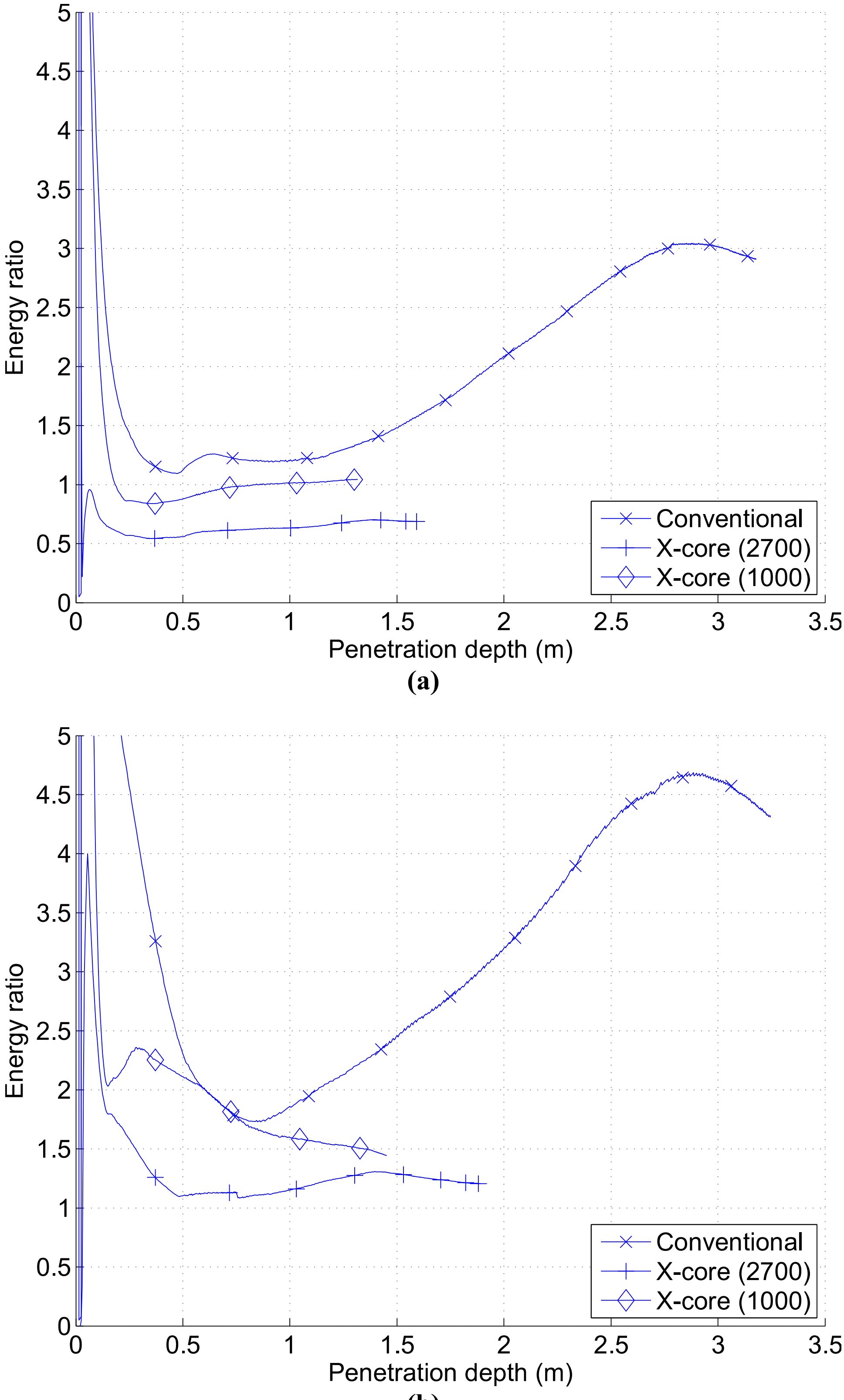

(a)

(b)

Fig. 43. Lower draught, RTCL-criterion: ratios between energies absorbed by stem and bulb for an impact on a web frame (a) and between two web frames (b).

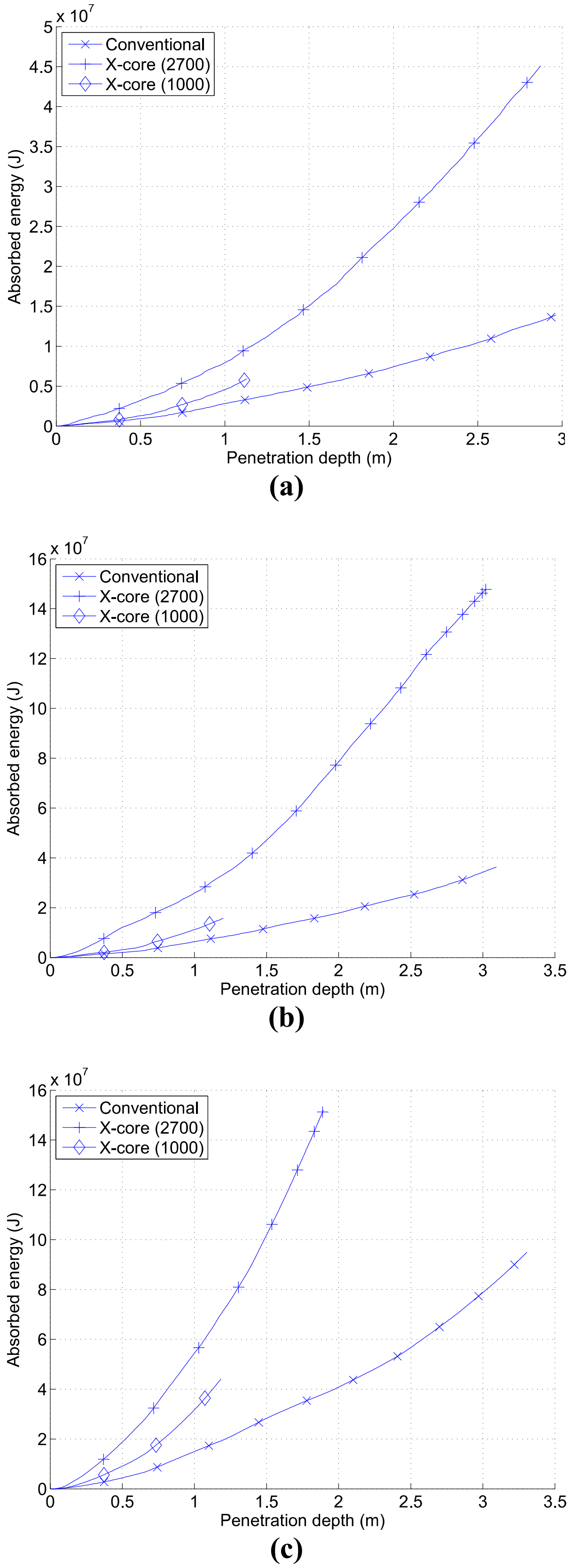

Fig. 44. Upper draught, impact on a web frame: total energies absorbed by conventional and x-core designs for the GL- (a), PES- (b), and RTCL-criteria (c).

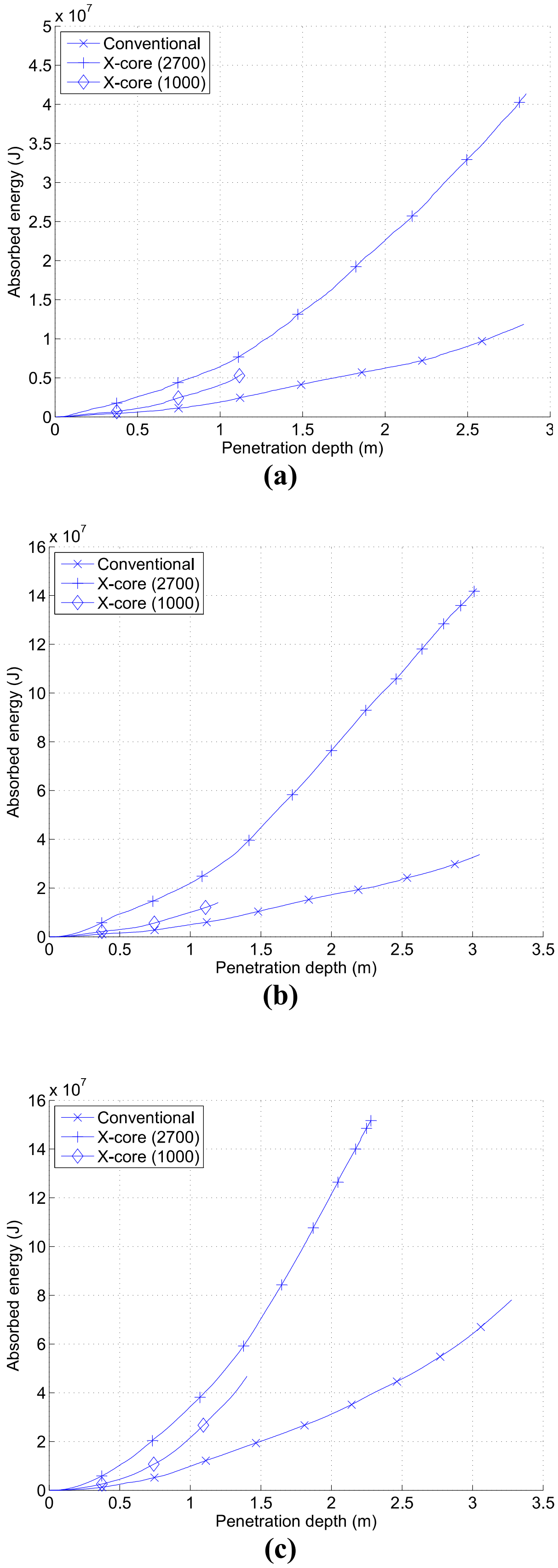

Fig. 45. Upper draught, impact between two web frames: total energies absorbed by conventional and x-core designs for the GL- (a), PES- (b), and RTCL-criteria (c).

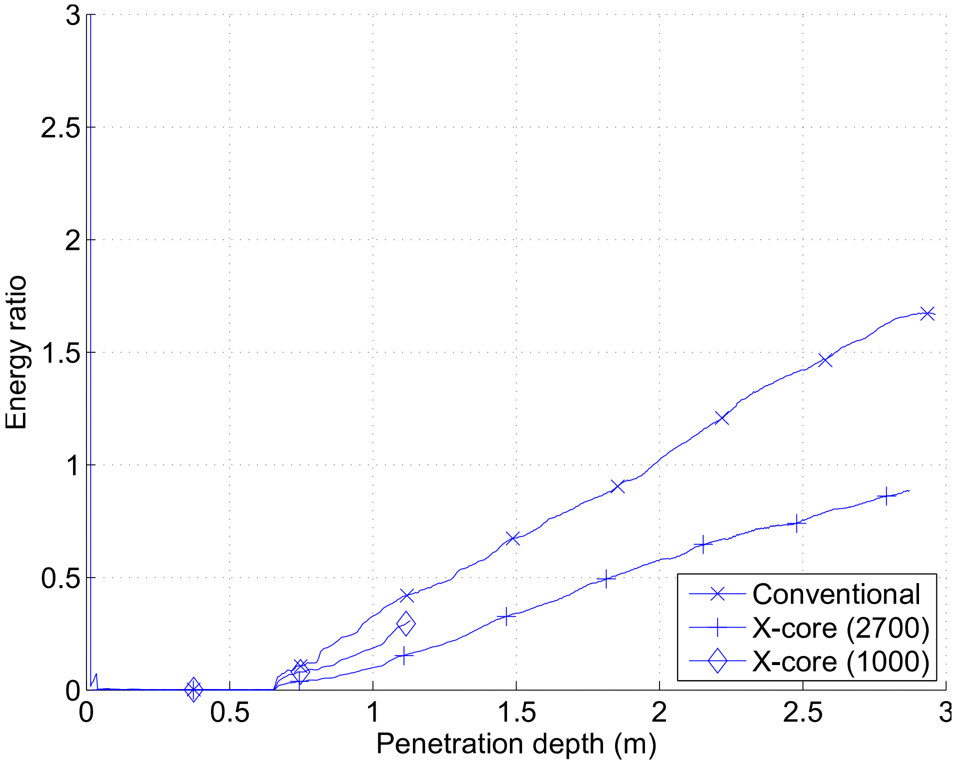

(a)

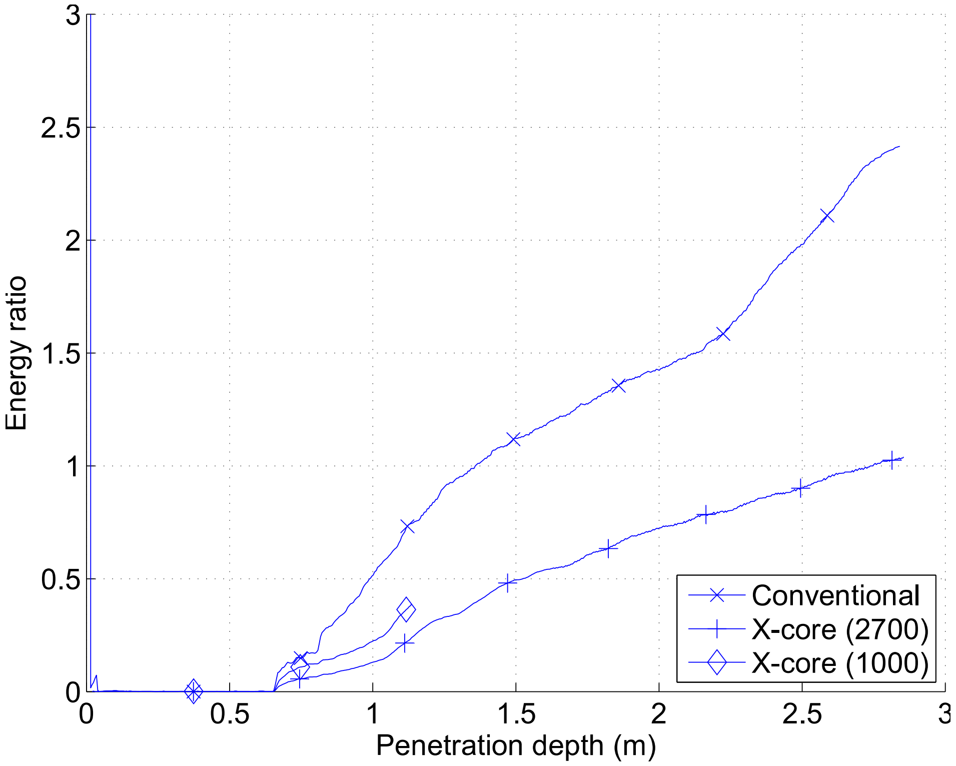

(b)

Fig. 46. Upper draught, GL-criterion: ratios between energies absorbed by stem and bulb for an impact on a web frame (a) and between two web frames (b).

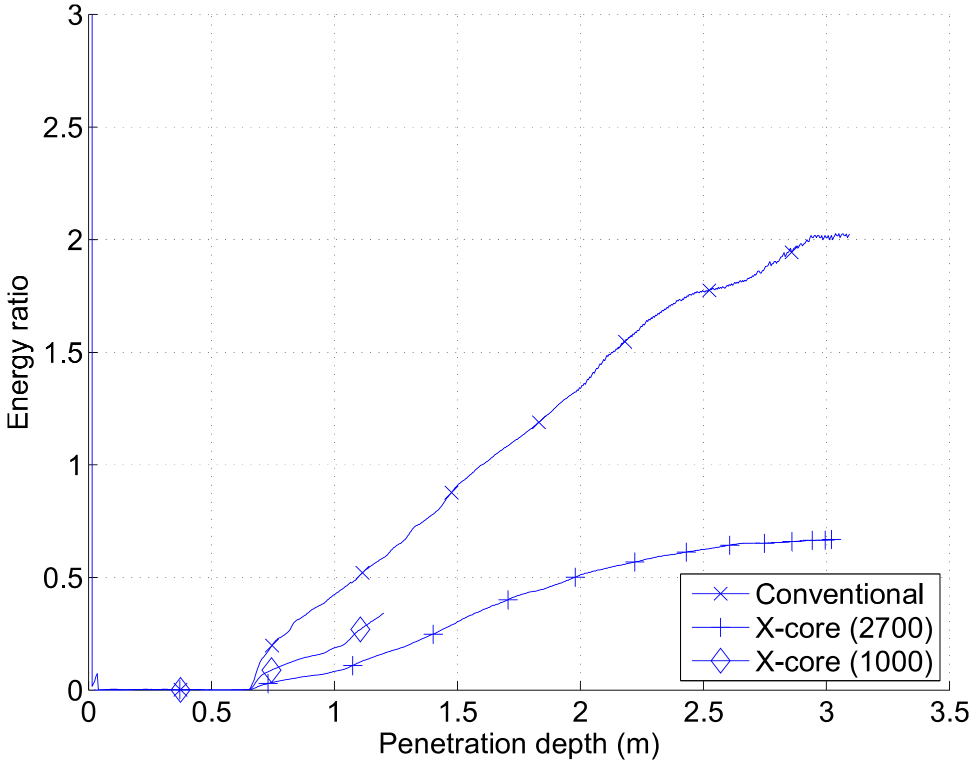

(a)

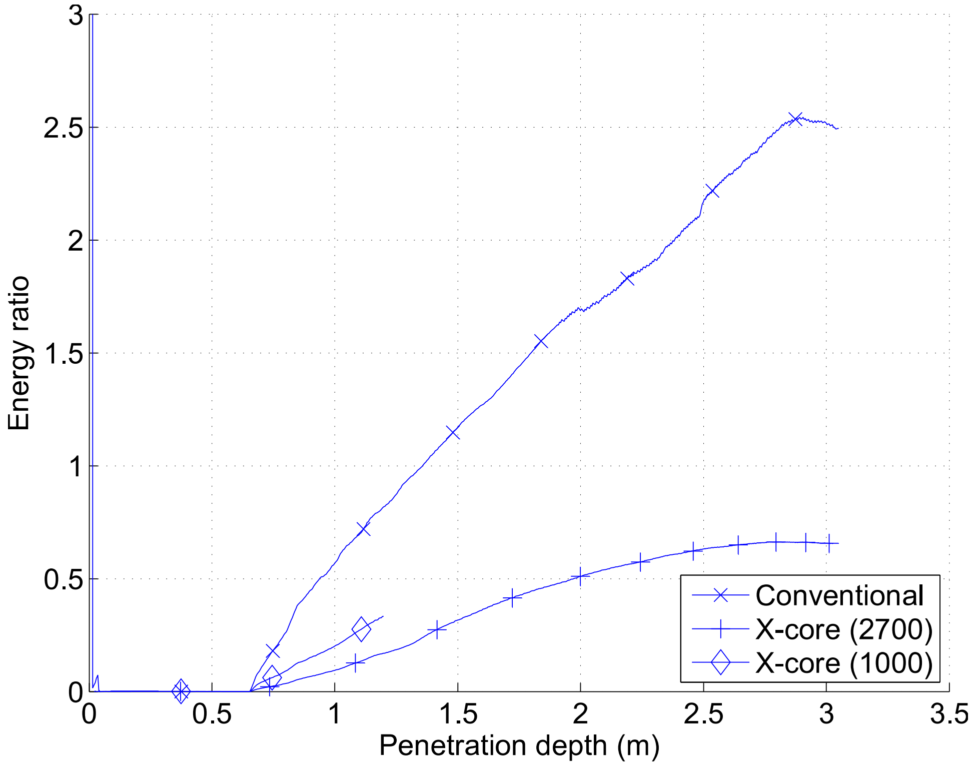

(b)

Fig. 47. Upper draught, PES-criterion: ratios between energies absorbed by stem and bulb for an impact on a web frame (a) and between two web frames (b).

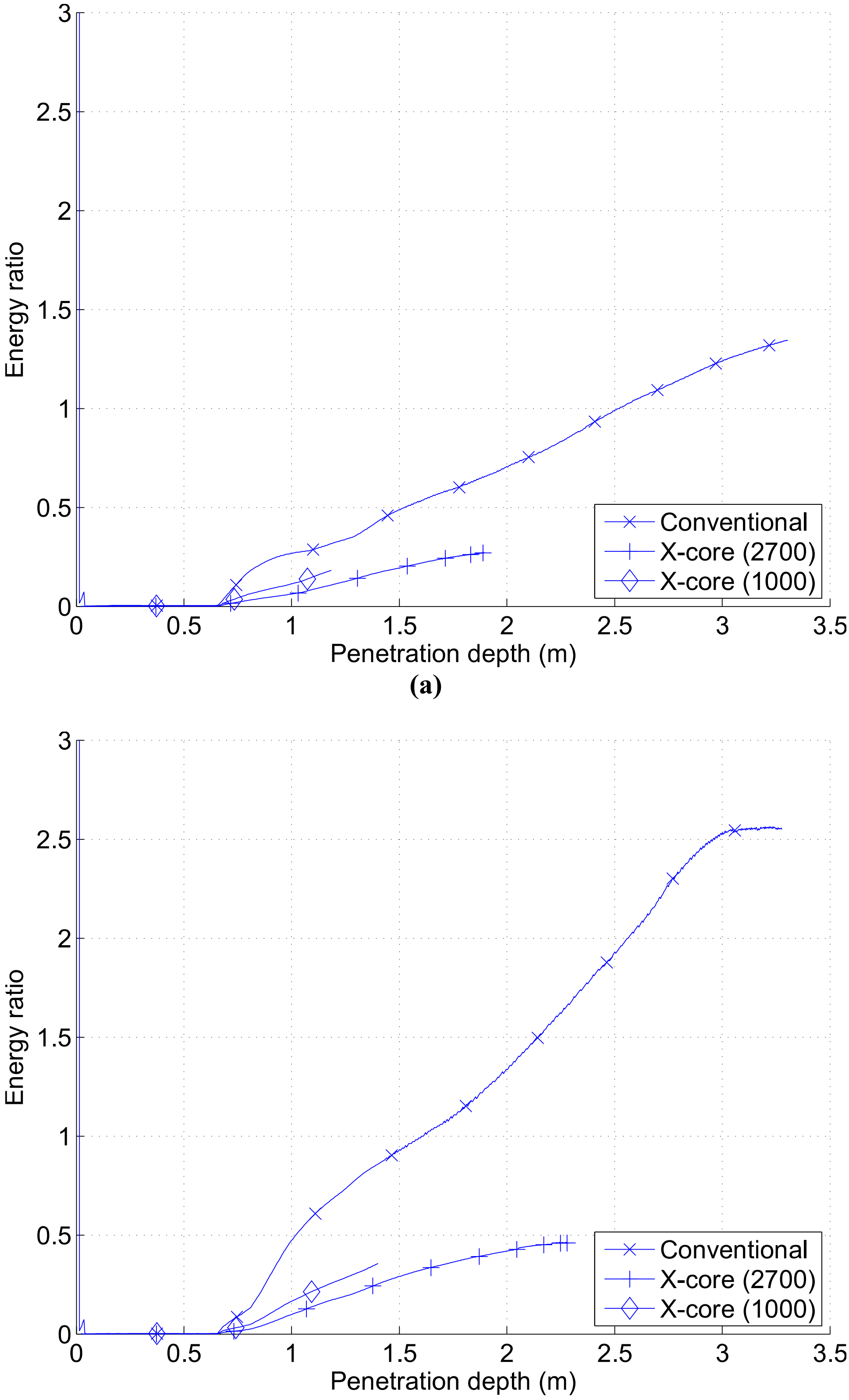

(a)

(b)

Fig. 48. Upper draught, RTCL-criterion: ratios between energies absorbed by stem and bulb for an impact on a web frame (a) and between two web frames (b).

Results from collisions incorporating friction

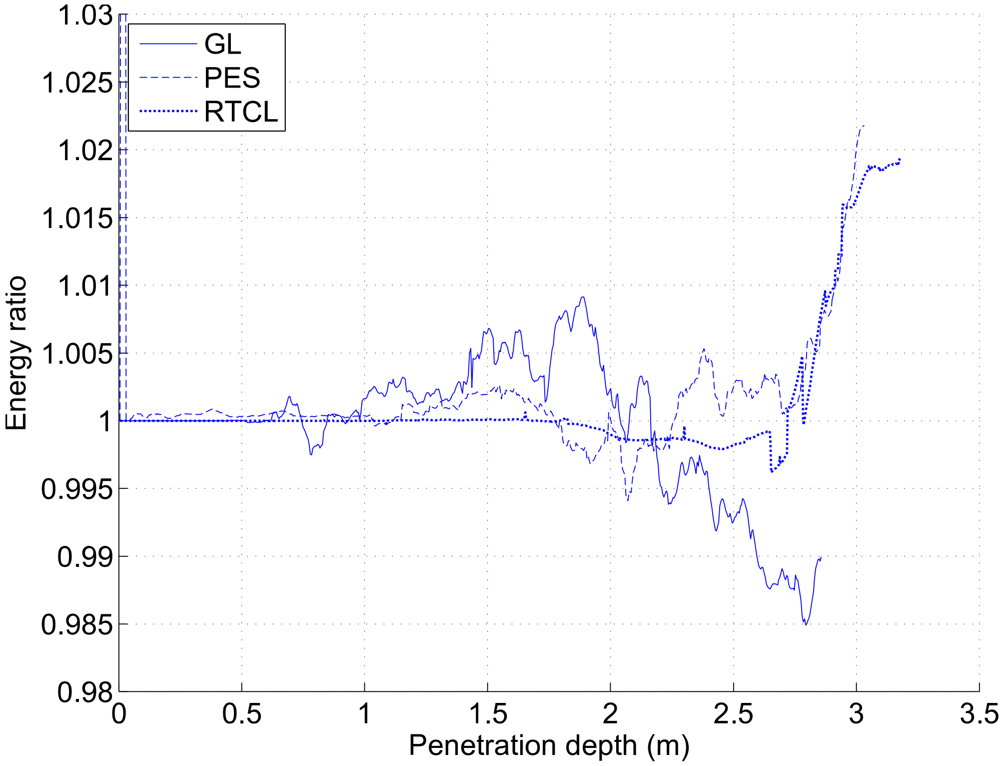

(a)

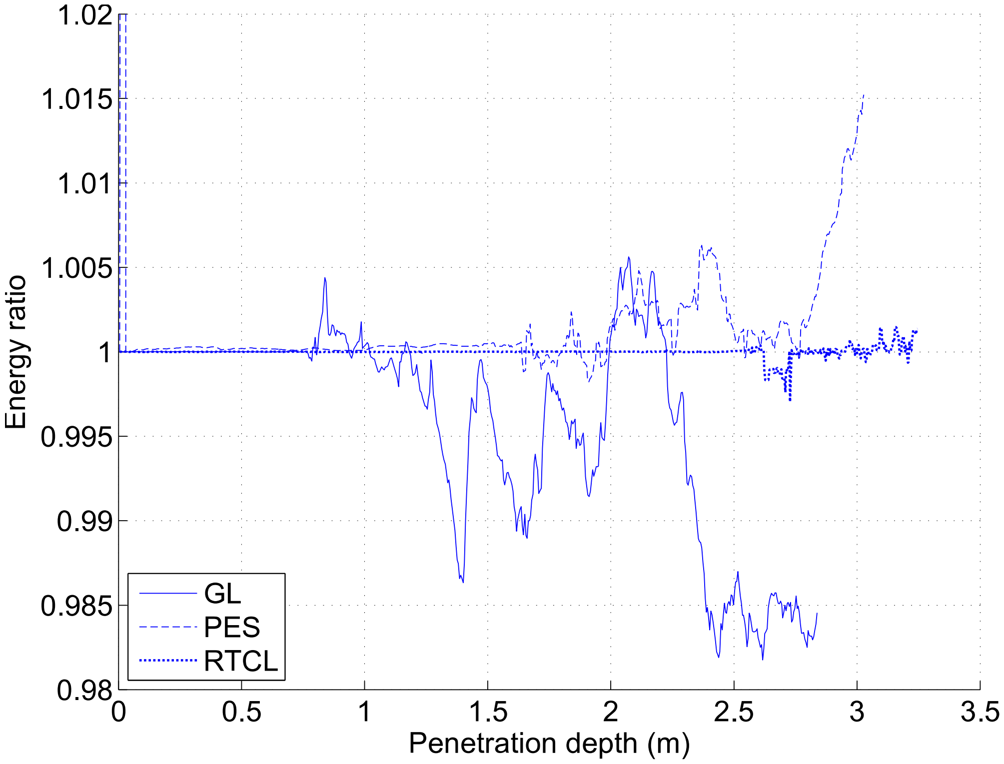

(b)

Fig. 49. Ratios between energies obtained from collisions with the conventional structure regarding and disregarding friction. Lower draught: impact on a web frame (a) and hit between two web frames (b).

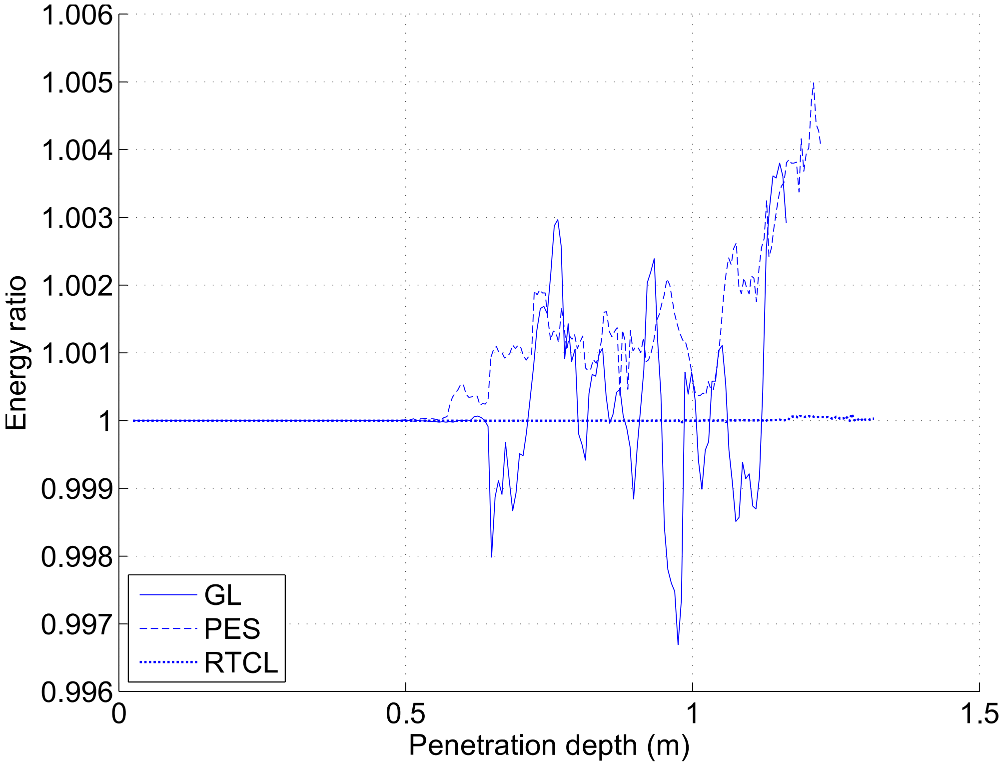

(a)

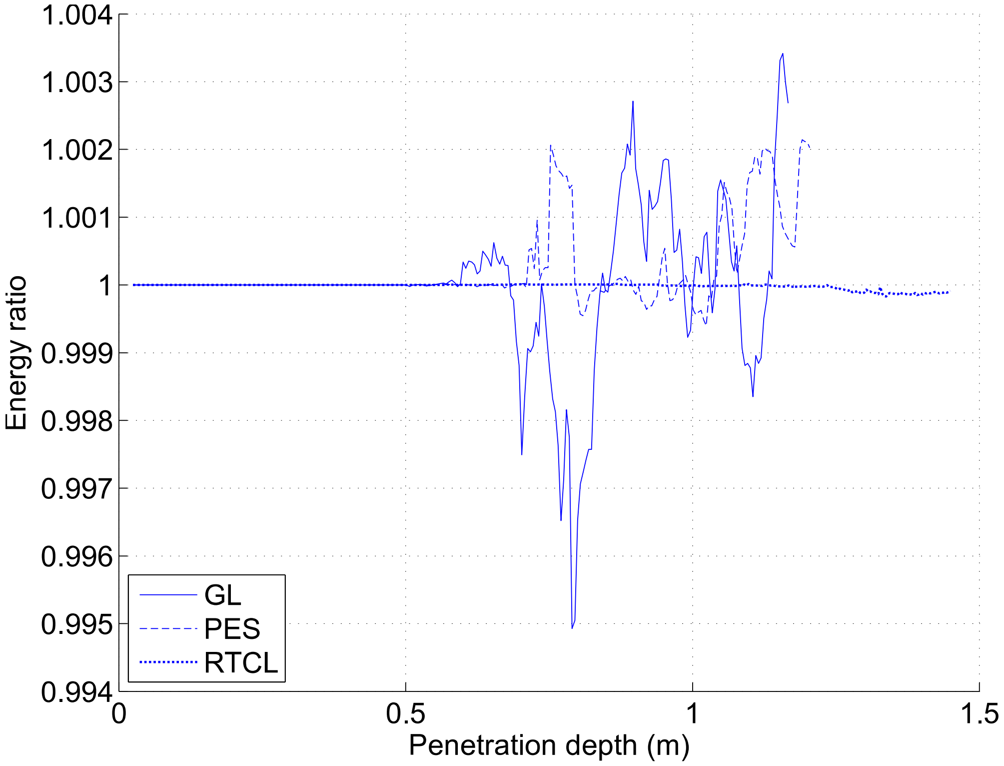

(b)

Fig. 50. Ratios between energies obtained from collisions with the narrow-spaced x-core structure regarding and disregarding friction. Lower draught: impact on a web frame (a) and hit between two web frames (b).

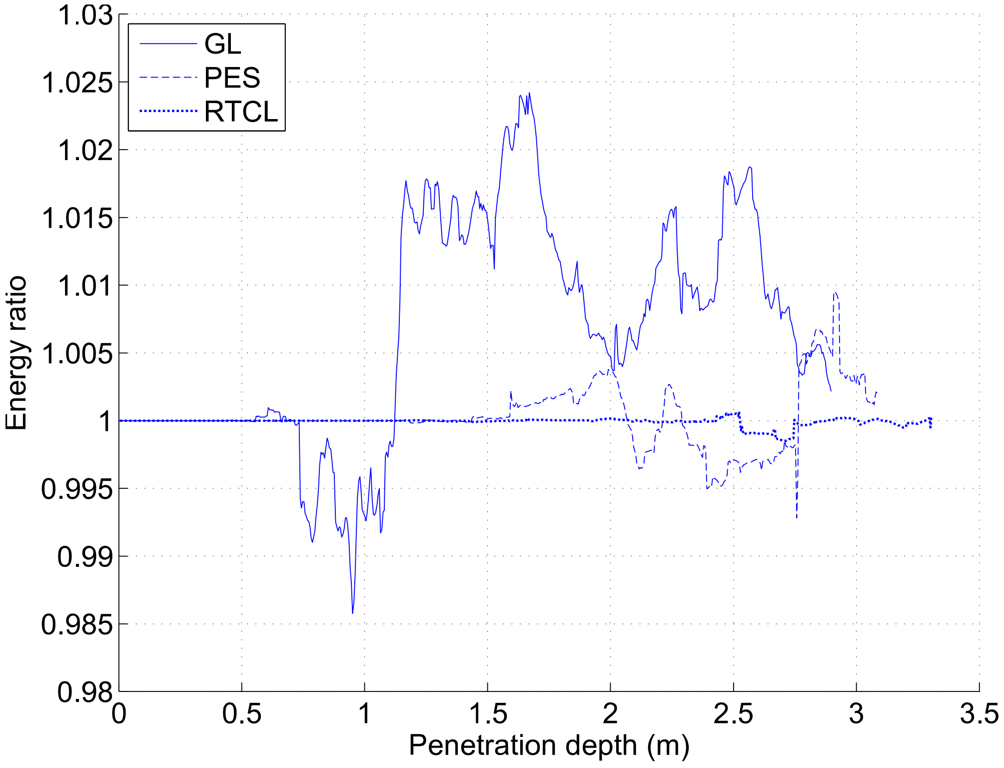

(a)

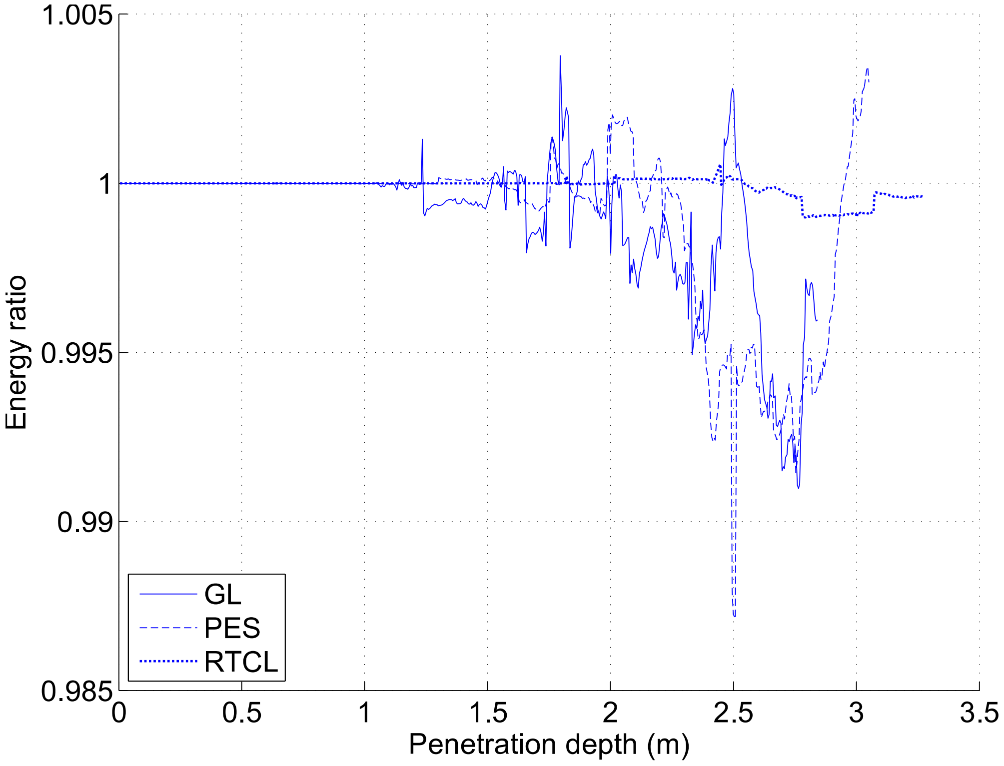

(b)

Fig. 51. Ratios between energies obtained from collisions with the conventional structure regarding and disregarding friction. Upper draught: impact on a web frame (a) and hit between two web frames (b).

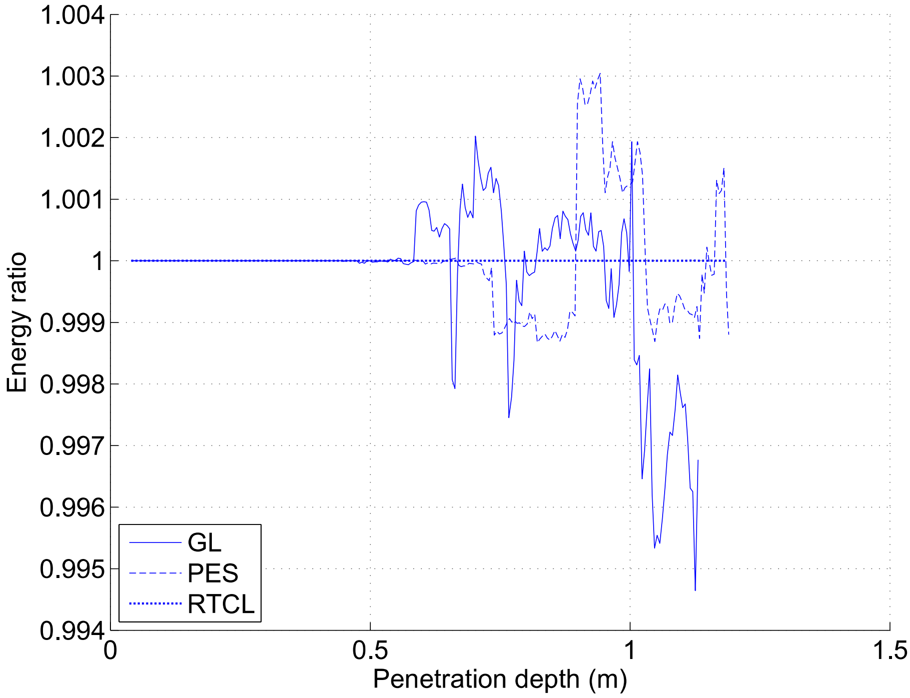

(a)

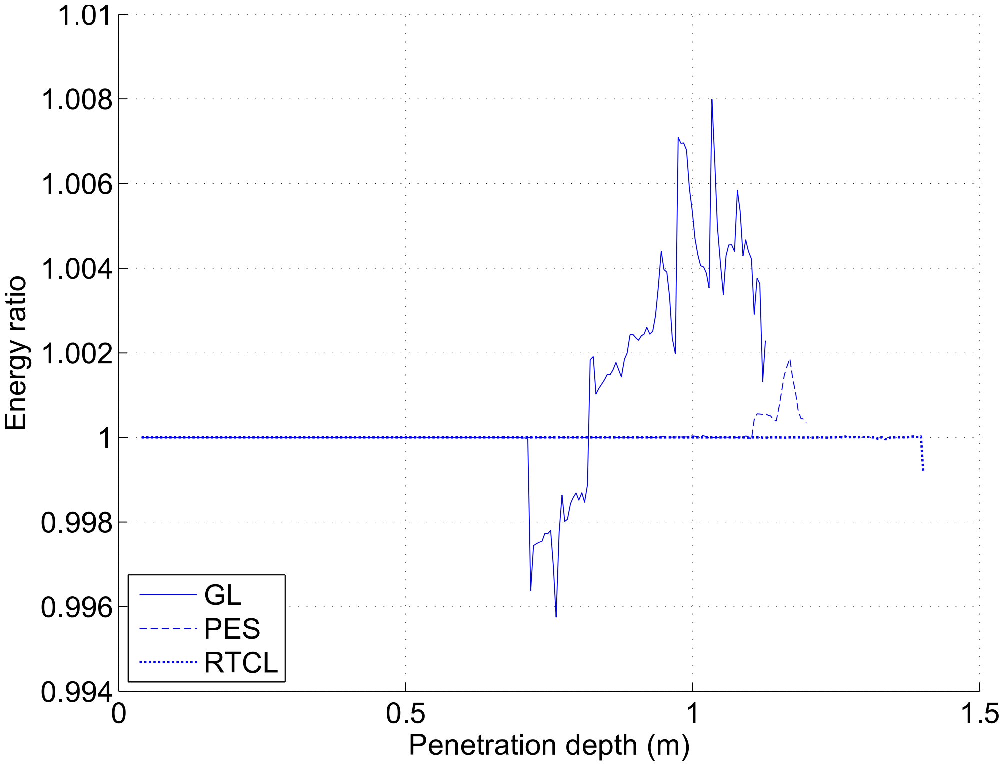

(b)

Fig. 52. Ratios between energies obtained from collisions with the narrow-spaced x-core structure regarding and disregarding friction. Upper draught: impact on a web frame (a) and hit between two web frames (b).

Results from collisions with defeatured structure

Table 6. Calculations times required for the detailed model in min (h:min), and resulting total absorbed energies in J.

Detailed	**Lower draught**		**Upper draught**	
	Impact on a web frame	Impact between two web frames	Impact on a web frame	Impact between two web frames
GL	1359 (22:39)	452 (7:32)	475 (7:55)	453 (7:33)
	22.42×10^{6}	25.20×10^{6}	13.92×10^{6}	11.85×10^{6}
PES	560 (9:20)	368 (6:08)	512 (8:32)	501 (8:21)
	60.27×10^{6}	54.29×10^{6}	36.30×10^{6}	33.73×10^{6}
RTCL	1702 (28:22)	2133 (35:33)	636 (10:36)	768 (12:48)
	123.39×10^{6}	108.74×10^{6}	94.95×10^{6}	78.11×10^{6}

Table 7. Calculations times required for the defeatured model in min (h:min), and resulting total absorbed energies in J.

Defeatured	**Lower draught**		**Upper draught**	
	Impact on a web frame	Impact between two web frames	Impact on a web frame	Impact between two web frames
GL	235 (3:55)	229 (3:49)	228 (3:48)	209 (3:29)
	18.34×10^{6}	17.98×10^{6}	10.19×10^{6}	9.50×10^{6}
PES	257 (4:17)	247 (4:07)	268 (4:28)	232 (3:52)
	51.61×10^{6}	46.39×10^{6}	34.22×10^{6}	29.64×10^{6}
RTCL	509 (8:23)	477 (7:57)	315 (5:15)	285 (4:45)
	109.10×10^{6}	96.00×10^{6}	82.80×10^{6}	69.10×10^{6}

Table 8. Calculations times required for the defeatured and revised model in min (h:min), and resulting total absorbed energies in J.

Revised	**Lower draught**		**Upper draught**	
	Impact on a web frame	Impact between two web frames	Impact on a web frame	Impact between two web frames
GL	38 (0:38)	47 (0:47)	35 (0:35)	35 (0:35)
	16.70×10^{6}	15.58×10^{6}	9.73×10^{6}	8.51×10^{6}
PES	70 (1:10)	70 (1:10)	66 (1:06)	66 (1:06)
	39.41×10^{6}	37.20×10^{6}	15.73×10^{6}	14.02×10^{6}
RTCL	90 (1:30)	98 (1:38)	77 (1:17)	80 (1:20)
	88.27×10^{6}	90.41×10^{6}	44.09×10^{6}	46.83×10^{6}

Results from collisions with coarsened mesh

Table 9. Calculations times required for l = 200 mm in min (h:min), and resulting total absorbed energies in J.

l = 200 mm	**Lower draught**		**Upper draught**	
	Hit on a web frame	Hit between two web frames	Hit on a web frame	Hit between two web frames
GL	60 (1:00)	63 (1:03)	60 (1:00)	60 (1:00)
	16.68×10^{6}	15.93×10^{6}	5.91×10^{6}	5.53×10^{6}
PES	70 (1:10)	70 (1:10)	66 (1:06)	66 (1:06)
	39.41×10^{6}	37.20×10^{6}	15.73×10^{6}	14.02×10^{6}
RTCL	90 (1:30)	98 (1:38)	77 (1:17)	80 (1:20)
	88.27×10^{6}	90.41×10^{6}	44.09×10^{6}	46.83×10^{6}

Table 10. Calculations times required for l = 300 mm in min (h:min), and resulting total absorbed energies in J.

l = 300 mm	**Lower draught**		**Upper draught**	
	Hit on a web frame	Hit between two web frames	Hit on a web frame	Hit between two web frames
GL	27 (0:27)	27 (0:27)	26 (0:26)	27 (1:00)
	18.54×10^{6}	17.97×10^{6}	6.86×10^{6}	7.14×10^{6}
PES	32 (0:32)	31 (0:31)	28 (0:28)	27 (1:06)
	45.29×10^{6}	40.93×10^{6}	17.07×10^{6}	15.09×10^{6}
RTCL	43 (0:43)	70 (1:10)	33 (0:33)	45 (0:45)
	91.06×10^{6}	126.32×10^{6}	60.96×10^{6}	89.45×10^{6}

Table 11. Calculations times required for l = 400 mm in min (h:min), and resulting total absorbed energies in J.

l = 400 mm	**Lower draught**		**Upper draught**	
	Hit on a web frame	Hit between two web frames	Hit on a web frame	Hit between two web frames
GL	18 (0:18)	17 (0:17)	16 (0:16)	16 (0:16)
	19.65×10^{6}	19.80×10^{6}	7.48×10^{6}	7.44×10^{6}
PES	20 (0:20)	22 (0:22)	18 (0:18)	18 (0:18)
	46.06×10^{6}	43.39×10^{6}	17.39×10^{6}	16.64×10^{6}
RTCL	24 (0:24)	60 (1:00)	15 (0:15)	21 (0:21)
	76.36×10^{6}	130.03×10^{6}	39.44×10^{6}	66.47×10^{6}